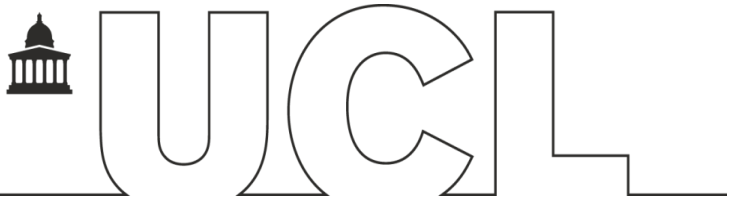

Transfer function analysis as a novel diagnostic tool for polymer electrolyte membrane fuel cells

Erik Charles Engebretsen

Submitted in part fulfilment of the requirements for the degree of Doctor of Philosophy at

University College London

2017

Declaration

I, Erik Charles Engebretsen, confirm that the work presented in this thesis is my own. Where information has been derived from other sources, I confirm that this has been indicated in the thesis.

…….

Signature

…….

Date

Abstract

Polymer electrolyte membrane fuel cells have shown great promise as a clean and renewable energy source due to their high efficiency and lack of carbon emissions at point of use. However, one of the great challenges in their wider commercialisation is the lack of *in-situ* metrological techniques to measure the performance of the devices over the course of their lifetime. In this work, novel transfer function analysis techniques are developed and applied to these devices to better understand their *in-situ* performance through perturbation and measurement of electrical, thermal, and pneumatic properties.

Localised electrochemical impedance spectroscopy measurements using a novel reference electrode array are made to measure spatially resolved, cathode-specific fuel cell performance for the first time, as well as membrane hydration transients when the fuel cell is polarised from open circuit.

Electro-thermal impedance spectroscopy, a transfer function technique relating an electrical perturbation to a thermal response, is developed to characterise the electrically-dependent thermal performance of an open-cathode fuel cell and identify faults such as pinhole formation and bowing of lands.

Electrochemical pressure impedance spectroscopy, a transfer function technique relating a cathodic pressure perturbation to an electrical response, is developed and applied to a fuel cell in order to characterise water management of a fuel cell under varying humidity conditions.

The impact of the techniques developed is discussed with scope for further advancement deliberated. The relevance of the application of the techniques is highlighted to give novel and complementary information not easily accessible by more conventional metrological methodologies.

Impact Statement

A by-product of the success of the industrial, technological, and digital revolutions has been the increasing need for power, heavily fuelled by fossil fuels. Our understanding of the impact of these activities on our environment is still relatively recent. The first UN Conference of the Parties (COP) to address climate change was held less than 30 years ago, with the aim of collaboratively understanding and addressing climate change. Twenty years on from the first COP, the Paris Agreement was signed by 195 member organisations committing to reducing greenhouse gas emissions.

The transition to a low carbon economy is dependent on the success of multiple alternative energy technologies to reduce our reliance on traditional fossil fuels. Hydrogen fuel cells have played niche roles in energy delivery over the past 70 years, however have emerged as a potential widespread energy conversion device to reduce carbon emission and increase energy security.

While commercialisation of hydrogen fuel cell products is being applied for a variety of applications, there are still limited diagnostic techniques to evaluate their *in-situ* performance. This thesis describes three diagnostic techniques which were developed and explored to aide in the understanding of fuel cell operation and identifying failure mechanisms.

Localised electrochemical impedance spectroscopy measurements were demonstrated to show there is a large variation in membrane hydration near the gas inlet compared to the

bulk of the fuel cell due to differences in humidity and temperature. Moreover, hydration transients on start-up were observed and showed that an excess of 5 mins was required for the membrane to achieve a new steady state. This can greatly influence the measurement and control of a fuel cell system on start-up.

Electrothermal Impedance Spectroscopy was used to relate the electrical behaviour of a fuel cell to its thermal properties. The technique was shown to identify areas of higher electro-thermal activity as well as manufacturing defects (uneven compression) and degradation faults (pinhole formation).

Electrochemical Pressure Impedance Spectroscopy was applied to relate the pressure of a fuel cell system with its electrical properties. The technique was shown to demonstrate a system's sensitivity at lower reactant stoichiometries and low humidity conditions.

The ultimate aim of the research is to provide stepping stones to develop a more comprehensive, standardised test for hydrogen fuel cell systems, similar to an MOT, in order to gain better insight into fuel cell performance over the lifetime of the product. This will aid in the reliability of fuel cell systems and prevent catastrophic failures of fuel cell systems in the field.

Table of Contents

List of Figures

List of Tables

List of Symbols and Abbreviations

Symbol	Definition	Unit
α	Charge transfer coefficient	(-)
ΔG	Gibbs free energy	J
ε	Thermal emissivity	(-)
ρ	Density	kg m^{-3}
λ	Wavelength	m
σ	Stefan - Boltzmann constant	W m K^{-4}
η	Polarisation	V
Γ	Charge required to reduce monolayer of protons on platinum	µC cm^{-2}
ϕ	Phase shift	°
ω	Frequency	Hz
A	Geometric surface area	m^2
a	Activity	(-)
B	Radiant flux	J s^{-1}
b	Wien's displacement constant	m K
C_p	Specific heat	kg m^2 K^{-1} s^{-1}
c	Speed of light	m s^{-1}
D	Experimentally determined mass transport constant	V
E	Potential	V
F	Faraday constant	C mol^{-1}

$\boldsymbol{h}$	Planck constant	m^2 kg s^{-1}
$\boldsymbol{i}$	Current density	mA cm^{-2}
$\boldsymbol{i_l}$	Limiting current density	mA cm^{-2}
$\boldsymbol{i_o}$	Exchange current density	mA cm^{-2}
$\boldsymbol{k}$	Thermal conductivity	W m^{-1} K^{-1}
$\boldsymbol{k_b}$	Boltzmann constant	m^2kg s^{-2} K^{-1}
$\boldsymbol{L}$	Platinum loading	mg cm^{-2}
$\boldsymbol{l}$	Length / thickness	m
$\boldsymbol{n}$	Number of electrons transferred	(-)
$\boldsymbol{P}$	Pressure	Pa
$\boldsymbol{p}$	Partial pressure	Pa
$\boldsymbol{Q}$	Heat input	W
$\boldsymbol{q_{Pt,ads/des}}$	Integral of desorption and adsorption peaks	C cm^{-2}
$\boldsymbol{R}$	Resistance	Ω
$\boldsymbol{\bar{R}}$	Universal gas constant	kg m^2 s^{-2} K^{-1} mol^{-1}
$\boldsymbol{r}$	Area-specific resistance	Ω cm^{-2}
$\boldsymbol{T}$	Temperature	°C, K
$\boldsymbol{t}$	Time	s
$\boldsymbol{V}$	Voltage	V
$\boldsymbol{v_j}$	Stoichiometric coefficient	(-)
$\boldsymbol{Z}$	Impedance	Ω cm^2

Subscript	Definition
a	Anode
act, a	Activation, anode
act, c	Activation, cathode
c	Cathode
$conc, a$	Concentration, anode
$conc, c$	Concentration, cathode
CT	Charge transfer
DL	Double layer
ohm	Ohmic
rxn	Reaction
ss	Steady state
t	Time domain

List of symbols used in data fitting:

Symbol	Definition
A_x	Amplitude
B_x	Horizontal Shift
C_x	Vertical Shift

Subscript	Definition
P	Pressure
T	Temperature
V	Voltage
i	Current density

List of abbreviations used:

Abbreviation	Definition
AC	Alternating current
AR	Amplitude ratio
AST	Accelerated Stress Test
BPP	Bipolar plate
BV	Butler-Volmer
CV	Cyclic voltammetry
DC	Direct current
ECSA	Electrochemically active surface area
EIS	Electrochemical impedance spectroscopy
EPIS	Electrochemical pressure impedance spectroscopy
ETIS	Electro-thermal impedance spectroscopy
GDE	Gas diffusion electrode
GDL	Gas diffusion layer
HF	High frequency
HOR	Hydrogen oxidation reaction
IR	Infrared
LF	Low frequency
MEA	Membrane electrode assembly
MPL	Micro-porous layer
OCV	Open circuit voltage

ORR	Oxygen reduction reaction
PEM	Polymer electrolyte membrane
PEMFC	Polymer electrolyte membrane fuel cell
PS	Phase shift
SEM	Scanning electron microscopy
SHE	Standard hydrogen electrode

List of Equations

Acknowledgements

Firstly, I'd like to thank by supervisors Dan, Paul, and Gareth – I couldn't have asked for a more supportive, challenging, and motivated trio to guide me through this journey. Your relentless work ethic and ability is an aspiration for any researcher. The financial support from the NPL and EPSRC has been invaluable.

To the senior researchers in the group, particularly Tom, Jay, and Toby – thank you for always giving time and a cup of tea to bounce off ideas off you and get from concept to reality. I have learned more than you can imagine from shadowing you in the office & lab.

To my mother and father, I hope this is further evidence that your multi-year investment is paying off. To the both of you, Anita, Jon, and Leo: Thank you for your years of love and support and daring me to strive for more.

To Vidal, what started with a less than savoury post-it note has resulted in an entrepreneurial partnership; let's see how high this kite can fly. Thanks to you, Rhod, and James for populating the evenings with meaningless chat to clear the mind and understanding the Good Friday Agreement.

To the researchers at the EIL, thank you for making the office and lab a perpetually entertaining place to work. I've come across enough characters to occupy a Tolkien novel.

Finally, to Jackie, I'm blessed to have had years of your support. I promise my next qualification will be more practical: a driver's licence.

Publications & Presentations

Publications

- E. Engebretsen, J.B. Robinson, O. Obeisun, T. Mason, D. Finegan, G. Hinds, P.R. Shearing, D.J.L. Brett, Electro-thermal impedance spectroscopy applied to an open-cathode polymer electrolyte membrane fuel cell, Journal of Power Sources, 302 (2016) 210-214.
- E. Engebretsen, T.J. Mason, P.R. Shearing, G. Hinds, D.J.L. Brett, Electrochemical pressure impedance spectroscopy applied to the study of polymer electrolyte membrane fuel cells, Electrochemistry Communications, 75 (2017) 60-63.
- E. Engebretsen, G. Hinds, Q. Meyer, T. Mason, E. Brightman, , L. Castanheira, P.R. Shearing, D.J.L. Brett, Localised electrochemical impedance measurements of a polymer electrolyte fuel cell using a reference electrode array to give cathode-specific measurements and examine membrane hydration dynamics, Manuscript submitted for publication.
- J.B. Robinson, E. Engebretsen, D. Finegan, J.A. Darr, G. Hinds, P.R. Shearing, D.J.L. Brett, Detection of internal defects in lithium ion batteries using lock-in thermography, ECS Electrochemistry Letters, 4 (2015) A106-A109.
- O.A. Obeisun, Q. Meyer, E. Engebretsen, D.P. Finegan, J.B. Robinson, G. Hinds, P.R. Shearing, D.J.L. Brett, Study of water accumulation dynamics in the channels of an open-cathode fuel cell through electro-thermal characterisation and droplet visualisation, International Journal of Hydrogen Energy, 40 (2015) 16786-16796.

- Q. Meyer, S. Ashton, P. Boillat, M. Cochet, E. Engebretsen, D.P. Finegan, X. Lu, J.J. Bailey, N. Mansor, R. Abdulaziz, O.O. Taiwo, R. Jervis, S. Torija, P. Benson, S. Foster, P. Adcock, P.R. Shearing, D.J.L. Brett, Effect of gas diffusion layer properties on water distribution across air-cooled, open-cathode polymer electrolyte membrane fuel cells: A combined ex-situ X-ray tomography and in-operando neutron imaging study, Electrochimica Acta, 211 (2016) 478-487.
- Q. Meyer, S. Ashton, S. Torija, C. Gurney, P. Boillat, M. Cochet, E. Engebretsen, D.P. Finegan, P. Adcock, P.R. Shearing, D.J.L. Brett, Nitrogen Blanketing and Hydrogen Starvation in Dead-Ended-Anode Polymer electrolyte membrane Fuel Cells Revealed by Hydro-Electro-Thermal Analysis, Electrochimica Acta, 203 (2016) 198-205.
- O.A. Obeisun, D.P. Finegan, E. Engebretsen, J.B. Robinson, O.O. Taiwo, G. Hinds, P.R. Shearing, D.J.L. Brett, Ex-situ characterisation of water droplet dynamics on the surface of a fuel cell gas diffusion layer through wettability analysis and thermal characterisation, International Journal of Hydrogen Energy, 42 (2017) 4404-4414.
- Bharath, V. J., J. R. Jervis, et al. (2017). "Effect of humidity on the interaction of CO_2 with alkaline anion exchange membranes probed using the quartz crystal microbalance." International Journal of Hydrogen Energy 42(38): 24301-24307.

Presentations at Conferences

- Zing 3rd Hydrogen & Fuel Cells Conference, Mexico, 2015. Electro-thermal impedance spectroscopy applied to an open-cathode polymer electrolyte fuel cell.
- ECS Conference on Electrochemical Energy Conversion & Storage with SOFC-XIV, UK, 2015. Localised Electrochemical Impedance Measurement using an Innovative Reference Electrode Array.
- H2FC Supergen, UK, 2014. Pneumato-Electrical Impedance Spectroscopy as a Novel Diagnostic Tool for Polymer Electrolyte Fuel Cells.
- H2FC Supergen, UK, 2013. Transfer Function Analysis as a Novel Diagnostic Technique in Polymer Electrolyte Fuel Cells.
- Electrochem 2013. Transfer Function Analysis as a Novel Diagnostic Technique in Polymer Electrolyte Fuel Cells.

Chapter 1

Introduction

1.1 Motivation

Fuel cells are a key technology in power production for the transition from a carbon-based economy to a sustainable, low carbon future. Polymer electrolyte membrane fuel cells (PEMFCs) have a relatively high power density, low-temperature operation, and produce no carbon emissions at point of usage [1, 2].

However, there are limitations to the technology as PEMFCs have high material costs [3], are sensitive to certain fuel and oxidant impurities [4, 5] in addition to knowledge gaps related to the internal mechanisms of operation [6]. *In-situ* diagnostic performance tests are essential tools used to gain insight into the inner workings of an operational PEMFC. This insight may lead to durability improvements and optimisation of performance, critical issues in the further commercialisation of the technology [7], as well as more comprehensive models of fuel cell operation.

Electrochemical impedance spectroscopy (EIS) is a powerful diagnostic tool which can be used to identify various performance losses in fuel cells [8]. A small sinusoidal perturbation in operating voltage is imposed on the fuel cell and the resultant current

response is measured, or vice - versa. The phase shift and amplitude ratio between the voltage and current are dependent on the frequency of the imposed wave due to the varying time constants at which electrochemical phenomena occur. These parameters, over a range of perturbation frequencies, can identify various electrical resistances and capacitances in the system. EIS has often been applied to PEMFCs to distinguish between effects caused by purely Ohmic losses and those caused by electro-kinetic and mass-transport limiting processes.

However, EIS is only able to directly identify electrochemical properties of the fuel cell system. By applying the same cause - effect relationship to other physical perturbations and system responses, novel transfer functions can unlock thermal, chemical, and mechanical properties of the fuel cell. Moreover, they can be used to provide performance data complementary to EIS. This can be achieved in part through selection of appropriate frequency ranges where it is expected selected physical properties will be perturbed by a periodic stimulus.

1.2 Research aims and objectives

The aim of this research is to outline conventional transfer function based *in-situ* diagnostic methods for PEM fuel cells and the relevant understanding of PEMFC behaviour gained by application of these techniques. Novel transfer function techniques are then described, developed and applied to PEMFCs to provide complementary information to the current understanding of fuel cell behaviour and failure mechanisms.

The development of novel transfer functions as a diagnostic tool for PEM fuel cells requires the identification of suitable cause - effect relationships that may give complementary results to common understanding of fuel cell behaviour, as well as novel insight into fuel cell performance. The accessibility of testing equipment to perform system perturbations and measurements was also considered when selecting transfer functions to develop.

The key objectives of this research were:

- To investigate the understanding of cathode-specific behaviour and spatially-resolved membrane hydration dynamics using conventional EIS combined with a novel reference electrode array.
- To develop Electro-thermal Impedance Spectroscopy (ETIS), a transfer-function between an electrical perturbation and thermal response, on an open - cathode fuel cell. The open-cathode allowed for unimpeded thermal imaging of the fuel cell gas diffusion layer and served as a good model system on which to develop ETIS and study common fault mechanisms of PEMFCs.
- To develop Electrochemical Pressure Impedance Spectroscopy (EPIS), a transfer-function between a pressure perturbation and electrical response, in a closed PEMFC system. The fuel cell EPIS behaviour was characterised as a function of current density and system humidification to better understand water management.

1.3 Thesis outline

In Chapter 2, factors affecting fuel cell performance and the current state of diagnostic technology are discussed. Relevant literature to each diagnostic study is included in the introduction of each respective results chapter. In Chapter 3, the materials and methodology of developing the three novel transfer-function techniques are discussed. In Chapter 4, the conventional EIS technique is combined with the use of a novel reference electrode array to perform localised cathode-specific measurements. The transient high-frequency resistance is then used to probe membrane hydration dynamics. In Chapter 5, a new diagnostic technique, ETIS, is developed and applied to an open-cathode fuel cell at varying current densities to yield information about water management in fuel cells. It is also applied to identify electro-thermally dependent fuel cell failure mechanisms. In Chapter 6, EPIS is developed and applied to a single cell PEMFC system. The results discussed yield information on water management complementary to current PEMFC understanding. Finally, in Chapter 7, the results are summarised and possible approaches to further developing and tuning the techniques are discussed.

Chapter 2

Literature Review

The aims of the literature review are to explain the operation of polymer electrolyte membrane fuel cells (PEMFCs), describe existing diagnostic techniques used to analyse fuel cells, and how those diagnostic techniques have contributed to current understanding of fuel cell operation. The fundamental mathematics of transfer function analysis are described and applied to conventional electrochemical impedance spectroscopy (EIS). Literature specific to the application of localised EIS, Electro-thermal Impedance Spectroscopy (ETIS), and Electrochemical Pressure Impedance Spectroscopy (EPIS), are discussed in the introduction of each respective results chapter.

2.1 Fuel Cell Technology Overview

A fuel cell is a device which converts chemical energy directly to electrical energy and hence is not limited by the Carnot Cycle [1, 9]. Unlike batteries, fuel cells have a continuous flow of fuel supplied from an external source as opposed to having the 'fuels' (redox chemicals) encased within their structure (as in a conventional Li-ion battery, for example).

Fuel cells generate electricity through a series of electrochemical reactions. At one electrode (the anode), oxidation occurs, causing the transfer of electrons and at the other electrode (the cathode), reduction occurs.

While the reactions can vary depending on fuel cell type, the principle is the same; a fuel is electrochemically converted to produce a flow of electrons. A comparison of common fuel cell types is shown in Table 2.1.

Fuel Cell Type	Advantages	Disadvantages
Alkaline FC	High efficiency, low oxygen reduction reaction losses, inexpensive catalyst	Must run on pure oxygen to avoid CO_2 contamination, corrosion
Phosphoric Acid FC	1-2 % CO tolerant, good quality waste heat, durable	Low power density, expensive, slow start-up, loss of electrolyte
Solid Oxide FC	CO tolerant, fuel flexible, high-quality waste heat, inexpensive catalyst	Long start-up time, durability under thermal cycling, inactivity of electrolyte below 600 °C
Molten Carbonate FC	CO tolerant, fuel flexible, high-quality waste heat, inexpensive catalyst	Electrolyte dissolves cathode catalyst, long start up time, CO_2 must be injected into cathode, electrolyte maintenance
Polymer electrolyte membrane FC	Low-temperature operation, high efficiency, high hydrogen power density, relatively rapid start up	Expensive catalyst, durability, poor quality waste heat, intolerant to CO, thermal and water management

Table 2.1 - Advantages and disadvantages of different fuel cell types (adapted from Mench [1])

Despite the need for expensive platinum catalyst and relatively high degradation rate, the advantages of PEMFCs listed in Table 2.1 have made them the leading fuel cell technology both in terms of units and megawatts sold [10].

A PEMFC uses hydrogen as its fuel and the overall cell reaction is:

$$H_2 + \frac{1}{2}O_2 \leftrightarrow H_2O$$

Equation 2.1 – Reaction between hydrogen and oxygen

The only by-product of the reaction is pure water, although side reactions can occur due to the presence of impurities in feed streams and other chemical species in the materials that make up the fuel cell.

The overall reaction in Equation 2.1 is comprised of two half reactions. At the anode, electrons and protons are separated through the oxidation of hydrogen.

$$H_2 \leftrightarrow 2H^+ + 2e^-$$

Equation 2.2 – Hydrogen oxidation reaction (HOR)

The electrons flow through an external circuit while the protons migrate through the membrane to recombine with the electrons and reduce oxygen.

$$\frac{1}{2}O_2 + 2H^+ + 2e^- \leftrightarrow H_2O$$

Equation 2.3 – Oxygen reduction reaction (ORR)

The reactions described in the aforementioned equations describe basic fuel cell operation, depicted in Figure 2.1.

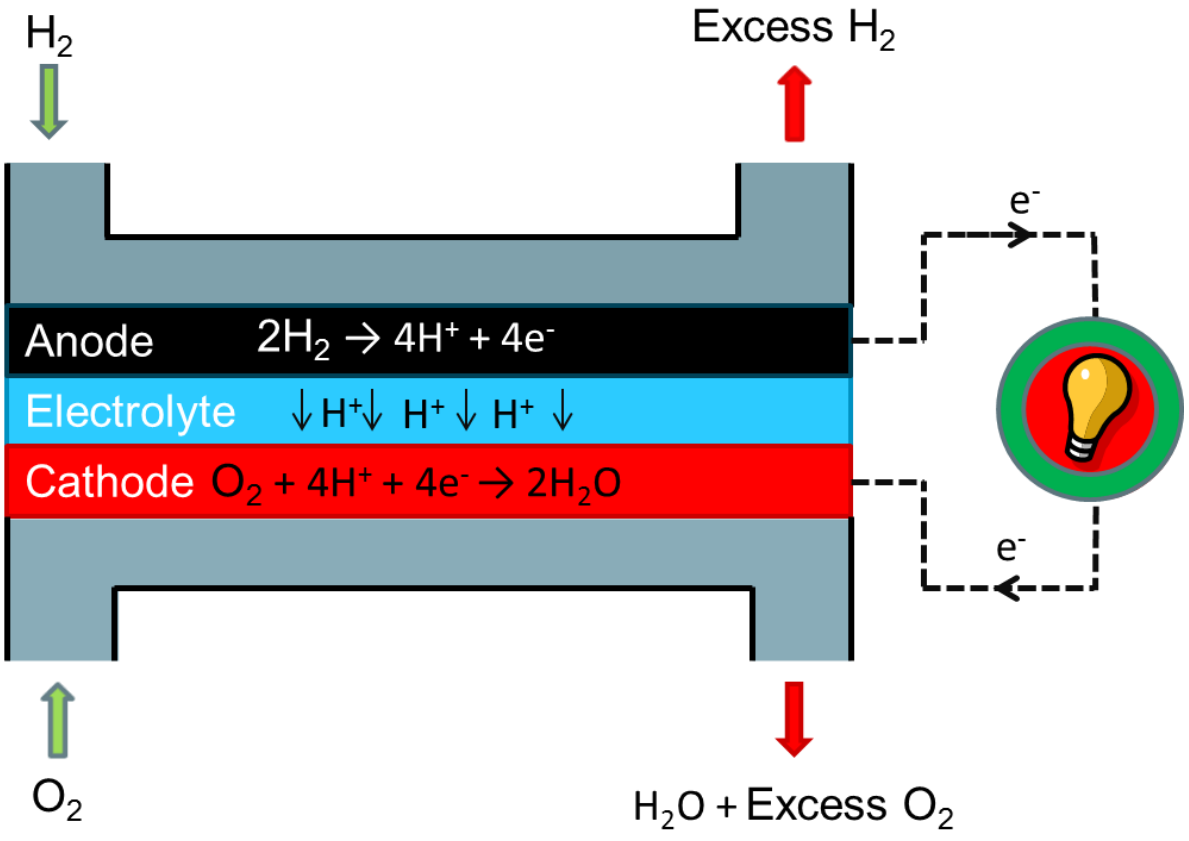

Figure 2.1 - Diagram of hydrogen fuel cell operation and redox reactions at both electrodes.

The kinetics of the oxygen reduction reaction (ORR) are much slower than the hydrogen oxidation reaction (HOR), hence the amount of catalyst on the cathode is generally much higher than that of the anode; typically 0.4 mg cm^{-2} and on the cathode and 0.1 mg cm^{-2} on the anode. Both electrodes are made of a catalyst layer (CL), usually made of platinum distributed on carbon supports which reduces the activation energy of the HOR and ORR. Despite advancements in optimising the loading of platinum on carbon, the catalyst contributes to a high proportion of PEMFC costs due to its high spot price regularly exceeding 22 GBP g^{-1} [11]. This has resulted in extensive research in platinum alloy and non-platinum based catalysis for PEMFCs [12].

As the PEMFC name suggests, a polymer electrolyte membrane is present between the electrodes to promote the transfer of ions that are produced and consumed as a result of the redox reactions. The solid polymer membrane electrolyte transfers protons from the anode to the cathode. Humid gas and the production of water hydrate the membrane, ensuring good proton conductivity. The most commonly used membrane material is Nafion™, a sulfonated tetrafluoroethylene developed and produced by DuPont. The widespread use of Nafion can be attributed to its properties as a good proton conductor with strong mechanical properties; however, this comes with cost implications [13]. The cost of Nafion at low volumes can be around 1660 GBP m^{-2} from distributors such as Ion Power.

Beyond the catalyst layers, there are gas diffusion layers (GDL) which serve several purposes; they allow for the even distribution of gases on to the catalyst surfaces, have a crucial role in management of liquid water build up, are the mechanical interface between

catalyst and bipolar plates, and carry current to and from the catalyst layer to the bipolar plates. These are often made of a hydrophobic carbon cloth. There is often a sub-layer of the GDL present on the catalyst layer called the micro-porous layer (MPL) carbon cloth mesh that facilitates effective water management in the electrodes and electrolyte and increases the supply of oxidant and fuel to the electrodes.

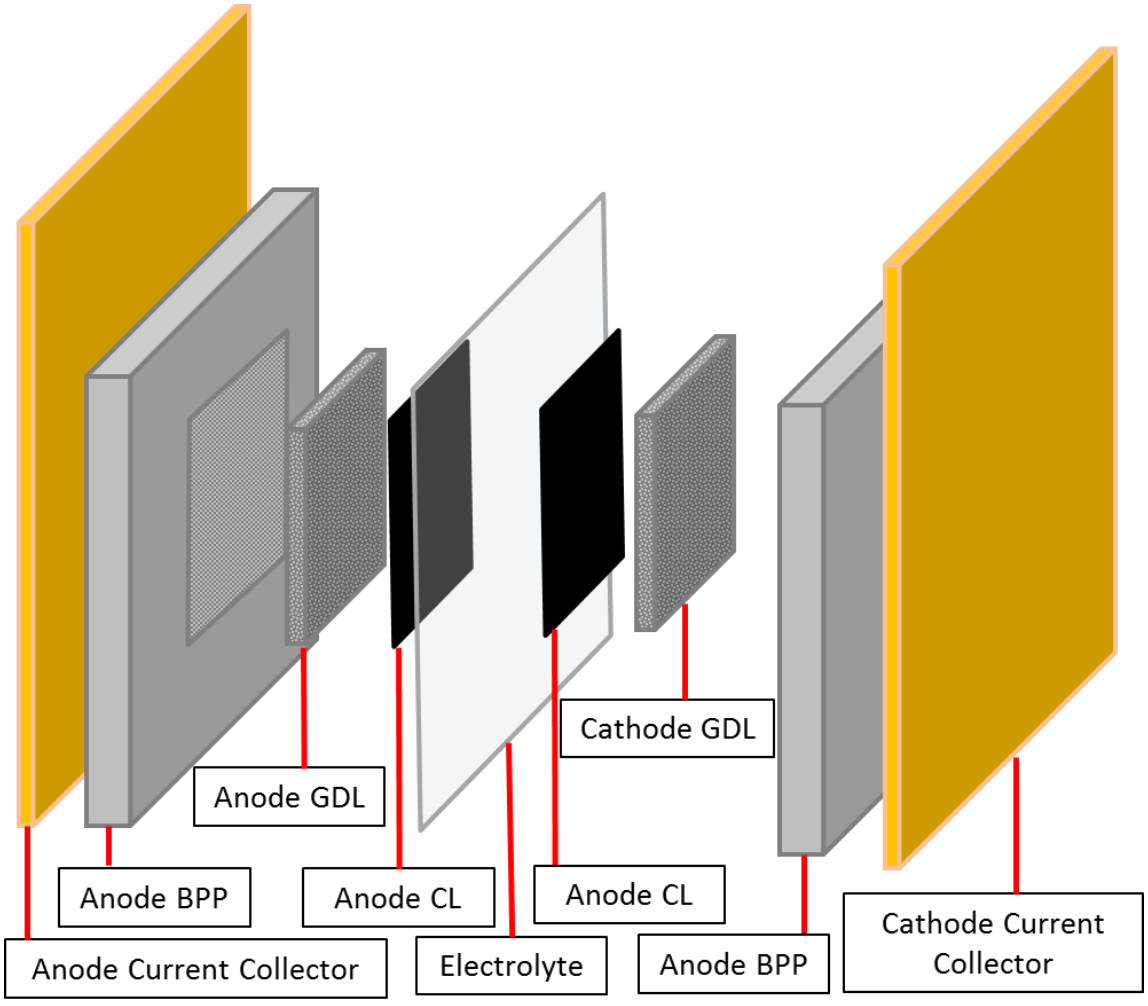

Figure 2.2 – Diagram of expanded components of a hydrogen fuel cell. Thicknesses are not shown to scale.

The intersection of the electrolyte and catalyst is a crucial interface which affects fuel cell performance as it provides locations where catalyst and gas reactant are present, while also providing both ionic pathways for the protons to migrate through the electrolyte and electron pathways for the current to flow through the external circuit. This interface is known as the triple-phase boundary.

The bonded electrode-membrane-electrode is commonly known as the membrane electrode assembly (MEA). The MEA is placed between two bipolar plates (BPPs) which serve to distribute the reactant gases through channels and provide electrical conduction to and from the electrodes. These are often made of graphite or coated stainless steel, among other materials, which are electrically conductive and corrosion-resistant in order to remain durable in the fuel cell environment [14].

2.2 Fuel Cell Performance

PEMFC performance is often characterised by a polarisation curve. This demonstrates the relationship between the voltage and current density of a PEMFC and highlights typical factors that contribute to performance losses at different current densities. Fuel cells are subject to a number of losses, or polarisations, during operation. The extent of these losses are dependent on the current drawn from the fuel cell, as shown by the current-voltage (*i* - *V*) curve, shown in Figure 2.3.

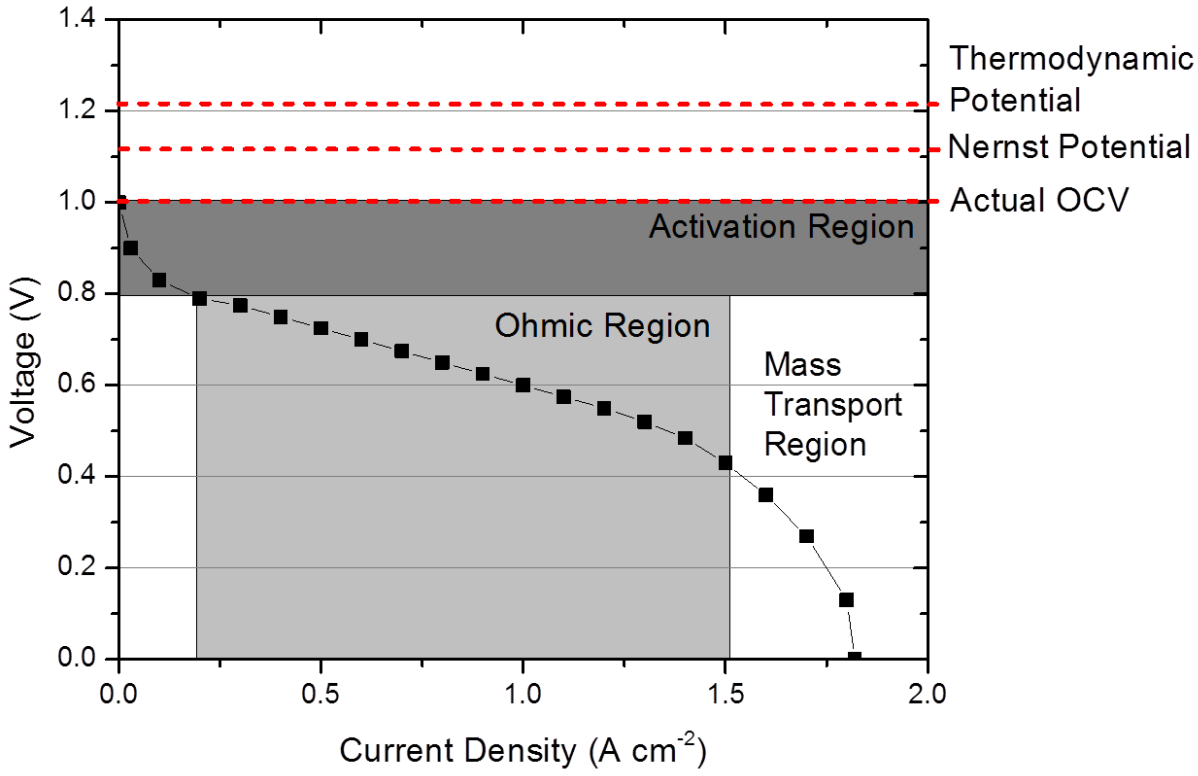

Figure 2.3 - Typical *i-V* curve for a PEM fuel cell showing approximate regions where activation, Ohmic, and mass transport polarisations dominate. The difference between the Nernst potential and OCV is attributed to the loss due to the crossover of reactant gas and the reaction between platinum and oxygen. All polarisations are arguably present as long as current is drawn from the system, but vary in contribution depending on current density [1].

In Figure 2.3, the activation region is specified at low current densities due to the fact that it is required to overcome the overpotential to draw current from the fuel cell. The mass transport is designated at higher current densities where water formation blocks reaction sites and reactants become unable to reach the catalyst layer. The Ohmic region is a

proportional function of current density, thus it is highlighted as the dominant polarisation between the previous two polarisations.

In general, the polarisation curve can be represented by:

$$E(i) = E^o - \eta_{\text{act,a}} - \eta_{\text{act,c}} - \eta_{\text{ohm}} - \eta_{\text{conc, a}} - \eta_{\text{conc, c}}$$

Equation 2.4 – Fuel cell voltage as a function of polarisation losses

Where *E(i)* is the operating voltage of the fuel cell, E^o is the open circuit voltage, and each η represents the various polarisations present in a fuel cell system.

Ultimately, the region in which the fuel cell operates will be a trade-off between the power delivered and the efficiency of the system. The proceeding sections will discuss the factors which affect each polarisation as well as provide general equations which represent each polarisation in Equation 2.4.

2.2.1 Open Circuit Voltage (OCV)

The maximum theoretical voltage between the electrodes of the redox reaction shown in Equation 2.2 and Equation 2.3 is 1.23 V [1, 15] which can be calculated using thermodynamic considerations. The reversible cell voltage, or open circuit voltage (OCV), is a function of both pressure and temperature and is represented by the Nernst Equation.

The Nernst equation accounts for operating conditions such as fuel and oxidant activity and operating temperature [1] to calculate the OCV:

$$E^o = -\frac{\Delta G^0_{\text{rxn}}}{nF} + \frac{\bar{R}T}{nF} \ln \frac{\prod a^{v_j}_{\text{products}}}{\prod a^{v_j}_{\text{reactants}}}$$

Equation 2.5 – Nernst Equation

The first term in the Nernst Equation accounts for the theoretical fuel cell voltage under standard conditions and the second term for the thermodynamic activity dependence. The Nernst equation is a result of the equilibrium achieved at the electrode surfaces. In reality, there is a decreasing concentration gradient of reactants from the bulk solution to the electrode surface, particularly under load. In addition, any species that are not part of the HOR or ORR redox reactions are not represented in the equation but will contribute to the OCV if it they electro active.

With the above considered, the Nernst Potential of a PEMFC would exceeds 1 V, however, the real OCV is generally between 0.9 and 1 V due to reactant crossover through the electrolyte, internal currents through electron leakage through the electrolyte, and other contamination such as the formation of PtO where the platinum catalyst has interacted with oxygen on the cathode [16].

2.2.2 Activation Polarisation

The activation polarisation is a voltage loss associated with the need to overcome the activation energy of the electrochemical reaction on the catalyst surface. In Equation 2.4 the activation losses at the anode and cathode are represented by $\eta_{act,a}$ and $\eta_{act,c}$, respectively.

To understand the activation losses, the activity at the catalyst interface needs to be examined. The electrical double-layer arises as a result of a build-up of charge on the electrode. At the anode, a negative charge builds due to the adsorption of hydrogen on the catalyst surface and also results in an accumulation of positive charge on the adjacent cathode. This charge accumulation is what is referred to as the capacitance of the double layer. The origin of the activation polarisation is the voltage difference required to drive a current across the electrode-electrolyte interface.

The reaction mechanism, catalyst type, catalyst layer morphology, operating parameters, impurities, concentration of reactants, age, and service history of the fuel cell all affect the activation polarisation [1].

The activation polarisation is normally modelled using the Butler-Volmer equation shown below,

$$i = i_0 \left[\exp\left(\frac{\alpha n F \eta_{act}}{\bar{R}T}\right) - \exp\left(\frac{-(1-\alpha) n F \eta_{act}}{\bar{R}T}\right) \right]$$

Equation 2.6 – Butler-Volmer Equation

Where the first term (within the square brackets) represents the oxidation reaction and the second term represents the reduction reaction at the same electrode. The exchange current density i_o, is the current at net zero overpotential; the current at both electrodes which balance without drawing a net current. It is a function of concentration, temperature, catalyst, age, and other parameters. The anodic charge transfer coefficient, α, is the fraction of the activation polarisation energy that goes to enhancing the oxidation branch of the reaction at the anode.

The major assumption using Butler-Volmer (BV) kinetics is that the reaction is limited by a single electron transfer step. This may not be the case where parallel reactions or intermediate step reactions are present.

The structure of Equation 2.6 is such that there is both a forward and reverse reaction rate, in the special case that these reaction rates are similar (given by α = 0.5) a hyperbolic function is used to yield the following result,

$$i = 2i_0 \sinh\left(\frac{nF\eta_{act}}{2\bar{R}T}\right)$$

Equation 2.7 – Butler-Volmer Equation for case when α = 0.5

Alternatively, if the exchange current density is low or the polarization is significant, the Tafel Equation, Equation 2.8, can be used to describe the activation losses.

$$\eta_{act} = \frac{\bar{\bar{R}}T}{\alpha_{rct}} ln\left(\frac{i}{i_o}\right)$$

Equation 2.8 – Tafel Equation

Given the structure of both Equation 2.7 and Equation 2.8, it is clear that the operating temperature has a significant impact on the loss incurred at a given current. It must also be noted that due to the number of constants included in each of the equations (i_0, α, n, F, R) the temperature is one of the only non-material parameters which can be controlled to minimise the activation polarisation.

2.2.3 Ohmic Polarisation

In Equation 2.4 the Ohmic losses are represented by η_{ohm}. The Ohmic losses are a result of resistance to the flow of electrons and ions through all the fuel cell's components, namely the electrodes, electrolyte, GDLs, bipolar plates, interconnects and contact resistances [1] as seen in Equation 2.9.

$$\eta_{ohm} = iA\left(\sum_{k=1}^{n} r_k\right)$$

Equation 2.9 – Ohmic polarisation in a fuel cell

Where r_k is the resistance per unit area of each fuel cell component, k. Hence, the choice of materials and non-continuous contact between components have a significant effect in the Ohmic region. Ohmic resistances in PEMFCs are also dependent on the humidification of the electrolyte as ionic resistances decrease with increasing membrane hydration. Ohmic polarisation can be significantly changed while the fuel cell is in operation by altering temperature and humidity settings [17].

2.2.4 Concentration Polarisation

Concentration polarisation or mass transport losses arise from a lack of reactant at the electrode surfaces. In Equation 2.4 the mass transport losses are represented by η_{conc}.

The primary reasons for this are the limitation for the diffusion of gases, accumulation of liquid water resulting in pore blockages, build-up of inert gases, and blockages caused by impurities.

Hence, the diffusivity of the reactant gases, porosity, tortuosity and hydrophobicity of the GDL and catalyst layers, and reactant purity have a major influence in the mass transport region. The cathode side of the fuel cell causes greater mass transport limitations due to the lower diffusivity of oxygen in air relative to pure hydrogen and the more significant amount of liquid water.

The concentration polarisation is often described in terms of a mass-limiting current density, i_l, the current at which the rate of mass transport to the reactant surface becomes insufficient to sustain the rate of reaction. If it is assumed that the reaction only occurs at the catalyst layer interface, typical of high current densities, and neglecting kinetic effects, the concentration polarisation can be expressed in Equation 2.10.

$$\eta_{conc} = -\frac{\bar{R}T}{nF}\ln\left[1 - \frac{i}{i_l}\right]$$

Equation 2.10 – Concentration polarisation [1]

In reality, the reactant concentration, formation and accumulation of water droplets, and build of inert gas affects reaction kinetics so Equation 2.10 deviates from the assumption. To compensate for this, factors such as fuel cell geometry and materials must be considered, increasing the complexity of the equation. A semi-empirical approach can also be utilised to overcome this deviation, where a factor D is introduced based on experimental data, as seen in Equation 2.11.

$$\eta_{conc} = -D \ln\left[1 - \frac{i}{i_l}\right]$$

Equation 2.11 – Concentration polarisation based on experimentally determined constant

2.3 *In-situ* Diagnostic Techniques

Some of the common diagnostic techniques used to investigate *in-situ* fuel cell behaviour are discussed in this section. Electrical techniques are discussed first before exploring non-electrical diagnostics, from Section 2.3.6.

There are numerous non-electrical techniques that have been used for fuel cell diagnosis. Some of these techniques, which have been presented with respect to fuel cell diagnostics, are briefly introduced but non-electrical techniques are not limited to those outlined in this section.

2.3.1 Galvanostatic and Potentiostatic Techniques

There are numerous electrical diagnostic techniques to test fuel cells; the most common of which are potentiostatic or galvanostatic sweeps and holds. These tests are intended to measure the transient system performance when operating parameters are changed or for long-term testing to observe fuel cell performance over time.

In practice, the electrical output of a fuel cell would regularly be drawn through a load to utilise power from the fuel cell. However, in electroanalytical lab testing, the electrical output is usually put through a controlled electronic load, potentiostat, or galvanostat.

Potentiostats and galvanostats generally have five cables to measure properties of an electrochemical device: Working, counter, sensing, and reference electrode as well as a ground [18]. The current is measured between the working and counter electrodes while the voltage is measured between the sensing and reference electrodes. The ground can be used to connect the electrochemical device to the same ground as the measurement device.

A potentiostat effectively monitors the resistance of an electrochemical device and adjusts the current through a control amplifier to maintain a constant potential according to Ohm's law

$$V = iR$$

Equation 2.12 – Ohm's Law

Current can also be measured and converted into a voltage signal through application of a Hall Effect sensor. The Hall Effect is the production of a potential across a semi-conductor when placed perpendicular to a current which produces a magnetic field according to Ampère's Law.

This effect is crucial for measuring current without breaking a circuit and is applied in current probes for non-invasive measurement.

2.3.2 Current Interruption

Current interruption is a transient measure of the cell voltage after the electrical circuit is suddenly cut, stopping the flow of current.

The current interrupt technique can be used to determine the Ohmic resistances of a PEMFC [19]. The change in voltage is measured and a typical response can be seen in Figure 2.2. The immediate voltage drop is due to the purely Ohmic component of the impedance that is not coupled with a capacitance; a large portion of this will be the resistance of the electrolyte. The subsequent voltage change is due to the electrochemical overpotential [20], which dissipates at a slower rate due to the capacitance of the double-layer in parallel with the resistance to charge transfer and other relaxation processes, such as those associated with mass transport.

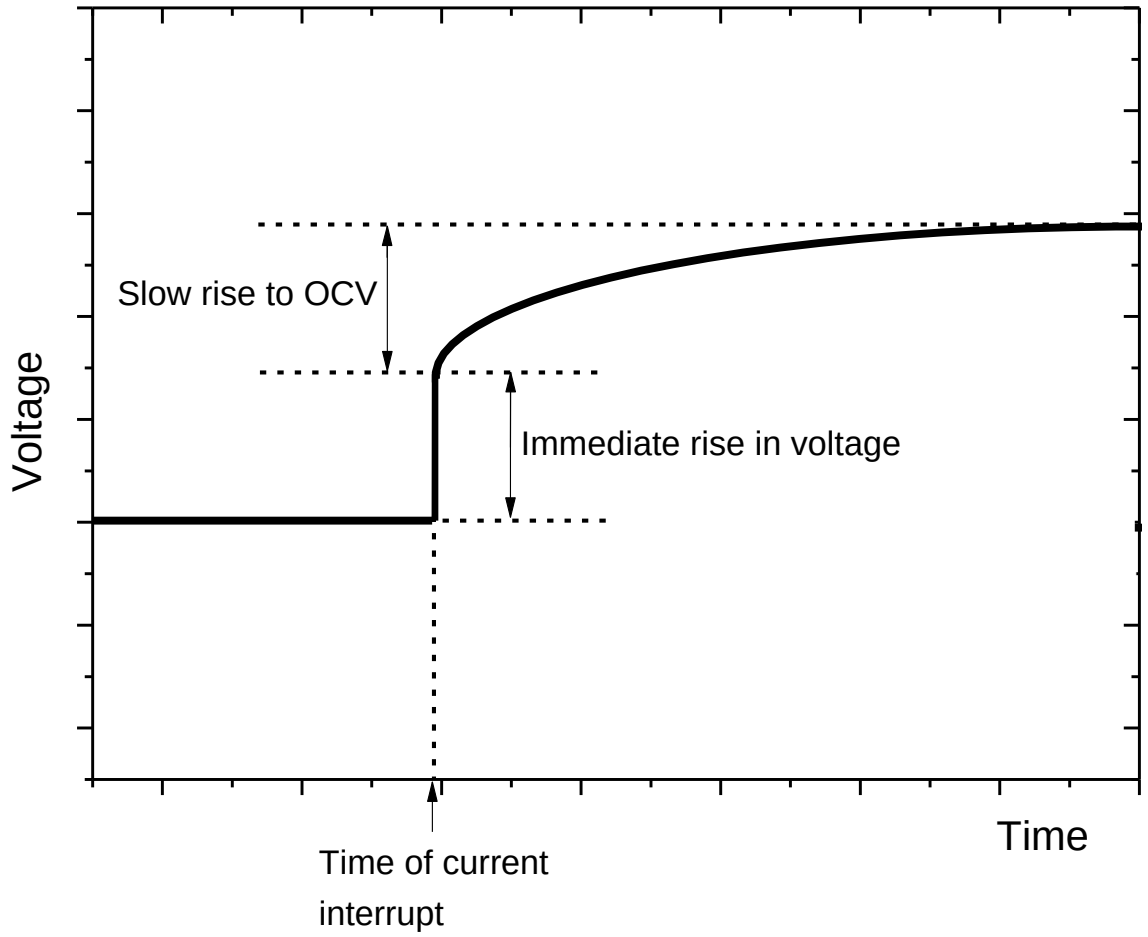

Figure 2.4 Typical voltage response using the current interruption technique. The initial rise in voltage is due to the Ohmic resistance. The subsequent, slower rise over the course of a few seconds to OCV is a result of the remaining overpotentials. [21].

Although this method is low cost, rapid and relatively easy to implement, it perturbs the system significantly as the delivery of current must be halted and returns the system to OCV.

2.3.3 Current Mapping

Current mapping is a technique by which the local current distribution of a fuel cell is measured. These sorts of measurements reveal the distribution of current over an electrode in a system. The ideal current mapping technique has high spatial resolution, real-time current response, is non-destructive to the MEA, and can be applied to multiple systems [6]. There are a number of ways to employ current mapping, such as the common method of segmenting the cell, such that the current drawn from each segment of the fuel cell is measured. However, this technique requires the altering of the GDL, BPPs, and current collection plates, as well as having low spatial resolution. This method is discussed more extensively in Chapter 4, Localised Electrochemical Impedance Spectroscopy Using a Novel Reference Electrode Array.

Other techniques employ Hall Effect sensors which reduce the possibility of lateral current flow but do not account for contact resistance between the BPP and GDL. The spatial resolution is also limited to the size of the magnetic loop sensor.

2.3.4 Electrochemical Impedance Spectroscopy (EIS)

EIS is a powerful transfer function diagnostic tool which can infer various performance losses in a fuel cell. A sinusoidal potential input is imposed on the system and the current response is measured (or vice versa). The current response is sinusoidal with the same frequency as the input potential [8, 19, 22, 23]. This input-output model is shown in Figure 2.5.

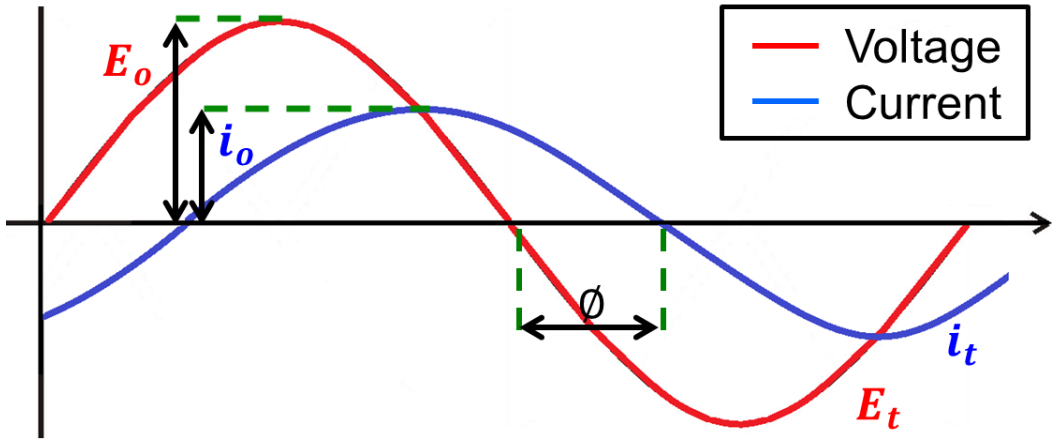

Figure 2.5 - Sinusoidal potential input with current response. EIS compares the imposed voltage signal E_t against the current response i_t at the same frequency to measure the phase shift (φ) and relative amplitude of the waves (E_o and i_o). Depending on the frequency of the imposed wave, the phase shift and amplitude ratio will change, revealing information about the fuel cell performance [2].

Impedance is similar to resistance apart from the fact that it is frequency dependent and considers both a real and imaginary component; hence it can give an idea of performance losses within a fuel cell with varying process time constants over a spectrum of frequencies. The impedance can be represented by the following equation:

$$Z(\varpi) = \frac{E_t}{i_t} = \frac{E_o}{i_o}\frac{e^{j\varpi t}}{e^{j\varpi t-\phi}} = \frac{E_o}{i_o}e^{\phi} = \frac{E_o}{i_o}(\cos(\phi) + j\sin(\phi))$$

Equation 2.13 – Electrochemical Impedance Spectroscopy relations

Where $Z(\varpi)$ is the frequency-dependent impedance term and the other parameters carry the same meaning as in Figure 2.5.

Hence the impedance can be described in terms of the relative amplitudes of the input and output and the phase shift alone. The results of EIS are usually plotted on Nyquist plots (discussed in Section 2.4.3.2) and using equivalent circuit analysis, the impedance associated with various fuel cell processes can be determined. The plotting of Nyquist plots from Equation 2.13 and application of EIS to PEMFCs is discussed in the Transfer Function section of this literature review, Section 2.3.4. Application of localised EIS is discussed in Section 4.1.

2.3.5 Cyclic Voltammetry

Cyclic voltammetry (CV) is a useful tool for evaluating the electrochemically active surface area of a fuel cell and other electrochemical devices. The technique requires ramping of the working electrode potential linearly with time. When a maximum specified voltage is reached, the potential is linearly decreased to the initial potential and this cycle is repeated as many times as specified. A voltammogram is a plot of the measured current density at the working electrode against the imposed potential [24].

Under CV, as the potential increases, the working electrode undergoes an oxidation process, increasing the anodic current until there are no more reactants that can be oxidised or the potential scan is reversed. If the redox reaction is reversible, as the

potential drops, reduction of the reactants occurs. Hence, CV is able to measure the redox potentials and reaction rates of an electrochemical device.

CV has been commonly applied *in-situ* to PEMFCs to determine the electrochemically active surface area (ECSA) of fuel cell electrodes [25-28]. This is achieved by measurement of the charge associated with the oxidation or reduction of the monolayer of absorbed species. This is the major assumption of ECSA; each proton is able to occupy one site on the active platinum surface and all of these sites are occupied during measurement.

The electrode of interest acts as the working electrode and is fed with an inert gas while the other electrode is supplied with hydrogen, acting as a pseudo-reference electrode.

The reductive reaction in this case is the desorption of hydrogen, and the oxidative is the adsorption of hydrogen on the catalyst layer, which both appear as peaks in a voltammogram as seen in Figure 2.6.

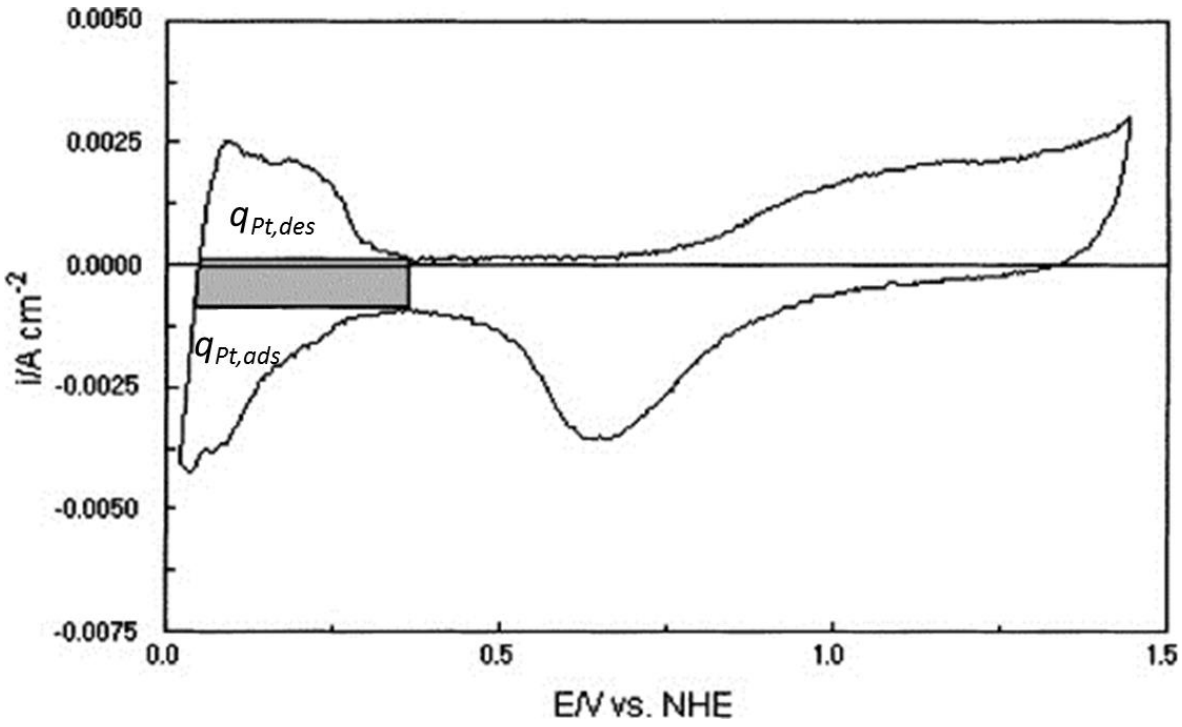

Figure 2.6 – Adapted from Pozio *et al.* [28]; Typical cyclic voltammogram (10 mV s^{-1}) of Pt/C. The adsorption integral, $q_{Pt,\ ads}$, and desorption integral $q_{Pt,\ des}$, represent the amount of charge exchanged during the adsorption and desorption of H_2 on Pt sites and the fill area is the contribution of double layer charge.

Integration of these peaks can estimate the electrochemically active surface area of the electrode according to Equation 2.14.

$$\text{ECSA}\ (\text{cm}_{Pt}^2\ \text{g}_{Pt}^{-1}) = \frac{q_{Pt}}{\Gamma \cdot L}$$

Equation 2.14 - Calculation of ECSA from voltammogram integral [29]

Where q_{Pt} is the integral of the peak, Γ is the charge required to reduce a monolayer of protons on platinum, and *L* is the platinum loading on the electrode.

More recently, Brightman *et al.* [30] and Lee *et al.* [31] developed a similar galvanostatic method to measure ECSA in stacks.

2.3.6 Neutron Imaging

Neutron Imaging has been used to map the water content in the flow-.field to see where blockages and diffusion problems may be occurring. In this technique, the fuel cell is placed into a collimated probing beam. While passing through the cell, the beam becomes attenuated depending on the local presence of attenuating materials (such as liquid water). The beam is then passed into a detector system to show where the attenuations have occurred.

Kramer et al. [32] showed the formation of liquid water in a PEMFC using neutron imaging, demonstrating that the amount of liquid water increased with increasing current density and dew point of the reactant gases.

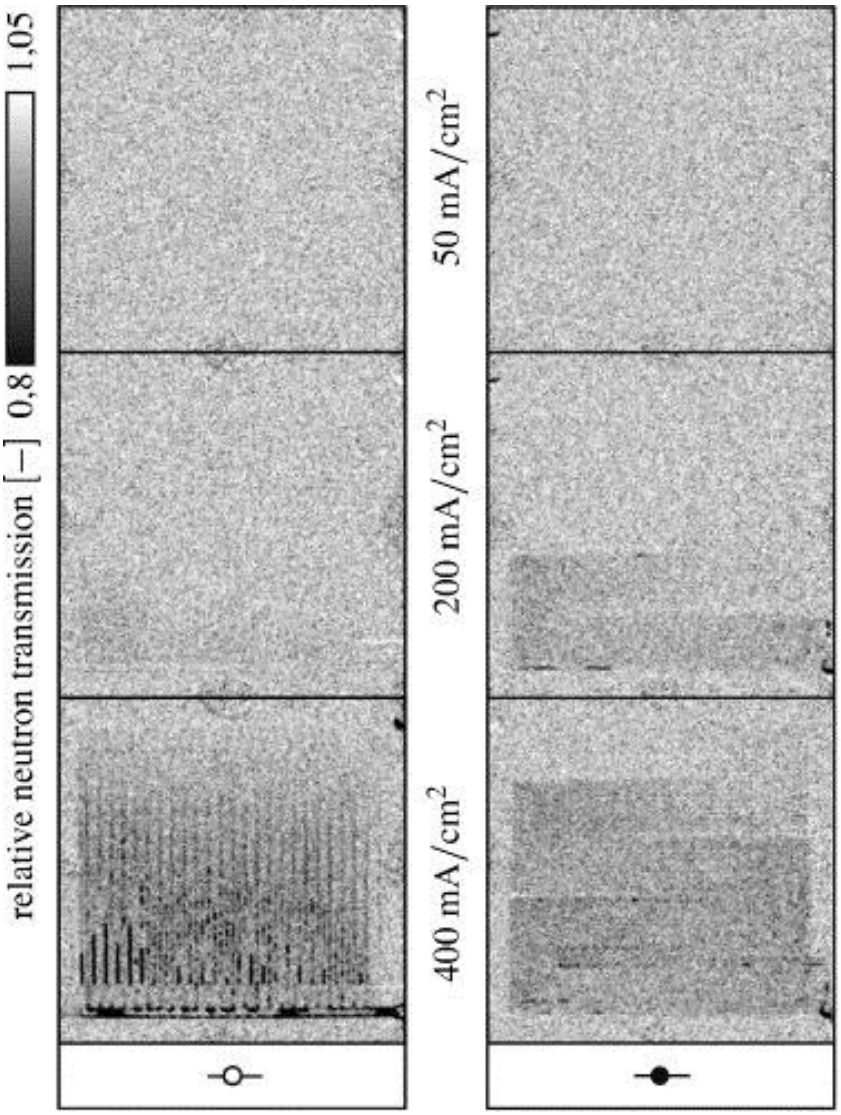

Figure 2.7 – From Kramer *et al.* [32]. Neutron images of a 50 finger interdigitated flow field (left) and 10 channel serpentine flow field (centre) at 50, 200, and 400 mA cm^{-2} with a 1 s exposure time.

Pekula *et al.* [33] then showed time-resolved neutron images to demonstrate the onset of flooding when polarising a PEMFC. Since then, there have been numerous studies exploring the application of neutron imaging techniques including high resolution, in-plane studies observing water formation on the cathode as far more limiting than that on

the anode [34], dependency of fuel cell edges on water management [35], investigation of water formation in cold start conditions [36], mapping water formation [37, 38], effects of GDL properties on water management [39], and hydrogen starvation in dead-ended operation [40]; when hydrogen is supplied to the anode periodically by operating a solenoid valve at the outlet, thus changing the hydrogen concentration throughout a purge cycle.

2.3.7 Optical techniques

The use of a PEM fuel cell with an optical window allows for liquid water dynamics in the flow-field to be recorded with a camera. The optical window can be made out of a number of transparent materials such as quartz, polycarbonate, or acrylic and can be used for individual visualisation of the anode and cathode. This principle was applied to observe flooding on the cathode under carrying humidity and stoichiometric conditions [41].

Spernjak *et al.* [42] developed an optically transparent fuel cell to evaluate the effectiveness of different GDL and MPL materials. This technique demonstrated that water formation does occur on the anode when the osmotic pressure caused by water formation on the cathode is great enough to drive water through the membrane. They then applied complementary neutron imaging [43] to show white-light and neutron images of static water under lands on the cathode of a PEMFC as a function of current density and different GDL & MPL materials.

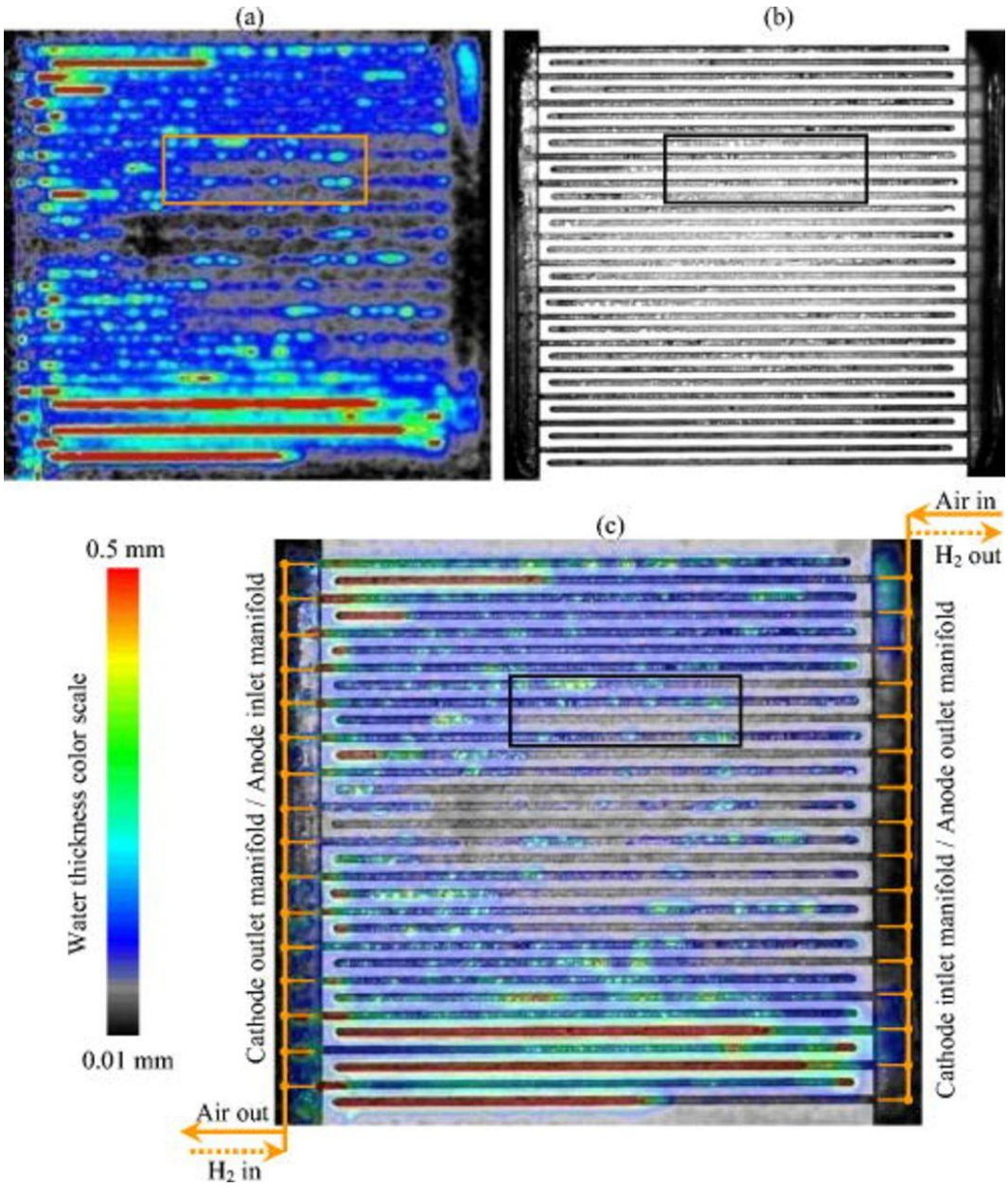

Figure 2.8 – From Spernjak *et al.* [43], channel flooding on the cathode. Corresponding neutron and cathode optical images for interdigitated flow field with untreated Toray paper as the GDL. Processed neutron image (a), optical image (b) of the cathode, and neutron image overlaid on the concurrent optical image (c).

2.3.8 Temperature Mapping

Temperature mapping of a fuel cell can be conducted by placing thermocouples in various positions of the gas flow fields to determine where more reactions are occurring and hence where mass transport limitations are becoming an issue in fuel cell performance. This technique is able to show a spatial measure of fuel cell performance as the reactants move through the flow-field, as opposed to most electrical techniques which show the performance of the unit as a system. This has been demonstrated on both cell [44, 45] and stack level [46, 47] and demonstrated temperature variations over 10 °C within a system.

This technique was more recently demonstrated alongside current mapping to show variations in localised temperature and current density while a fuel cell is operated in a dead-end mode [48], demonstrating the dependency of these operating parameters on hydrogen concentration.

2.3.8.1 Thermal Imaging

Thermal imaging, or infrared (IR) thermography, is a widely used diagnostic technique which uses infrared radiation emitted from surfaces to accurately measure temperature, often through the use of a semiconducting detector [49, 50]. Unlike temperature mapping, which uses thermocouples in pre-determined locations, thermal imaging allows

for a higher spatial resolution. Moreover, it is a non-invasive technique which may capture dynamic thermal changes in fuel cell operation.

The technique can infer surface temperature of objects based on the fact that all objects above 0 K emit some infrared radiation [51]. The wavelength of this radiation is slightly higher than that of visible light and can be described by Planck's law of thermal radiation which relates temperature to the radiant flux emitted from a black body.

$$B_\lambda(T) = \frac{2hc^2}{\lambda^3} \frac{1}{e^{\frac{hc}{\lambda k_B T}} - 1}$$

Equation 2.15 - Planck's law [49]

With increasing temperature, more thermal radiation is emitted and the peak wavelength of the radiation decreases. Some objects glow when sufficiently heated due to the fact that the peak wavelength has decreased sufficiently to appear in the visible spectrum. Estimating the peak wavelength is critical to tuning thermal imaging equipment for suitable temperature ranges and can be described using Wien's displacement law.

$$\lambda_{max} = \frac{b}{T} = \frac{2900\ \mu\text{m K}}{T}$$

Equation 2.16 - Wien's displacement law [49]

The equation demonstrates the inverse relationship between temperature and wavelength, multiplied by a factor *b*, Wien's displacement constant.

In order for the infrared radiation to be measured and recorded, it must first pass through a focal lens. Due to the fact that glass absorbs long wavelength infrared radiation, the lens is often made of germanium or sapphire which are more IR-transparent materials, contributing to the higher cost of the thermal imaging camera.

The IR radiation can then be converted to an electrical signal in an array of photodetectors based on a narrow gap semiconductor. These semiconductors often operate at low temperatures (4 – 100 K) to obtain high-resolution thermal images. Without the cooling, the semiconductors would become saturated with their own radiation.

The Stefan-Boltzmann law relates the power radiated from a black body to its temperature. However, as most objects measured with an IR camera are not black bodies, the emissivity of the object must be considered. The emissivity, ε, is the ratio of the radiant energy given off by an object to the radiant energy given off by a black body at the same temperature. The relationship between an object's radiation, emissivity and temperature is given by Equation 2.17.

$$j^* = \varepsilon\sigma T^4 = (5.670373 \times 10^{-8}\mathrm{W\ m^{-2}K^{-4}})\ \varepsilon T^4$$

Equation 2.17 – Stefan – Boltzmann law [49]

Because the relationship between the IR measured and the temperature is exponential to the power of 4, it is crucial to measure accurately the emissivity of the object observed in order to achieve a reliable temperature measurement.

Thermal imaging has previously been demonstrated on a range of electrochemical devices; however, due to the fact infrared imaging is a surface measurement, modifications must often be made to the design of cells and stacks in order to image the regions of interest; typically, the MEA.

Hajenkos *et al.* [52] designed a cell which enabled infrared imaging of the cathode using a transparent back plate in order to investigate the coupled effects of flooding, current distribution and temperature in a PEMFC *in operando*. The added value of using thermography is the spatial resolution of the temperature measurement over a large area, enabling researchers to find limitations in single cell PEMFC models which assume isothermal behaviour [53], and spatial variations in air-cooled industrial stacks [54].

IR thermography has enabled the development and validation of more comprehensive PEMFC models which show thermal interaction within a cell and between cells in a stack [55-57], enabling the reliable optimisation of fuel cell performance based on computational data [56]. It has led to the identification of a 'polarisation area' [58] as a more effective way of describing performance due to the uncertainty in controlling the temperature of a commercial stack.

2.4 Transfer Function Analysis

Transfer function analysis has been applied as a diagnostic tool for PEMFCs previously, as mentioned in Section 2.3.4, EIS. The principle of transfer function analysis is the description of the frequency dependent relationship between a sinusoidal input imposed on a system and the measured response at the same frequency. The application of a periodic stimulus at a chosen frequency enables the investigation of individual physical system properties if there is a difference in their characteristic frequency such that the feature can be adequately separated. For example, using EIS, Ohmic resistances occur very quickly hence they appear at high frequencies, whereas mass transport limitations are limited by diffusion and appear at lower frequencies.

Moreover, when measuring a response at the same frequency as the applied stimulus, there is a greater confidence that the measured response is a direct effect of the applied stimulus. The only exception to this rule is if there is noise in the system occurring at the same frequency, distorting the response.

Beyond EIS, which both imposes and measures an electrical property of a PEMFC, a number of other manipulable and measureable parameters have been identified which can deduce further information from a fuel cell system. Before exploring what transfer function analysis has revealed about PEMFC performance, and the possible cause and effect relationships to be investigated, the fundamentals of transfer function analysis are discussed in this section.

2.4.1 Conditions of Validity

The validity of transfer function analysis is dependent on the response of a system to be linear and time-invariant to an input stimulus [59]. Linearity signifies that an input *x(t)* will yield a response *y(t)* from the system. The input and response can be scaled such that an input $A \cdot x(t)$ will yield a response $A \cdot y(t)$, and summed such that an input $A_1 \cdot x_1(t) + A_2 \cdot x_2(t)$ will yield a response $A_1 \cdot y_1(t) + A_2 \cdot y_2(t)$.

Time-invariance signifies steady state behaviour; that an input *x(t)* will yield a response *y(t)*, regardless of the time delay in input to the system. That is to say if time *T* elapses, input *x(t+T)* will yield a response *y(t+T).*

2.4.2 Calculating Transfer Functions

Consider the system in Figure 2.9. An input signal or forcing function, *f(t)*, is transformed within a system to give an output signal *y(t).* In order to introduce the transfer function, the model must be transformed from the time domain into the frequency domain [59-61]. A Laplace transform of the input and output signals will give the signals in the frequency domain.

Fourier Transforms could also be applied to characterise the signals in the frequency domain as they only consider the steady state signal as opposed to Laplace which also takes a transient signal into account [62]. Fourier transforms are a powerful analytical tool which can quickly relate the input and output signals of a steady-state system.

However, for the scope of this work, Laplace transforms are applied to demonstrate the mathematics of the system which may include a transient step.

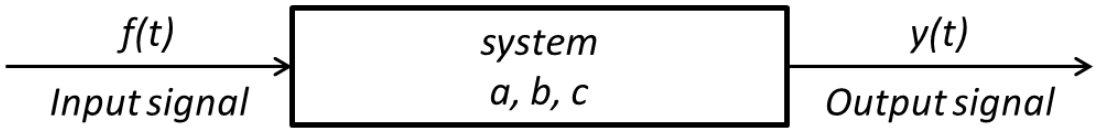

Figure 2.9 - Block Diagram of an input-output relationship in time domain.

If we assume a second order differential equation in the time domain,

$$a\frac{d^2y}{dt^2} + b\frac{dy}{dt} + cy = f(t)$$

Equation 2.18 – Time-dependent second order differential equation

Taking the Laplace transform of the differential, the system is described in the frequency domain,

$$(as^2 + bs + c)Y(s) = F(s)$$

Equation 2.19 – Frequency-dependent second order differential equation

Where $\mathcal{L}\{f(t)\} = F(s)$ and $\mathcal{L}\{y(t)\} = Y(s)$. The transfer function can then be defined as the ratio of the Laplace transforms of the output signal and input signal,

$$H(s) \equiv \frac{Y(s)}{F(s)} = \frac{1}{as^2 + bs + c}$$

Equation 2.20 – Transfer function of a second order system

Now consider EIS where a sinusoidal potential input is imposed on the system and the current response is monitored. The sinusoidal input, $f(t) = A\sin\varpi t$, will yield a current response in the frequency domain *Y(s),*

$$Y(s) = H(s)F(s) = H(s)\frac{A\varpi}{s^2 + \varpi^2}$$

Equation 2.21 – General response of a system to a sinusoidal stimulus

To derive a transfer function, *H(s)*, as an example, we consider a resistor, of resistance *R*, in series with a capacitor, with capacitance *C,* to relate the potential and current,

$$E(t) = i(t)R + \frac{Q(t)}{C} = i(t)R + \frac{\int_0^t i(t)dt}{C}$$

Equation 2.22 – Time-dependent expression of a resistor in parallel with a capacitor

Taking the Laplace transform of this term,

$$E(s) = i(s)R + \frac{i(s)}{sC} = i(s)(R + \frac{1}{sC})$$

Equation 2.23 – Frequency-dependent expression of a resistor in parallel with a resistor

$$i(s) = E(s)/(R + \frac{1}{sC})$$

Equation 2.24 – Isolation of current term in Equation 2.23

The transfer function, or impedance in this case as resistance is potential divided by current,

$$Z(s) = \frac{E(s)}{i(s)} = \frac{i(s)(R + \frac{1}{sC})}{i(s)} = R + \frac{1}{sC}$$

Equation 2.25 – Impedance of a resistor and capacitor in series expressed as a transfer function

Hence, in general, a contribution to impedance for a resistor can be expressed as *R* and for a capacitor *1/sC* [63]. So if for a typical fuel cell, we consider a resistor (Ohmic resistances)

in series with a capacitor (double-layer with capacitance *C*) and resistor (charge transfer resistance) in parallel, the impedance can be represented as

$$Z(s) = R_s + \frac{1}{(\frac{1}{R_{CT}} + sC_{DL})}$$

Equation 2.26 – Impedance of a typical fuel cell expressed as a transfer function

Now applying this transfer-function to Equation 2.21, the general transfer-function equation with a sinusoidal input, the current response can be predicted. By applying a sinusoidal signal to the potential of magnitude E_o and angluar frequency $\varpi = 2\pi f$, the potential becomes $E = E_o \sin(\varpi t)$. The current response can be predicted given the potential and impedance. Since $\mathcal{L}[\sin \varpi t] = \varpi/(s^2 + \varpi^2)$,

$$i(s) = \frac{E_o \varpi}{(s^2 + \varpi^2)} \frac{1}{R_s + \frac{1}{(\frac{1}{R_{CT}} + sC_{DL})}}$$

Equation 2.27 – EIS current response of a typical fuel cell

Equation 2.27 becomes

$$i(s) = \frac{E_o \varpi (1 + sR_{CT}C_{DL})}{(s^2 + \varpi^2)(R_s + R_{CT} + sR_sR_{CT}C_{DL})}$$

Equation 2.28 – EIS current response after multiplying terms

$$i(s) = E_o\left(\frac{\varpi}{(s^2+\varpi^2)(R_s+R_{CT}+sR_sR_{CT}C_{DL})} + \frac{\varpi s R_{CT}C_{DL}}{(s^2+\varpi^2)(R_s+R_{CT}+sR_sR_{CT}C_{DL})}\right)$$

Equation 2.29 – EIS current response isolating E_o

Taking the inverse Laplace transform will give the output signal in the time domain.

$$i(t) = \frac{E_o}{\kappa}\left[\left(\varpi^2 R_s {R_{CT}}^2 {C_{DL}}^2 + R_s + R_{CT}\right)\sin(\varpi t) + \varpi {R_{CT}}^2 C_{DL}\cos(\varpi t) - \varpi {R_{CT}}^2 C_{DL} e^{\frac{-(R_s+R_{CT})t}{R_sR_{CT}C_{DL}}}\right]$$

Equation 2.30 – EIS current response in terms of factor κ

Where

$$\kappa = \varpi^2 {R_s}^2 {R_{CT}}^2 {C_{DL}}^2 + {R_s}^2 + 2R_sR_{CT} + {R_{CT}}^2$$

Equation 2.31 – Factor κ of Equation 2.30

The third term in Equation 2.30 (the exponential), is a transient response and decreases quickly to zero. Hence at steady state,

$$i_{ss}(t) = \frac{E_o}{\kappa}\left[\left(\varpi^2 R_s {R_{CT}}^2 {C_{DL}}^2 + R_s + R_{CT}\right)\sin(\varpi t) + \varpi {R_{CT}}^2 C_{DL}\cos(\varpi t)\right]$$

Equation 2.32 – Current response at steady state

Since $a_1 \cos b + a_2 \sin b = a_3 \sin(b + \phi)$, where φ the phase angle between the input and response, is $\tan^{-1}\left[\frac{a_1}{a_2}\right]$ and $a_3 = \sqrt{a_1^2 + a_2^2}$,

$$i_{ss}(t) = \frac{E_o \beta}{\kappa}[\sin(\varpi t + \varphi)]$$

Equation 2.33 – Current response after applying trigonometric identity

Where

$$\beta = \sqrt{\left(\varpi^2 R_s {R_{CT}}^2 {C_{DL}}^2 + R_s + R_{CT}\right)^2 + \left(\varpi {R_{CT}}^2 C_{DL}\right)^2}$$

Equation 2.34 – β in Equation 2.33

And

$$\varphi = \tan^{-1}\left[\frac{\varpi^2 R_s {R_{CT}}^2 {C_{DL}}^2 + R_s + R_{CT}}{\varpi {R_{CT}}^2 C_{DL}}\right]$$

Equation 2.35 – φ, the phase shift in Equation 2.33

This, as expected, is a sinusoidal response to the original sinusoidal input with the same frequency. Hence the phase shift and amplitude ratio can be used to plot a transfer function.

2.4.3 Interpreting Transfer Functions

There are two common methods of interpreting transfer function behaviour as a function of frequency: Bode and Nyquist Plots.

2.4.3.1 Bode Plots

The Bode plot is a semi-log plot of the log of the amplitude ratio (gain curve) and phase angle (phase curve) plotted against a logarithmic frequency scale. The advantage of the Bode Plot is that the frequencies of the poles and zeros of the transfer functions can be identified based on frequencies where the slope of the Bode Plot changes.

As an example, consider the transfer function of a first order system [64]:

$$(s) = \frac{K_p}{\tau_p s + 1}$$

Equation 2.36 – Transfer function of a first order system[64]

Where K_p is the system gain, and τ_p is the time constant of the first order process.

If we consider a sinusoidal input,

$$Y(s) = H(s)F(s) = \frac{K_p}{\tau_p s + 1} \frac{A\varpi}{s^2 + \varpi^2}$$

Equation 2.37 – Response of a first order system

Splitting into fractions,

$$Y(s) = \frac{K_p A}{{\tau_p}^2 \varpi^2 + 1} \frac{\varpi}{s^2 + \varpi^2} - \frac{K_p A \varpi \tau_p}{{\tau_p}^2 \varpi^2 + 1} \frac{s}{s^2 + \varpi^2} + \frac{K_p A \varpi \tau_p}{{\tau_p}^2 \varpi^2 + 1} \frac{1}{s + \frac{1}{\tau_p}}$$

Equation 2.38 – Response of a first order system split into three terms

And taking the inverse Laplace transform,

$$Y(t) = \frac{K_p A}{{\tau_p}^2 \varpi^2 + 1} \sin(\varpi t) - \frac{K_p A \varpi \tau_p}{{\tau_p}^2 \varpi^2 + 1} \cos(\varpi t) + \frac{K_p A \varpi \tau_p}{{\tau_p}^2 \varpi^2 + 1} e^{-t/\tau_p}$$

Equation 2.39 – Time-dependent response of a first order system

The third term is a transient response and decreases quickly to zero. The steady state value of the response is,

$$Y_{ss}(t) = \frac{K_p A}{{\tau_p}^2 \varpi^2 + 1} \sin(\varpi t) - \frac{K_p A \varpi \tau_p}{{\tau_p}^2 \varpi^2 + 1} \cos(\varpi t)$$

Equation 2.40 – Time dependent response of steady state first order system

Since $a_1 \cos b + a_2 \sin b = a_3 \sin(b + \phi)$, where $\varphi = \tan^{-1}\left[\frac{a_1}{a_2}\right]$ and $a_3 = \sqrt{a_1^2 + a_2^2}$,

$$Y_{ss}(t) = \frac{K_p A}{\sqrt{{\tau_p}^2 \varpi^2 + 1}} \sin(\varpi t + \phi)\,;\ \phi = \tan^{-1}(-\varpi \tau_p)$$

Equation 2.41 – Time dependent response of a steady state first order system

Hence the amplitude ratio is

$$|H(s)| = \frac{|Y|}{|F|} = \frac{\frac{K_p A}{\sqrt{{\tau_p}^2 \varpi^2 + 1}}}{A} = \frac{K_p}{\sqrt{{\tau_p}^2 \varpi^2 + 1}}$$

Equation 2.42- Amplitude ratio of a first order system

And the phase angle is

$$\phi = \tan^{-1}(-\varpi \tau_p)$$

Equation 2.43 – Phase shift of a first order system

With these expressions, the Bode plot can be constructed, as shown in Figure 2.10.

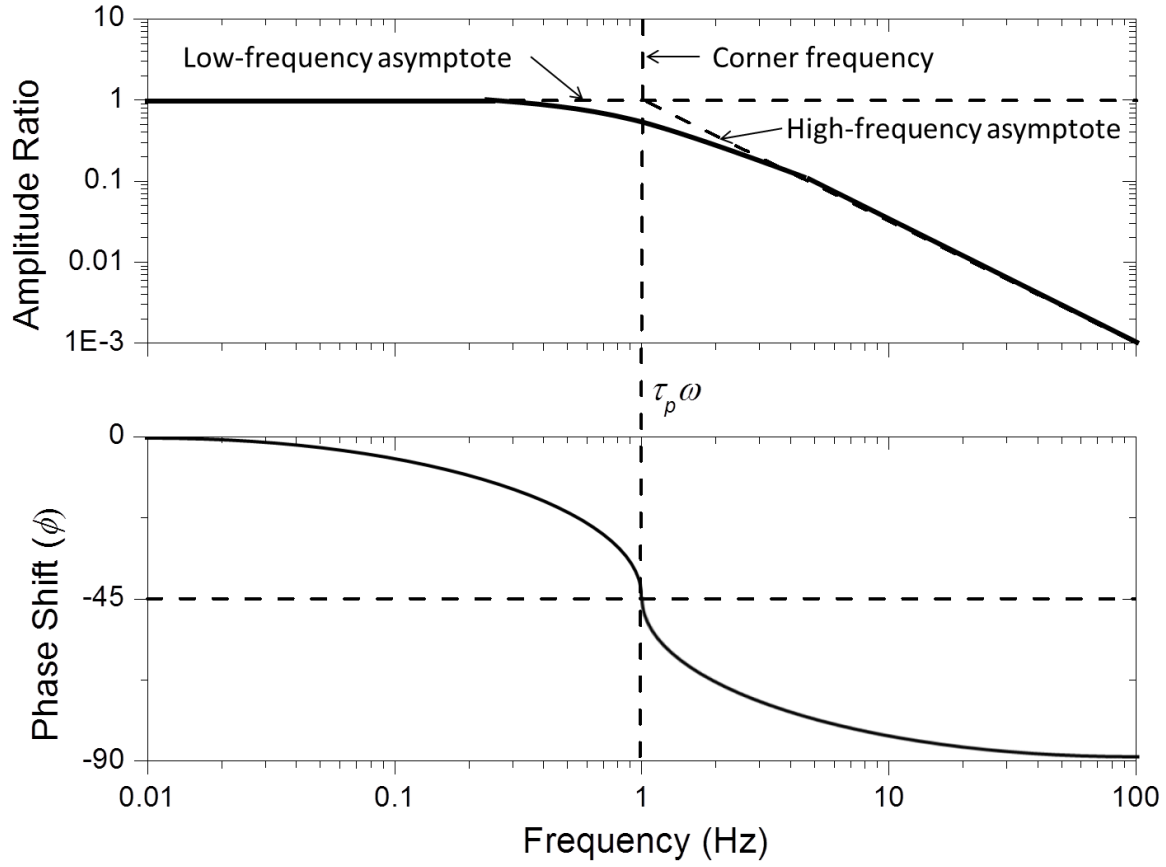

Figure 2.10 - Bode Plot for a first order system. The amplitude ratio is shown on a log-log plot on the top based on Equation 2.42. The phase-shift is shown on a semi-log plot below based on Equation 2.43. Corner frequencies are indicative of where there is a change in the dominant effect of the system [64].

A major point of interest is the corner frequency, $\tau_p \, \varpi$ in the case of a first order process, which is where the characteristics of the transfer function change between high and low frequencies. This is due to the fact that the system response to the perturbation no longer has sufficient time to deliver its maximum output.

2.4.3.2 Nyquist Plots

A Nyquist Plot is a parametric graph which plots the real component of the transfer function against the imaginary component. The major disadvantage of the Nyquist Plot is that individual frequencies are not inherently expressed as each frequency is represented by a point on the Nyquist Plot. However, it is particularly useful when performing EIS as different curves can deduce various resistances and capacitances in a fuel cell.

The Nyquist Plot can be made based on the magnitude and argument of the transfer function. The argument will give the angle between the x - axis and the line segment from the origin to the point. The magnitude will determine the distance of the point from the origin.

If we consider EIS, the potential input can be represented by $E_t = E_o \sin(\varpi t) = E_o e^{j\varpi t}$ and the current response can be represented as $I_t = I_o \sin(\varpi t - \phi) = I_o e^{j\varpi t - \phi}$. The transfer function is then,

$$Z(\varpi) = \frac{E_t}{I_t} = \frac{E_o}{I_o} \frac{e^{j\varpi t}}{e^{j\varpi t - \phi}} = \frac{E_o}{I_o} e^{\phi} = \frac{E_o}{I_o} (\cos(\phi) + j \sin(\phi))$$

Equation 2.44 – Simplified transfer function of EIS

Hence,

$$\arg Z(\varpi) = \tan^{-1}\frac{\sin(\phi)}{\cos(\phi)} = \tan^{-1}(\tan\phi) = \phi$$

Equation 2.45 – Argument of impedance term in Equation 2.44

And

$$|Z(\varpi)| = \sqrt{\left(\frac{E_o}{I_o}\cos(\phi)\right)^2 + \left(\frac{E_o}{I_o}\sin(\phi)\right)^2} = \sqrt{\left(\frac{E_o}{I_o}\right)^2(\cos^2(\phi) + \sin^2(\phi))} = \frac{E_o}{I_o}$$

Equation 2.46 – Magnitude of impedance term in Equation 2.44

A typical Nyquist Plot for a fuel cell electrode is shown in Figure 2.11.

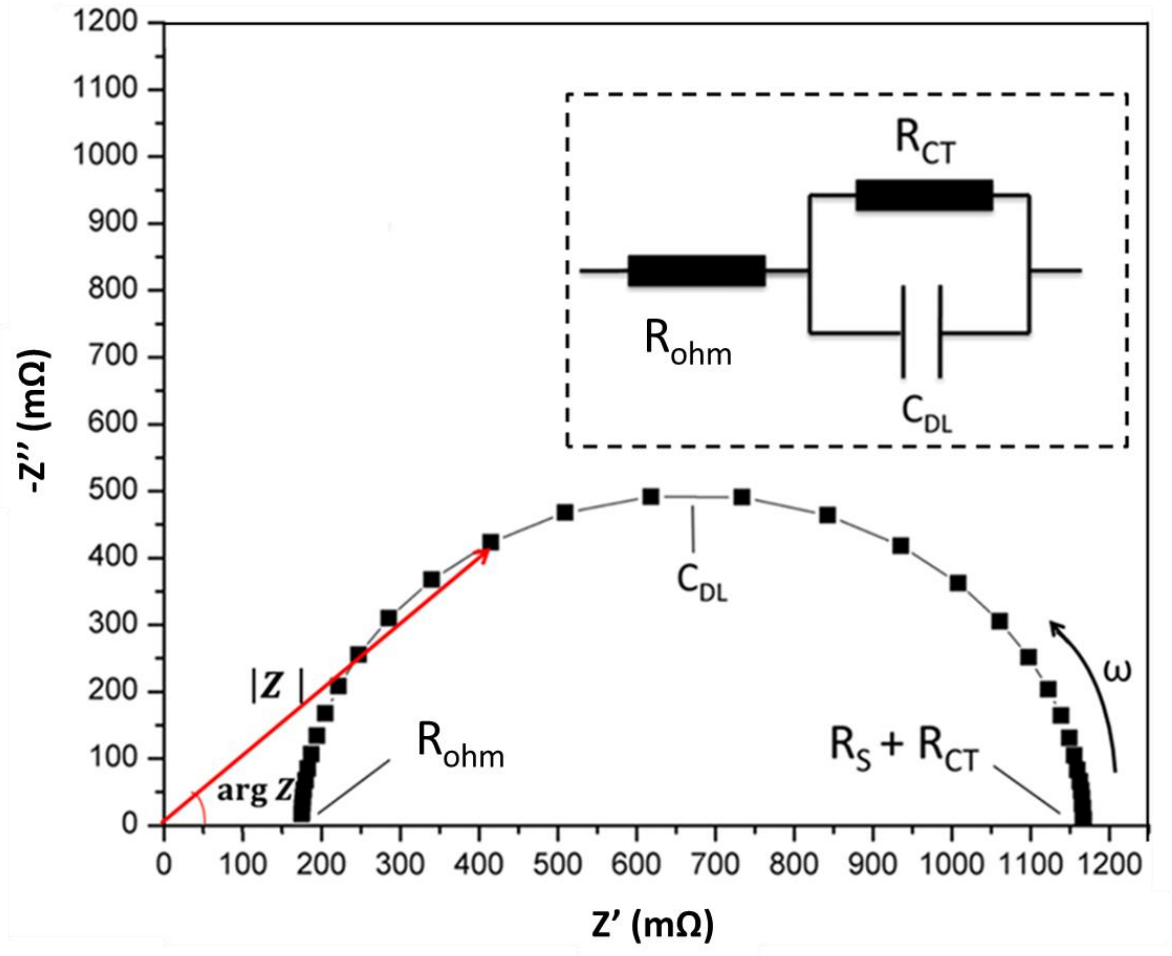

Figure 2.11 – Nyquist Plot for a dummy fuel cell electrode adapted from Reece [22] with a one electrode and electrolyte equivalent circuit (inset). The amplitude ratio is plotted as distance from the origin based on Equation 2.46 and the corresponding phase shift is used as an angle from which a point is plotted from the x-axis based on Equation 2.45. Because Ohmic, kinetic, and mass transport activities of a fuel cell are dominant at different frequencies, an arc or multiple arcs are visible on the Nyquist Plot. Typical frequencies increase from 100 mHz (the intercept with the x-axis toward the right) to 1 kHz (the intercept with the x-axis toward the left).

The equivalent circuit in Figure 2.11 shows how the Ohmic resistances (R_S), capacitance of the double-layer (C_{DL}), and charge transfer resistance (R_{CT}) appear on a Nyquist Plot. At higher frequencies, only Ohmic resistances are observed, so the high frequency (HF) intercept is indicative of the Ohmic resistances in the system. As the frequency decreases, charge transfer and mass transfer resistances are observed, as they occur more slowly in the time domain. The low frequency (LF) intercept is indicative of the total resistances in the system.

2.4.4 EIS applied to PEMFCs

EIS is the most widely applied transfer-function diagnostic technique applied to PEMFCs. In order to make a sound inference of physical properties, the equivalent circuit must be considered. The equivalent circuit has been demonstrated to be a function of polarisation [65] due to the appearance of single or multiple arcs in an EIS Nyquist Plot. The way equivalent circuits are generally applied is as follows:

- The electrolyte is represented by a resistor, representing Ohmic resistances in the membrane
- The electrodes are individually represented by a resistor and capacitor in parallel, representing the properties of the double-layer formed on each electrode's surface. Because these occur at similar frequencies for both electrodes, usually only a single arc appears on a Nyquist plot. Because anode kinetics for PEMFCs are considered facile relative to the cathode, one electrode is designated in the

equivalent circuit and the contribution to the impedance is attributed to the cathode. This assumption has been challenged [66] and can be circumvented with the introduction of a reference electrode.

- At higher current densities, an additional resistor in parallel with the capacitor can be added to the equivalent circuit as another arc appears due to mass transport limitations. This resistance is representative of the increased impedance brought on by the decrease in partial pressure of reactants and blocking of reaction sites due to water formation.

EIS has been applied to optimize the properties of the MEA of a PEMFC. It was shown that the charge transfer resistance decreases with increasing platinum loading on the electrodes [67], although this is, of course, a trade-off with the cost of the device. Increasing Nafion content in the electrode was found to decrease Ohmic resistances up to a point, before increasing mass transport resistances [68].

With respect to the membrane, it was shown that the thinner the membrane, the lower the Ohmic resistance, as well as decreasing dependence on gas humidification and temperature [69]. This however, leaves the MEA more susceptible to gas crossover.

One of the most investigated parts of the fuel cell with respect to EIS is the GDL due to its influence on mass transport limitation and membrane hydration. The GDL holds liquid water, aiding in membrane hydration and thus lower Ohmic resistances; however, this blocks reaction sites and increasing the mass transport overpotential. The porosity and

structure of the GDL have been computationally and experimentally evaluated to investigate the trade-off between these two parameters [70-72].

The compression of the GDL also affects fuel cell performance as increased compression improves contact resistance but eventually starts crushing the GDL and blocking reactant pathways [73, 74].

EIS has also been applied to measure the effect of gas contamination on fuel cell performance. One of the most common contaminants in hydrogen as a result of the reforming process from which most commercially available hydrogen is produced is CO. It was found that a feeding dilute amount (typ. > 10 ppm) of CO in the hydrogen stream to the fuel cell increases the charge transfer resistance due to the absorption of CO on the catalyst surface. This blocks reaction sites and also affects unblocked sites through dipole interactions [75].

2.4.5 Dynamic Mechanical Analysis applied to PEMFC materials

Dynamic mechanical analysis (DMA) is a transfer function between the stress and the strain of a material which can reveal viscoelastic properties. The stress is imposed on the material by applying a normal force sinusoidally and the strain is measured as the displacement caused by the applied perturbation. These responses are measured at a range of temperatures as the viscoelastic properties are heavily dependent on this variable [76]. When applied to PEMFCs, DMA is primarily used to study the viscoelastic properties of the electrolyte *ex-situ.*

2.4.6 Scope for novel transfer function analysis applied to fuel cells

A matrix of transfer functions was constructed based on known performance parameters of PEMFC operation. Five system perturbations were selected: thermal, chemical, mechanical, electrical, and pneumatic. Six system response measurements were also considered: thermal, chemical, mechanical, electrical, pneumatic, and acoustic. The intersection of each cause and effect was evaluated and the possible PEMFC phenomena one would expect to be perturbed and be able to measure were hypothesised in each box.

The transfer functions to pursue were selected based on the impact on fuel cell performance and availability of equipment. Within this project, conventional EIS was also selected and applied in a novel way in order to enhance current understanding of fuel cell performance.

Electro-Thermal Impedance Spectroscopy (ETIS) was selected as a novel transfer function to be investigated. There is a strong relationship between current and temperature [52, 57, 58] which can reveal thermal properties of the materials the current and heat must pass through, including water produced by the fuel cell. In addition, the availability of a potentiostat to induce electrical perturbations, a thermal imaging camera with lock-in capabilities, and an air-breathing cathode PEM fuel cell made the development of ETIS logistically feasible.

Electrochemical Pressure Impedance Spectroscopy (EPIS) was also selected due to the ability to further study water management from a pneumatic, rather than thermal perspective. Several methods of pressure perturbation were attempted before

successfully implementing a system incorporating an acoustic speaker to produce rapid pressure perturbations.

Other transfer function techniques were attempted with limited success due primarily to the lack of sinusoidal periodicity in the tuning of thermal and mechanical system perturbations.

		Method – Imposing PEMFC Stimulus				
		Thermal - Heat Transfer	**Chemical** – Stoichiometry	**Mechanical** - Stress	**Electrical** – Voltage/ Current	**Pneumatic** – Flow/ Pressure
Method - Measuring PEMFC Response	**Thermal** Heat Transfer		Reaction stoichiometry and water management	Heat transfer properties may vary, water management	Variations show water management, active areas	Variation will affect temperature, water management
	Chemical CO_2 sensor	Catalyst degradation can be inferred via CO_2 evolution	Catalyst degradation can be identified		Catalyst degradation observed if the cell operates near OCV	Catalyst degradation may occur if carbon in catalyst reacts with water
	Mechanical Strain	Can cause thermal expansion of GDL/membrane, change heat transfer properties	Membrane water content and mass transport properties vary	Dynamic Mechanical Analysis		Mass transport properties in GDL, membrane water content
	Electrical Voltage / current	Reaction kinetics, water management, mech. failure due to membrane drying	Water management variations may be observed	Water management, GDL mass transport will vary	Electrochemical Impedance Spectroscopy	Reactant starvation at electrodes, water management in channels
	Pneumatic Pressure and Flow	Reaction kinetics and water management variations may be observed with thermal expansion	Reaction kinetics and water management variations	GDL mass transport property variations can be observed	Reaction kinetics and water management variations may be observed	Flow variation will affect the osmotic pressure and mass transport properties
	Acoustic Acoustic Emission	Temperature variation can alter water management, mechanical failure due to membrane drying	Reaction stoichiometry variation will affect water management	Water management changes with compression, mechanical failure may be observed	Electrical characteristics affect water management	Water management affected due to varying reactant flow

Table 2.2– Method-method matrix of transfer functions considered. The cells highlighted in green are well-established techniques that have been widely reported on, not necessarily in the field of fuel cells. The cells highlighted in yellow are the novel transfer function techniques applied to PEMFCs in this research.

2.5 Summary

The main factors affecting PEMFC performance were discussed in this chapter including activation polarisation, dependent primarily on reaction kinetics, Ohmic polarisation, dependent primarily on membrane hydration, and mass transport limitations, dependent on reactant availability and water management.

Then, the operating principles of a range of existing diagnostic techniques were discussed. The application of these techniques to PEMFCs was introduced with some results of PEMFC performance, particularly as it pertains to water management and membrane hydration as this will become relevant in the newly developed transfer function techniques.

Finally, the principles of transfer function analysis were discussed along with EIS and DMA used as examples of well-established transfer function techniques. A method-method matrix of transfer functions was presented with the prioritised, successfully developed transfer function techniques highlighted.

In the subsequent section, the implementation of the novel diagnostic techniques will be discussed.

Chapter 3

Materials and Methods

Due to the nature of this work in developing novel diagnostic techniques, each of the three studies required different methods and equipment. However, the fuel cell materials used are largely similar throughout the studies.

3.1 Localised EIS using a Reference Electrode Array

Reference electrode measurements in PEMFCs are generally made with edge-type or sandwich type reference electrodes.

Edge type reference electrodes require the measurement to be taken at the edge of the MEA on part of the membrane. The reliability of this method is heavily dependent on the alignment of the anode and cathode, as any misalignment of the electrodes will result in voltage and current edge effects [77, 78]. He and Nguyen also reported that the geometry of the measurement location also played a significant role in achieving a reliable reference measurement [79].

Sandwich type reference electrodes require the probe to be inserted between two sheets of membrane before being hot pressed together. However, Büchi and Scherer [80]

reported this method increases the membrane resistance in PEMFCs and affects water management. Li and Pickup also reported this system perturbation for DMFCs [81].

A more recent approach [82-84] to reference electrode measurements in PEMFCs is to make contact with the electrodes through the flow field plates, GDL, and MPL. While this increases the cost and complexity of the system, there is scope to make reliable, localised reference electrode measurements without compromising water management in the membrane or accuracy of measurement.

3.1.1 Reference Electrode Array

Brightman and Hinds [83, 84] developed a 50 cm^2 single cell PEMFC with 3 × 3 reference electrode array to perform transient voltage measurements on start-up and shut-down.

Each reference electrode was connected to the fuel cell cathode via a salt bridge fabricated using Nafion tubing (Perma Pure, NJ, USA) with an outer diameter of 0.84 mm sheathed in a polytetrafluoroethylene (PTFE) sheath with an outer diameter of 1.27 mm. The PTFE sheath allowed for the salt bridge to pass through holes in the end plates, current collector, and cathode flow field plate, with an O-ring seal to allow for the pressurisation of the cathode gas. The Nafion tubing was filled with de-ionised water to ensure hydration and plugged internally with a polyether ether ketone (PEEK) filament of 0.45 mm diameter (Goodfellow Ltd., UK).

The other end of the salt bridge (length approximately 25 cm) was immersed in a glass vessel filled with 0.5 M H_2SO_4 containing a Hydroflex hydrogen reference electrode (Gaskatel GmbH, Germany). The hydrogen reference electrodes were calibrated against a standard hydrogen electrode (SHE) in 0.5 M H_2SO_4 at room temperature before being used in the fuel cell.

A schematic of the Nafion tubing passing through the end plates in order to make direct ionic contact with the cathode is shown in Figure 3.1

The cathode was selected as the electrode of interest due to its relatively higher contribution to the overall cell impedance and greater variation of humidity and water management issues due to the formation of water on the cathode. The reference electrode array provided a means to make cathode-specific localised impedance measurements for the first time.

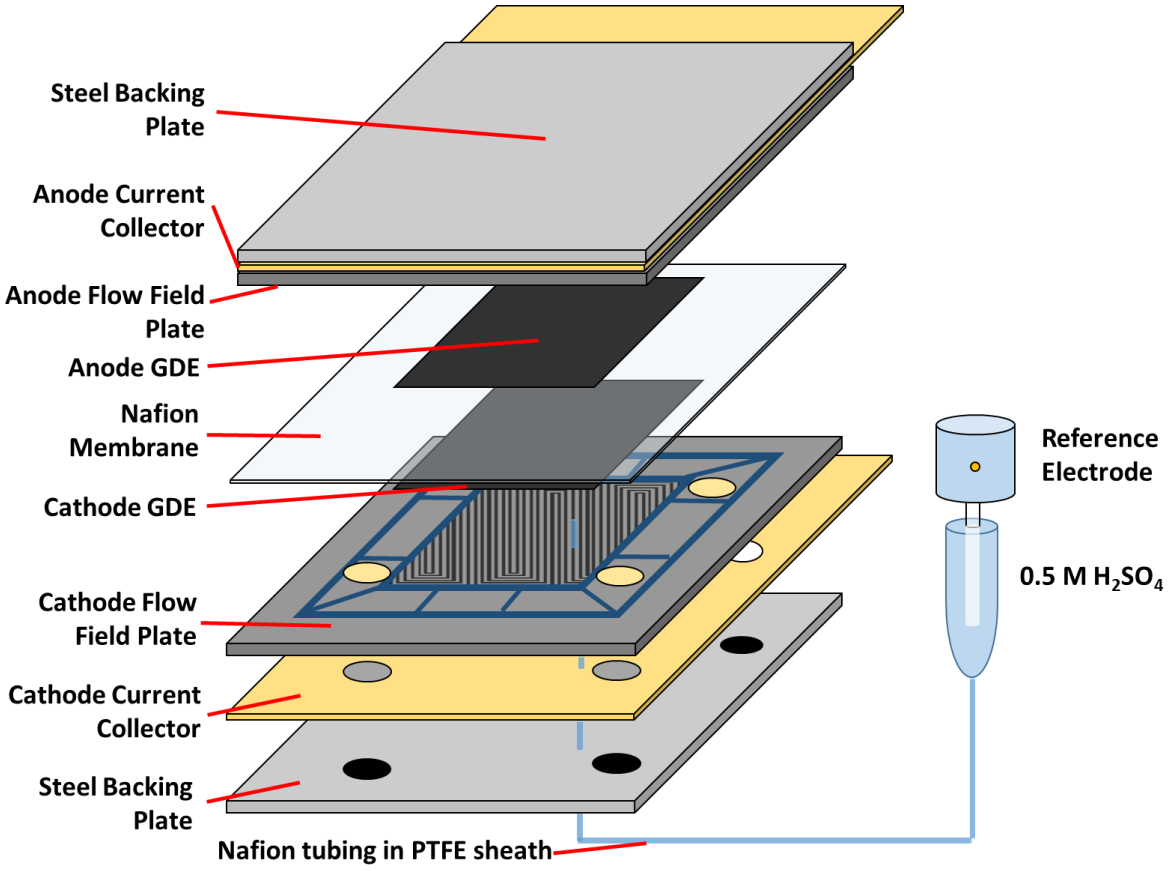

Figure 3.1 - PEMFC developed by Brightman and Hinds [84] with reference electrode array passed through end plates for ionic contact with cathode and electrode-specific measurements.

3.1.2 Membrane Electrode Assembly

A 50 cm^2 MEA was supplied by Johnson Matthey (Johnson Matthey Fuel Cells, UK) and consisted of a Nafion membrane with an anode and cathode platinum loading of 0.07 mg cm^{-2} and 0.4 mg cm^{-2}, respectively.

In order to achieve an ionic pathway through the gas diffusion layer (GDL) and micro-porous layer (MPL), previous implementations of the reference electrode array for dc measurements have used a Nafion solution with propanol to impregnate the GDL and MPL at the point of contact.

However, for EIS measurements, this was found to give rise to impedance artefacts caused by stray capacitances [85, 86]. Therefore, in the work presented, two methods were proposed to overcome the impedance artefacts: Utilisation of a platinum wire with the Nafion tubing in the PTFE sheath, and the drilling of a hole through the MPL and GDL to make direct contact between the catalyst layer and the Nafion tubing.

The latter solution overcame the issue of stray capacitances and to this end, before the GDL was compressed with the membrane and catalyst layer, nine 0.9 mm holes were drilled through the GDL of the cathode in line with each of the contact points of the reference electrodes. The cell was then compressed using a pressurised gas and piston arrangement with a compression pressure of 6 bar_g.

Polarisation curves of an unmodified MEA and of an MEA with holes in the GDL were recorded for comparison. The gases were supplied in a partial counter-flow configuration with the reference electrode array implemented on the cathode. Due to the large area of

the fuel cell and configuration, each current density was held for 300 s to record a representative cell voltage.

The configuration of the nine reference electrode connections relative to the serpentine flow-field on the cathode is shown in Figure 3.2.

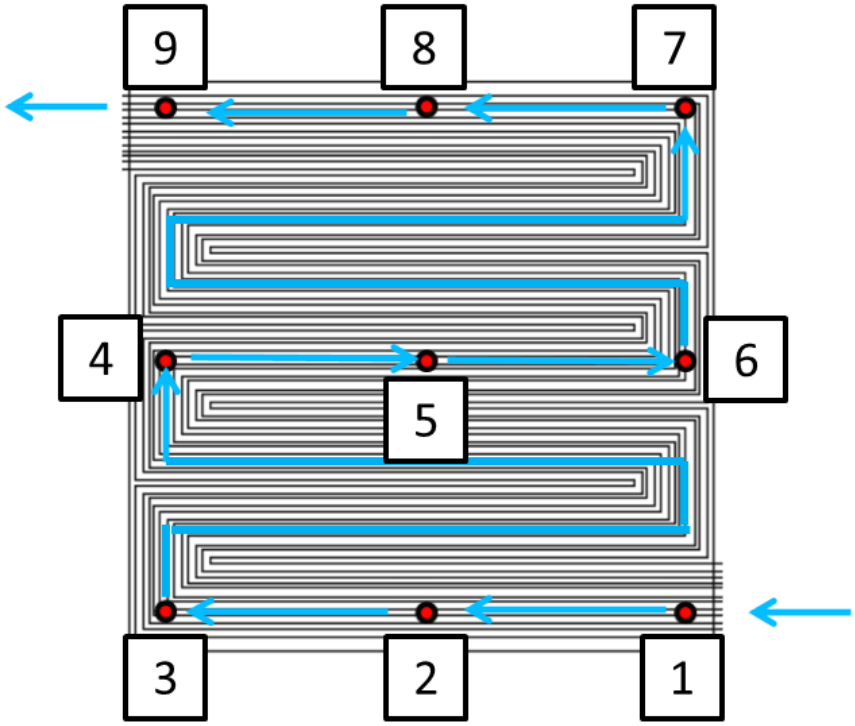

Figure 3.2 - Schematic of the cathode flow-field with the direction of air flow shown in blue and placement of reference electrodes in red. Hydrogen is passed through a similar flow-field on the anode in a partial counter-flow configuration such that the anode gas is counter-flow in the horizontal direction and co-flow in the horizontal direction.

3.1.3 Electrochemical Impedance Spectroscopy

EIS was performed using a LabVIEW-based (National Instruments, USA) multi-channel frequency response analyser developed in house by Meyer *et al.* (UCL-FRA) presented in previous studies [54, 87].

The software, in this case, required a data acquisition (DAQ) device with eleven inputs and one output (USB 6363 Multifunction DAQ, National Instruments, USA). The 11 voltage inputs were for the nine reference electrodes, the overall cell voltage, and the current measured with a current probe (Tektronix A622, RS Components Ltd., UK).

The one output was for the software to deliver a signal to an external load which subsequently controlled and applied the sinusoidal fluctuation to the fuel cell current. A schematic of the frequency response analyser integrated into the reference electrode system is shown in Figure 3.3.

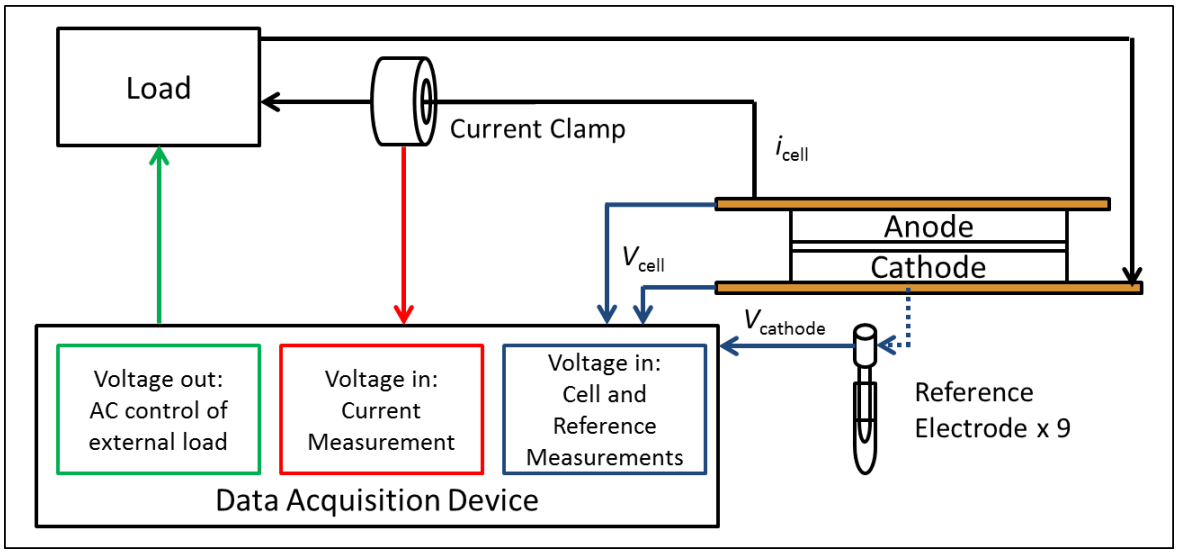

Figure 3.3 – Schematic of frequency response analyser for localised EIS cathode measurements.

3.1.4 Fuel cell testing

All experiments were carried out at 80 °C, 90% RH, and 204 kPag backpressure using a G100 test stand (Greenlight Innovation Europe, Germany). Hydrogen was supplied to the anode and air to the cathode (BOC plc, UK), both at two times stoichiometry, with a minimum flow rate of 20 mL min^{-1} hydrogen and 50 mL min^{-1} air.

3.2 Electro-thermal Impedance Spectroscopy

The intent of the design of experiment for the development of ETIS was to simplify the system as much as possible from a thermal perspective. For this reason, a passive, open-cathode PEMFC was selected for the development of the technique.

3.2.1 Open-Cathode Fuel Cell Design

The PEMFC consisted of two printed circuit board (PCB) current collectors (anode and cathode) which also distributed gases, a membrane electrode assembly (MEA), gaskets and two end-plates. PCBs have been previously used as current collectors for fuel cells [88-90] due to their low cost and weight as well as their design flexibility.

The PCB geometry was 1.6 mm thick and contained a 38 µm layer of copper, which was coated with a proprietary carbon-based ink for corrosion protection. The gaskets used for gas manifolds were made of silicone and were 0.4 mm thick, and those used as seals between the end-plate and current collector were 0.15 mm thick.

A double-serpentine flow-field geometry was used for the anode and a parallel vertical flow-field was used for the cathode. A schematic of the design is shown in Figure 3.4. The 1 mm slits in the cathode flow-field where the GDL is exposed to the atmosphere are referred to as ‘channels’ and the 1 mm wide sections of PCB material between the channels are referred to as ‘lands’.

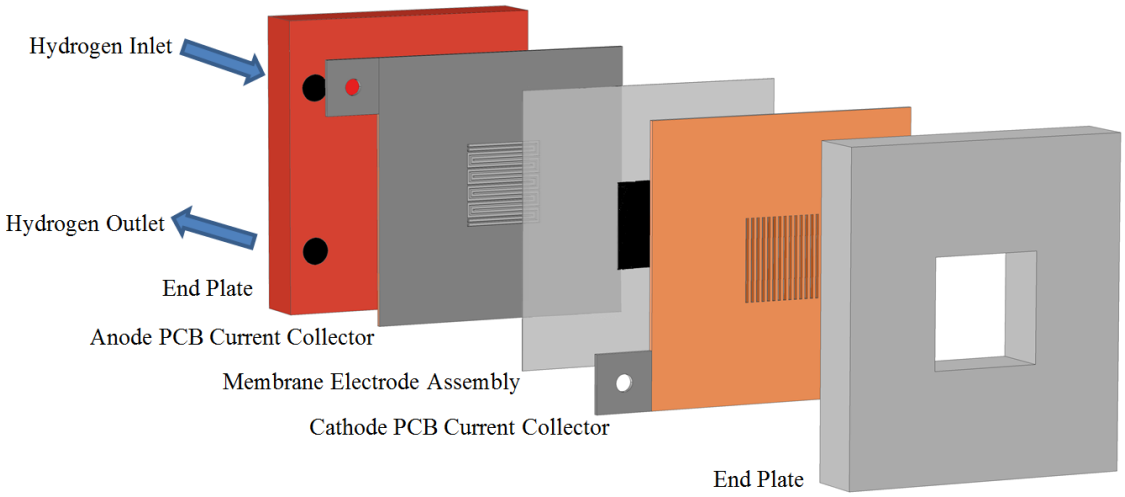

Figure 3.4 - Schematic of the open-cathode PEMFC design. The MEA can be directly viewed through the aperture in the end-plate and the open channels in the cathode current collector.

The cathode end-plates were made from aluminium and contained a 13 cm^2 square open window for direct visualization of the flow-field. The size of this window was larger than the active area of the cell and had a negligible effect on the electrochemical performance of the cell. The aluminium and lands on the cathode side were painted with acrylic black paint in order to increase the emissivity of the material.

A torque of 3.6 Nm was applied to each of the four tie bolts to compress the cell and achieve a similar performance as achieved by Obeisun *et al.* in other studies which have used the same cell design [88, 89, 91, 92].

3.2.2 MEA fabrication

The electrolyte, Nafion 117 (Fuel Cell Store, USA), was pre-treated at 80 °C in 3% H_2O_2 (Sigma Aldrich, UK) to remove all organic impurities and then in 1 M H_2SO_4 (Sigma Aldrich, UK) to sulfonate the electrolyte.

The MEAs were produced in-house using the electrolyte and ELE0237 Johnson Matthey 0.4 mg cm^{-2} platinum electrodes (Johnson Matthey Fuel Cells, UK) with an active area of 9.6 cm^2. The MEAs were pressed (Carver 4122CE, USA) at 170 °C for 4 minutes with an applied pressure of 3100 kPa.

3.2.3 Thermal imaging

Thermal imaging was performed using a 640×512 focal plane array InSb camera (SC5000MB FLIR, UK). The camera was calibrated for the temperature range in question (15 °C - 60 °C) with the images being recorded using commercially available software (ResearchIR, FLIR ATC, Croissy-Beaubourg, France) at 100 frames per second.

ETIS was performed by fixing the location of the camera in relation to the cell and selecting identical pixel groups through the range of frequencies examined. The emissivity of the cathode GDL was calculated to be in excess of 0.95 over the temperature range observed during the experiments and the lands after being painted black were measured to have an emissivity in excess of 0.97.

The aforementioned emissivity values were calculated using the material heating method. This required individually heating the fuel cell components on a hot plate to known temperatures in the fuel cell operating range (15 °C and 50 °C). A thermocouple is then used to measure the surface temperature and input into the thermal imaging software to compare the apparent temperature to the real value. This effectively applies the emissivity correction to specific areas based on the surfaces of different materials.

Thermal images were post-processed using commercially available software to obtain temporal temperature data and lock-in images (Altair LI, FLIR ATC, Croissy-Beaubourg, France).

3.2.4 Fuel cell testing

A fuel cell test station (840 Advanced Fuel Cell Test System, Scribner Associates, USA) was used to supply dry hydrogen gas to the fuel cell anode. Hydrogen (99.995% purity, BOC plc, UK) was supplied at ambient temperature at a rate of 100 mL min^{-1}. The cathode was open to the atmosphere. The cell was not heated to reduce the noise associated with heating the cell through conventional PID-control.

An IviumStat potentiostat (Alvatek, UK) was used to apply single-frequency current perturbations with 3 mA cm^{-2} amplitude between 100 µHz and 1 Hz to the fuel cell and measure the voltage response.

The current was measured with a current clamp (Tektronix A622, RS Components Ltd., UK) and recorded in a data acquisition unit (USB 6363 Multifunction DAQ, National

Instruments, USA) which amplified the signal to an equivalent stimulus signal within the specifications of the thermal imaging camera (0 – 10 V). A drawing of this experimental set-up is given in Figure 3.5.

The output voltage from the DAQ board to the thermal imaging camera was also recorded by the DAQ board in order to ensure there was no phase-shift difference between the original current signal and the amplified signal for input into the camera.

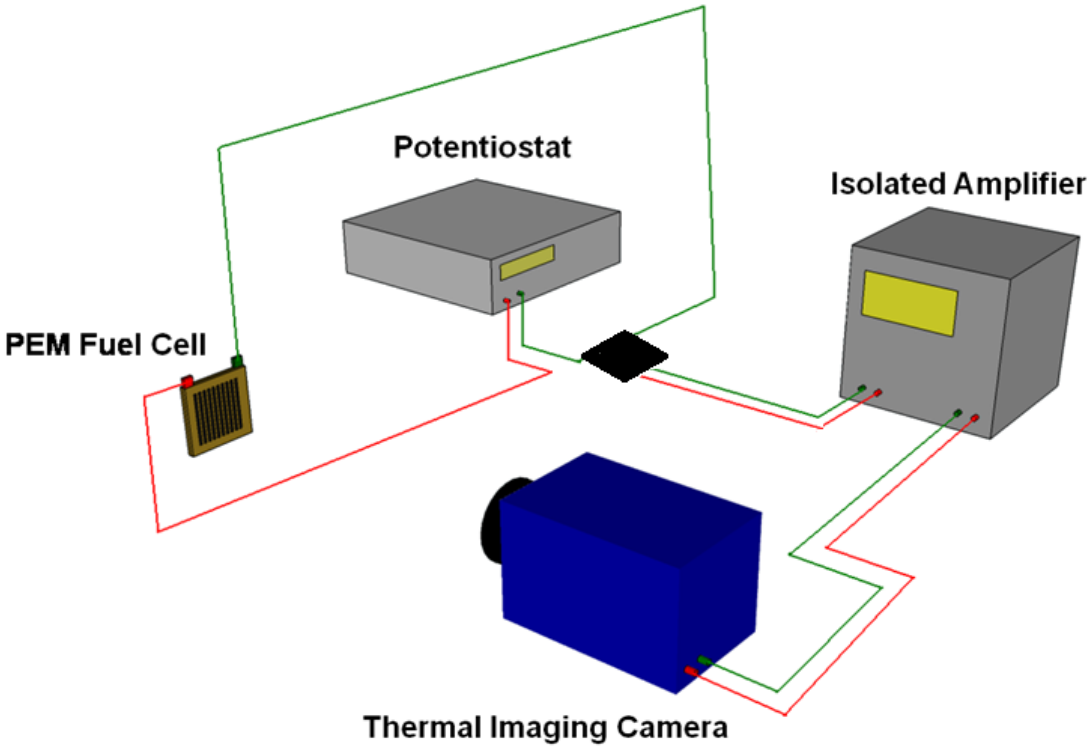

Figure 3.5 – ETIS experimental set-up in order to acquire current perturbation signal from the fuel cell.

3.3 Electrochemical Pressure Impedance Spectroscopy

The greatest challenge in the design of experiment for the development of EPIS was the method by which the cathode pressure could be rapidly, reliably and periodically perturbed. Initially, the pressure was to be modulated with an ASCO 202 solenoid valve (Air Engineering, UK), which can open and close at a rate of 400 Hz. However, after tuning the solenoid, it was found to be inadequate to output a periodic sinusoidal pressure perturbation above 1 Hz.

An alternative way to perturb the cathode oxidant pressure was to use a loudspeaker. A loudspeaker can produce regular sinusoidal pressure perturbations at different frequencies [93]. In a closed cathode system, this provided an elegant solution to a complex control problem.

3.3.1 Pressure modulation

For fixed cathode pressure measurements, a manual backpressure valve (Scribner Associates, Alvatek, UK) was used to apply pressure between 0 and 62 kPa_g.

For dynamic modulation (EPIS) measurements, the cathode backpressure was modulated using a loudspeaker (Visaton WS 17 E, RS Components Ltd., UK). The housing for the speaker was built in-house using Perspex such that the system would remain air-tight. The experimental system used to apply the pressure modulation to the fuel cell is illustrated in Figure 3.6.

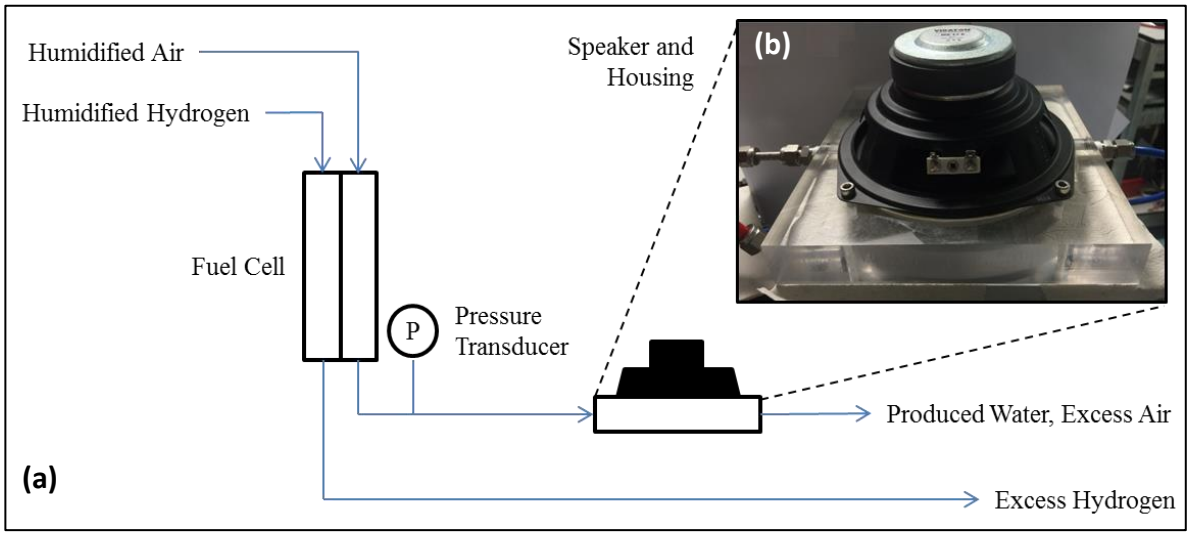

Figure 3.6 – Schematic diagram of the experimental rig (a) and inset photo of speaker and housing (b). Silicone rubber was applied between the speaker and housing to ensure a gas-tight seal. Humidified hydrogen and air were controlled using a Scribner fuel cell test system.

The speaker housing was attached ~15 cm linearly downstream of the fuel cell such that the absolute pressure was closer to the speaker atmospheric operating range while still close enough to the fuel cell to influence the cathode backpressure. The cathode backpressure was modulated by applying a sinusoidal current to the speaker using an IviumStat potentiostat (Alvatek, UK). The resultant amplitude of the pressure 'front' at the fuel cell was 60 Pa for the investigated frequency range.

3.3.2 Rig and fuel cell design

A fuel cell test station (Scribner Associates, USA) was used to supply heated and humidified hydrogen gas to the fuel cell anode and air to the cathode. Hydrogen (99.995% purity, BOC plc, UK) was fed to the anode and zero grade air (21% O_2, BOC plc, UK) to the cathode at 60 °C and either 70% RH or dry. Flow rates of gases were fixed at 100 mL min^{-1} and 250 mL min^{-1} to the anode and cathode, respectively unless stated otherwise.

A commercially available fuel cell (Scribner, Alvatek, UK) was used with an active area of 5 cm^2 and a serpentine flow-field machined in resin-impregnated graphite on both anode and cathode. The channels and lands were both 1 mm wide. Compression of the cell was controlled by applying 2 Nm torque to each of the 8 bolts of the cell.

An IviumStat potentiostat (Alvatek, UK) was used to apply a constant current to the fuel cell system while measuring the voltage. The cell was operated galvanostatically to control the stoichiometry of the reaction.

The cathode backpressure relative to atmosphere was measured directly downstream of the fuel cell with a pressure transducer (Honeywell 162PC01D, RS Components Ltd., UK). The principle of operation of a differential pressure transducer is based on transforming an excitation signal into a measured signal based on the physical distortion of a diaphragm inserted between the two pressures in question. The diaphragm is made of a piezoelectric material which produces a voltage linearly with strain. The pressure transducer was calibrated using two pressures: Atmospheric and a column of water of known height.

The pressure and voltage were both recorded at 2000 Hz using a data acquisition unit (USB 6363 Multifunction DAQ, National Instruments, USA) and customised LabVIEW software.

3.3.3 MEA fabrication

MEAs were produced in-house using HP Nafion electrolyte (Nafion Store Europe, Germany) and Johnson Matthey 0237 platinum electrodes (Johnson Matthey Fuel Cells, UK) with an active area of 5 cm^2. The Pt loading on both anode and cathode was 0.4 mg cm^{-2}. It was found that hot-pressing the HP Nafion resulted in hydrogen crossover and poor cell performance, hence the MEAs were pressed together by compression in the fuel cell.

Chapter 4

Localised Electrochemical Impedance Spectroscopy Using a Novel Reference Electrode Array

As discussed in the literature review, EIS is the most widely applied transfer function diagnostic technique when considering PEMFCs. However, the majority of these measurements are made as a global measurement based on a 2-electrode (anode - cathode) measurement. This makes it difficult to deconvolute the individual contributions of anode and cathode.

Moreover, the total cell impedance may not represent localised effects well due to differences in gas concentration and humidification, which can vary significantly over a large MEA surface area. In this chapter, localised EIS measurements of a cathode PEMFC are made using a reference electrode array and the evolution of the EIS high-frequency intercept with time is observed during start-up.

4.1 Introduction

4.1.1 Localised EIS of a PEMFC

Many complex processes occur in PEMFCs [6] which are further complicated by spatial variation due to changing conditions such as humidity and concentration as gases flow through the system. Several methods have been proposed for measuring local currents in galvanic cells, such as incorporating mini-electrodes and loop Hall effect sensors [94-98]. Cleghorn *et al.* pioneered the most widely used design to measure local current densities: the segmented current collector [99]. Using a segmented printed circuit board (PCB) current collector design, this approach allowed the effects of varying humidity and stoichiometric flow rate of air to be determined spatially across the extent of a cell.

The segmented flow field and current collector approach has been applied in further studies to measure the local effects on current density when altering cell temperature, clamping pressure, polarisation, and introducing trace amounts of poisoning gases into the feed streams [52, 100-111]. A crude measure of local current does not allow the various losses that constitute performance to be determined. However, electrochemical impedance spectroscopy (EIS) as previously described, can differentiate between various performance losses [23].

Localised impedance measurements have been made in previous studies using the segmented flow-field configurations where one or both of the flow-fields were segmented. Although Cleghorn *et al*. [99] recorded the spatial effects of membrane hydration at steady state by measuring the high frequency (HF) resistance, Brett *et al.*

presented the first work of localised impedance spectroscopy on a PEMFC [110]. Using ten segmented measurements with independent loads, they demonstrated increased impedance associated with mass transfer losses down the flow field channel as reactants are consumed. Schneider *et al.* [111] investigated the effects of humidity and stoichiometry of the feed gas on localised impedance; demonstrating that the overall cell impedance spectrum can be misleading. Hakenjos and Hebling [112] then coupled impedance data with thermal performance by developing a diagnostic system which could perform thermal imaging through an IR transparent flow field simultaneously with EIS on 16 individual segments.

A number of studies demonstrated the spatial variations of a ten segment single cell PEMFC with loop Hall effect sensors to measure local currents under varying conditions, such as CO poisoning of the anode gas [105, 106, 113], acetonitrile [103] and acetylene poisoning [104] of the cathode gas, as well as studies varying the flow-field geometry [107] and back pressure [108]. These studies demonstrated that the poisoning of the anode was not uniform and there was a general deterioration of the charge transfer resistance from the inlet down the channel with time. Bender *et al.* also demonstrated the spatial dependence of resistance with polarisation.

The critical commonality in all the aforementioned studies is that the designs of the flow-fields have been altered to perform local measurements and EIS was performed in a two-electrode configuration, meaning that the cathode performance cannot be unequivocally separated from that of the anode.

4.1.2 Reference electrodes for *in-situ* testing in PEMFCs

Reference electrode placement in PEMFCs is difficult due to geometrical constraints. Conventional reference electrodes are either internal (sandwich) or external (edge) type. The internal type is fabricated by placing a thin reference electrode between two membranes and hot pressing. This has effects on both the ionic and water transport across the membrane [81].

The external type reference electrodes are connected to the edge of the membrane with a salt bridge. This type of reference electrode suffers from potential drops due to the distance to the reference electrode and edge effects caused by misalignment between the electrodes [77, 79]. Several computational studies have been conducted applying EIS to a three-electrode configuration [114-118] in order to determine the impedance through the cathode catalyst layer. Cruz-Manzo *et al.* [114-116] showed agreement between computational models and experimental results using an edge-type reference electrode, but were unable to provide spatially-resolved impedance spectra of a single cell.

Piela *et al.* [82] and Hinds and Brightman [83, 84] developed reference electrode designs which overcome the limitations of sandwich and edge-type reference electrodes by approaching the electrode through the end-plates, current collectors, and flow-fields. This is achieved by drilling holes in each layer and assuring gas-sealing with O-rings. Hinds and Brightman [83] applied the technique to show transient voltages during start-up and shut-down which led to performance degradation.

Although this configuration adds significant complexity to the design of the fuel cell system, it allows for multiple reference electrode measurements to be made with local resolution of potential, and most importantly, the measurement is free from an Ohmic potential drop in the membrane.

In this chapter, localised EIS is applied using a reference electrode array to determine, for the first time, spatially-resolved impedance spectra on the cathode of a PEMFC. Localised high-frequency intercepts were also monitored upon polarisation of the cell and during transient operation to give insight into membrane hydration dynamics on start-up.

4.2 Results and Discussion

4.2.1 Impedance artefacts

Initially, it was attempted to make impedance measurements using the same procedure adopted by Brightman and Hinds [83, 84] by making electrical contact with the catalyst layer through the GDL and MPL using Nafion impregnated in these layers.

However, the use of this method gave rise to impedance artefacts, as shown in Figure 4.1. These artefacts are characterised by the crossing of the impedance arc into the second quadrant of the Nyquist plot (a negative real number contribution). This type of artefact was previously observed by Balabajew *et al.* [85] and attributed to stray capacitances present in high-frequency measurements.

In order to establish whether these stray capacitances originated in the length of Nafion tubing or in the short distance between the top of the GDL and the catalyst layer, two solutions were attempted.

The inclusion of a platinum wire with the Nafion tubing is a solution suggested by Mansfeld *et al.* [86]; this is meant to overcome the resistance and capacitance at the tip of a reference electrode by running the platinum wire in parallel with the reference electrode. In this schematic, it is thought the dc potential is measured through the reference electrode and the ac potential through the platinum wire.

In order to achieve better electrical contact through the GDL and MPL, holes were drilled through these layers such that the Nafion salt bridge could make direct contact with the catalyst layer. The results of these alterations are shown in Figure 4.1.

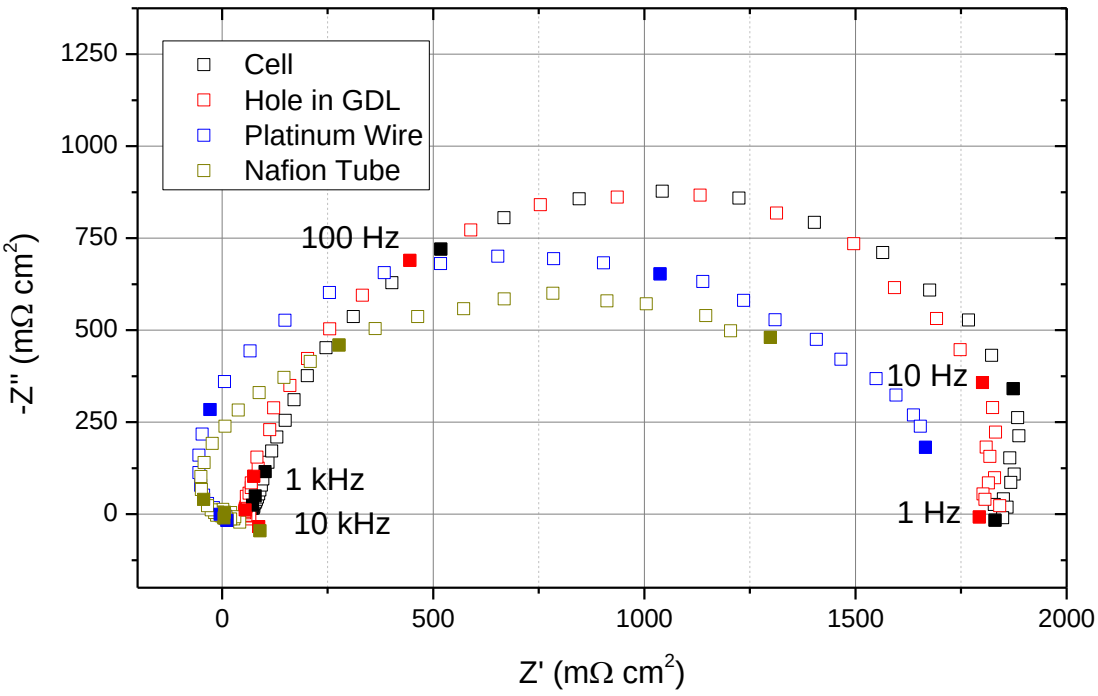

Figure 4.1 – EIS of spectra of overall cell and use of reference electrode with Nafion salt bridge, platinum wire, and a hole through the GDL and MPL. The former two measurements were made with Nafion impregnation through the GDL and MPL. EIS was performed between 10 kHz and 1 Hz at OCV with a current perturbation of 20 mA.

From Figure 4.1, it is clear that the impedance artefact is still present when using the platinum wire instead of the Nafion tubing, indicative that the Nafion tubing is not the cause of the feature. However, when considering the holes drilled through the GDL and MPL, the artefact is no longer present and the impedance spectrum much more closely resembles the expected arc behaviour, matching the cell impedance arc closely. However, in order to validate this method as a diagnostic technique, the effect of this major alteration on the fuel cell performance must be evaluated.

4.2.2 Effect of holes through GDL on fuel cell performance

In order to measure the effect of drilling through the GDL on overall cell performance, polarisation curves of the new configuration, with altered GDL and unaltered GDL were compared.

From Figure 4.2 it can be seen that there is little difference in the performance of the two MEAs at low current densities. There is a deviation at high current densities, above 1 A cm^{-2}, as the limiting current density of the MEA with holes in the GDL is lower than that of the unaltered MEA. This is due to the increased mass transport limitations caused by the removal of sections of the GDL. Water removal from the catalyst layer is less effective and thus oxygen diffusion through the GDL is impeded. This affects the validity of the EIS spectra at higher current densities, as they are less representative of the unaltered MEA but provides accurate representation below ~800 mA cm^{-2}.

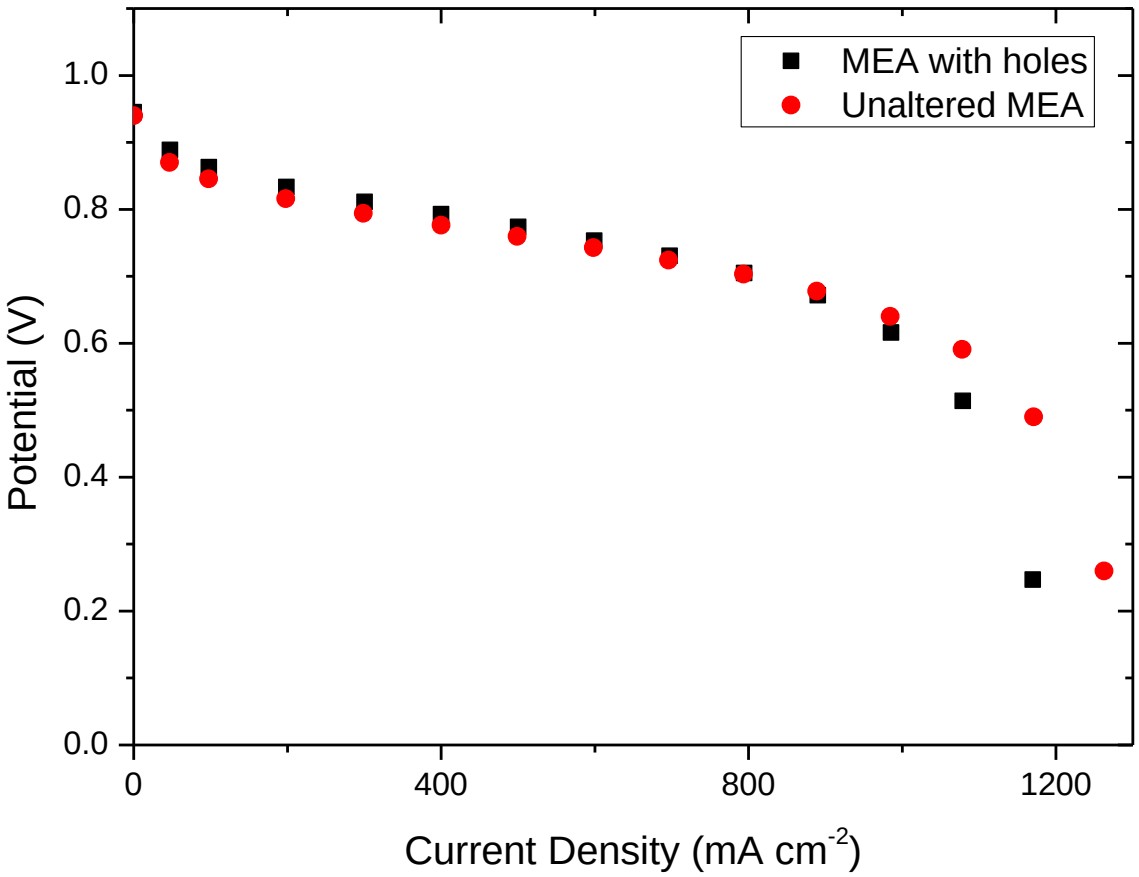

Figure 4.2 - Polarisation curves of unaltered MEA and MEA with nine holes in the cathode GDL at reference electrode points. Humidified hydrogen and air (90% RH) were supplied at two times stoichiometry, 80 °C and 204 kPag back pressure. The potential was averaged over the last minute of a five-minute galvanostatic hold for each point.

4.2.3 Localised Impedance Spectra of a PEMFC Cathode

The calibration of the reference electrodes required the immersion of all nine reference electrodes in 0.5 M H_2SO_4 measured against a standard hydrogen electrode (SHE) at room temperature. The potentials of all nine reference electrodes were within 3 mV of the SHE during calibration.

EIS was performed simultaneously on all nine reference electrodes between 10 kHz and 0.1 Hz at five different current densities to demonstrate the various impedances in different polarisation regions. The current density perturbation had a peak-to-peak amplitude of 30 mA cm^{-2}, except below 400 mA cm^{-2}, where the amplitude was 20 mA cm^{-2} peak to peak.

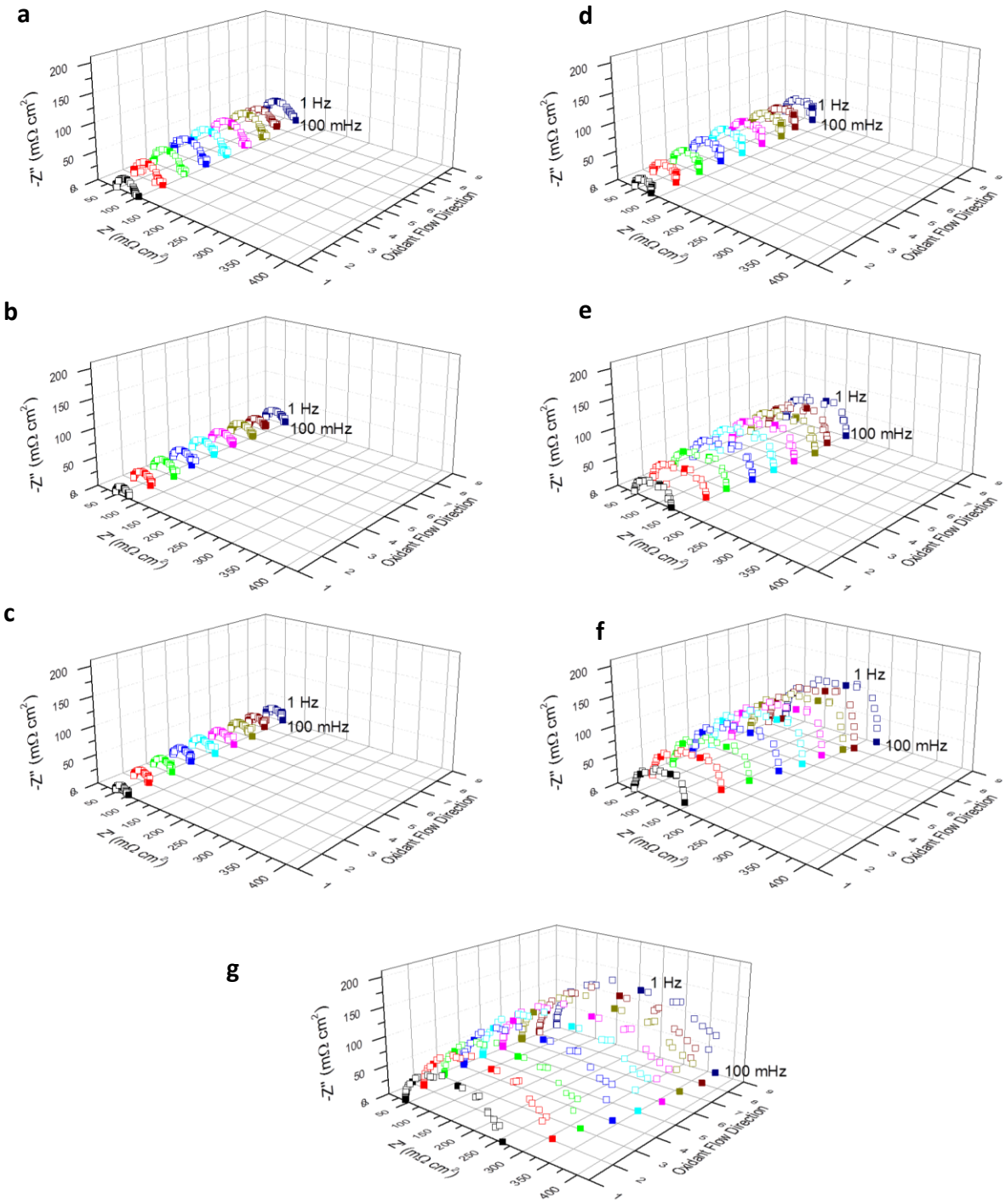

Figure 4.3 - Impedance spectra from 10 kHz to 100 mHz at OCV (a), 100 (b), 200 (c), 400 (d), 500 (e), 600 (f), and 1000 (g) mA cm^{-2}. EIS was performed galvanostatically with an amplitude of 20 mA cm^{-2} when polarised below 400 mA cm^{-2}, 30 mA cm^{-2} above this value.

Humidified hydrogen and air (90% RH) were supplied at two times stoichiometry, 80 °C and 204 kPag back pressure.

From Figure 4.3, it can be observed that the LF impedance, represented by the intercept with the real plane at low frequencies, initially decreased with increasing current density for each reference electrode location. Above 400 mA cm^{-2} (Figure 4.3e-g), the impedance of each segment increases due to the onset of mass-transport limitation.

The LF resistance is more clearly plotted as a function of position and current density in Figure 4.4. Below 600 mA cm^{-2} there is little variation in the resistance; approximately 10 mΩ cm^{-2} across the channel at 400 mA cm^{-2}. This is indicative of there being sufficient oxidant reaching the catalyst at all the locations down the channel.

Above this current density, as more oxidant is consumed and water is generated, the low-frequency impedance increases down the flow-field. These results are consistent with the work of Brett *et al.* [110] who reported similar trends for a single-channel cell. At a current density of 1000 mA cm^{-2}, the low-frequency impedance at the first reference electrode location (closest to the cathode inlet) is approximately 100 mΩ cm^2, or ~25% lower than the final reference electrode location near the outlet.

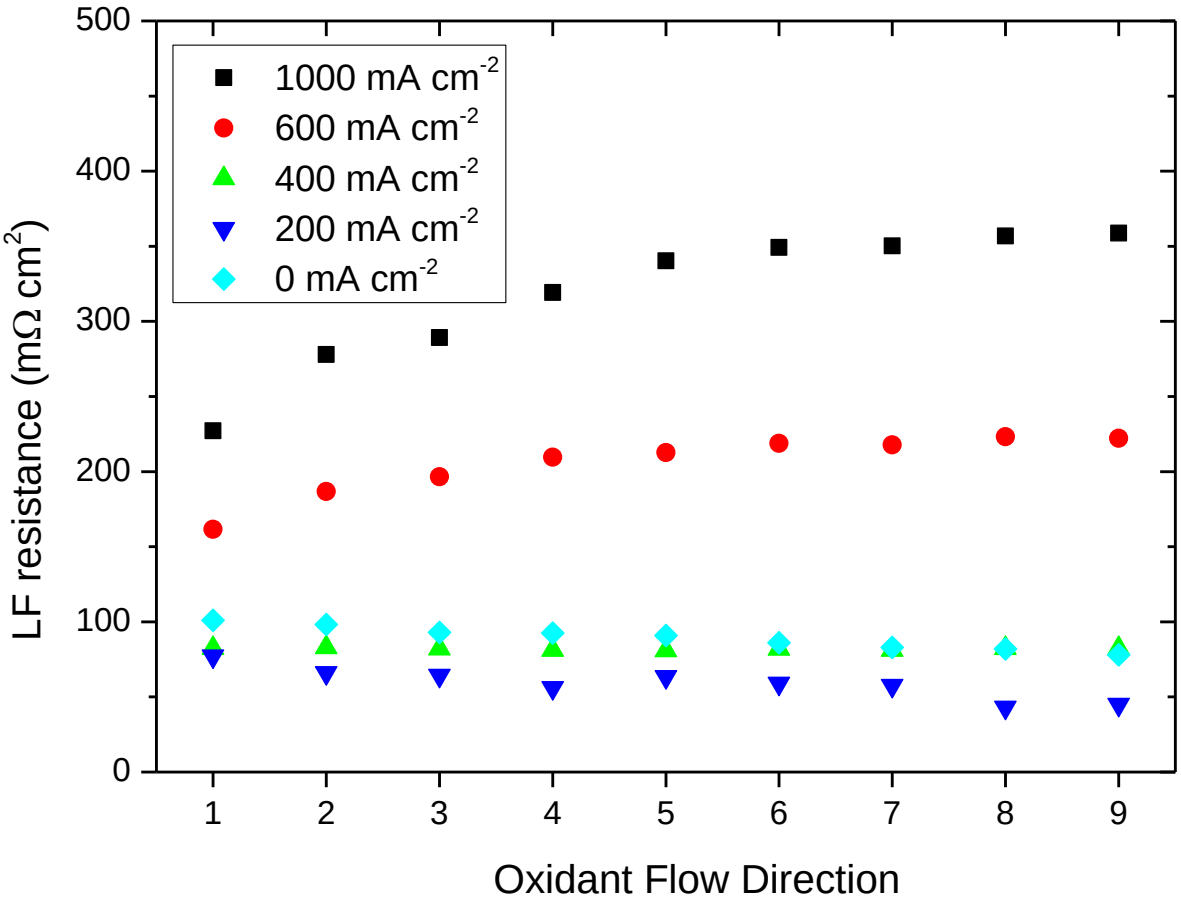

Figure 4.4 – Low-frequency intercept (1 mHz) impedance from nine reference electrodes on the cathode at 1000, 600, 400, 200, and 0 mA cm^{-2}. EIS was performed galvanostatically with an amplitude of 30 mA cm^{-2} at two times stoichiometry.

The high-frequency impedance behaviour in Figure 4.3 can be more clearly interpreted in Figure 4.5. For all polarisations, the high-frequency impedance (intercept with the real axis) is greatest at the oxidant inlet and decreases down the flow-field. The high-frequency intercepts do not vary significantly beyond the fourth reference electrode. This indicates that the membrane is not fully hydrated at the entrance to the cell and requires an

'entrance length' of the channel in order for the gas to reach equilibrium with the product water generated in the cell. This difference is a function of cell temperature, fuel cell current (water production rate), gas humidification and temperature [119, 120]. With increasing current densities, the high-frequency intercept decreases as there is better hydration due to water formation and thus lower Ohmic resistances and decreasing of the 'entrance length'.

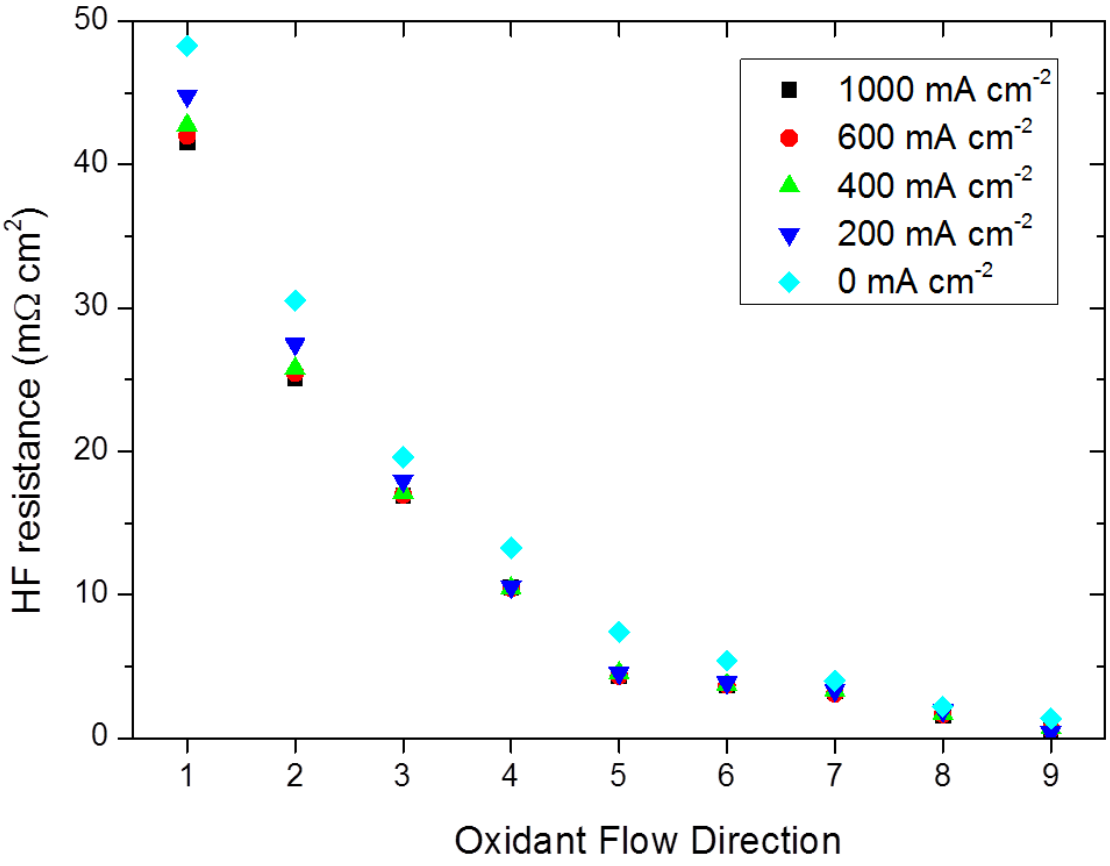

Figure 4.5 - High-frequency impedance data at 1 kHz at OCV, 200, 400, 600, and 1000 mA cm^{-2} for all nine reference electrode locations. EIS was performed galvanostatically with an amplitude of 30 mA cm^{-2} at two times stoichiometry in a partial counter-flow configuration.

4.2.4 High-frequency resistance transients on start-up

The HF resistance data presented in Figure 4.5 are representative of a system already at steady state. Although there is an underlying assumption in transfer function analysis requiring linearity in a system, it is possible at very high frequencies to assume pseudo-linearity. This is due to the fact that the frequency of the perturbation is much faster than the rate of change of the system.

Therefore the high-frequency transients on start-up of the PEMFC were investigated, in order to observe the hydration behaviour of the membrane as water is produced in the PEMFC.

The high-frequency resistance was observed relative to each respective initial high-frequency intercept value. An impedance measurement at 1 kHz was measured every 0.2 s and aggregated after making a step change from OCV to 500 mA cm^{-2}. The change in high-frequency resistance is shown in Figure 4.6.

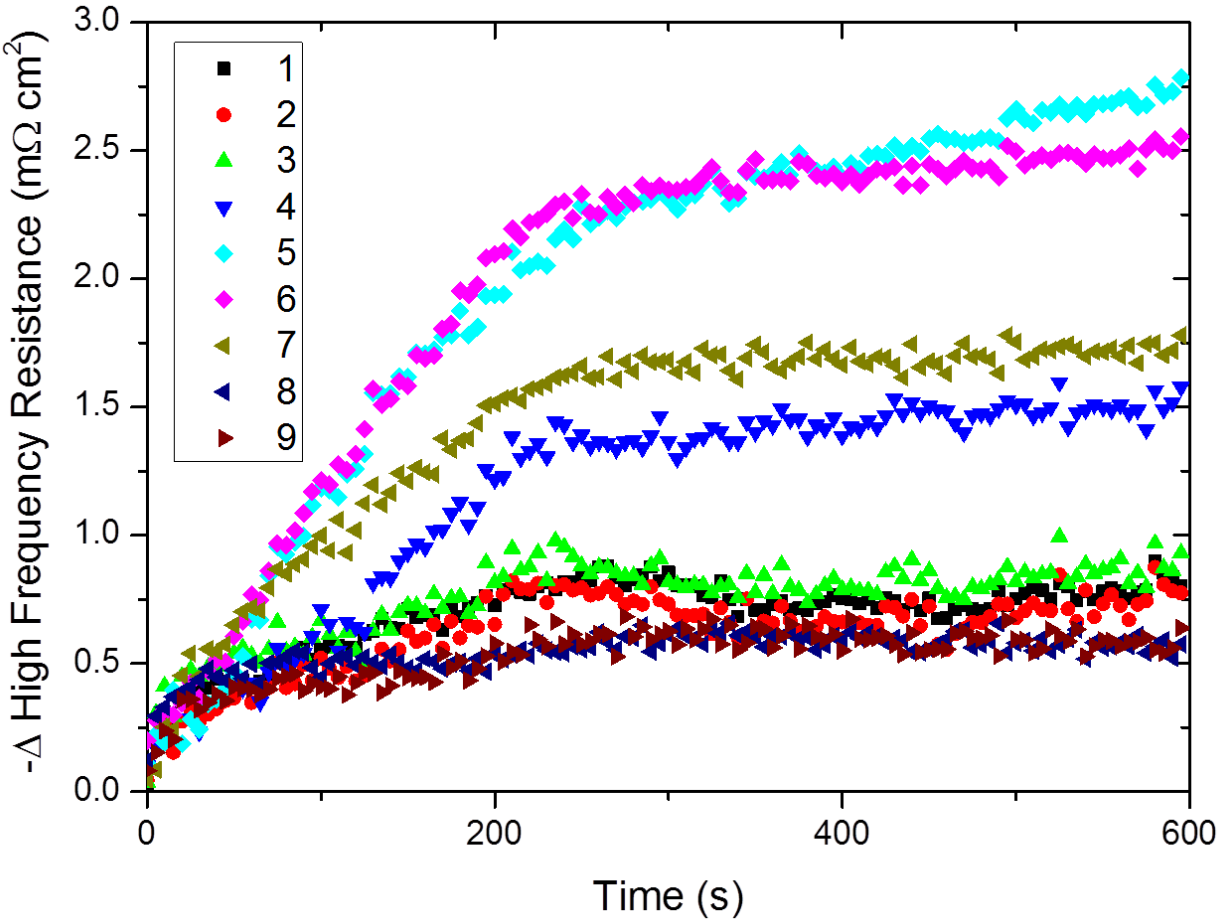

Figure 4.6 - Negative difference between transient data and starting high-frequency intercept for each respective reference electrode following a step change from OCV to 500 mA cm^{-2}. EIS was performed galvanostatically at 1 kHz every 0.2 seconds and aggregated for 10 second intervals with an amplitude of 30 mA cm^{-2}.

From Figure 4.6, three distinctive regions of change can be identified. Within the first 10 s, the HF resistance at each reference electrode location decreases by approximately 0.4 mΩ cm^2. This is in agreement with the findings of Lai *et al.* [121] who reported a rapid membrane swelling step within the first 10 s of applying a current step using an array of

displacement sensors. The membrane swelling then continued with a slower ramp up to steady state, which was achieved after ~250 s, using a Nafion-212 membrane, again in agreement with the results shown.

In further agreement with that study, the high-frequency resistance continues to decrease up to ~250 s, where a steady high-frequency resistance is observed at most of the reference electrode locations. Between 10 s and 250 s, the high-frequency resistance decreases at a rate of approximately 0.008 $m\Omega\ cm^2\ s^{-1}$ in the centre of the MEA as opposed to 0.001 $m\Omega\ cm^2\ s^{-1}$ near the cathode exit.

The decrease in high-frequency resistance at several time stamps relative to position in the flow-field is shown in Figure 4.7. The data in Figure 4.7 (a) demonstrate the similar decrease in low-frequency resistance across the MEA in the first 20 s, before areas towards the middle of the flow-field improve more drastically relative to the edges of the fuel cell. Inferring from the results of Lai *et al.* [121], this may be due to increased current densities in the centre of the MEA, thus producing more water and improving membrane hydration locally.

This also demonstrates that although the fuel cell is capable of instantly outputting the current, the fuel cell will not have reached equilibrium, optimal hydration, and indeed efficiency in the same short period of time.

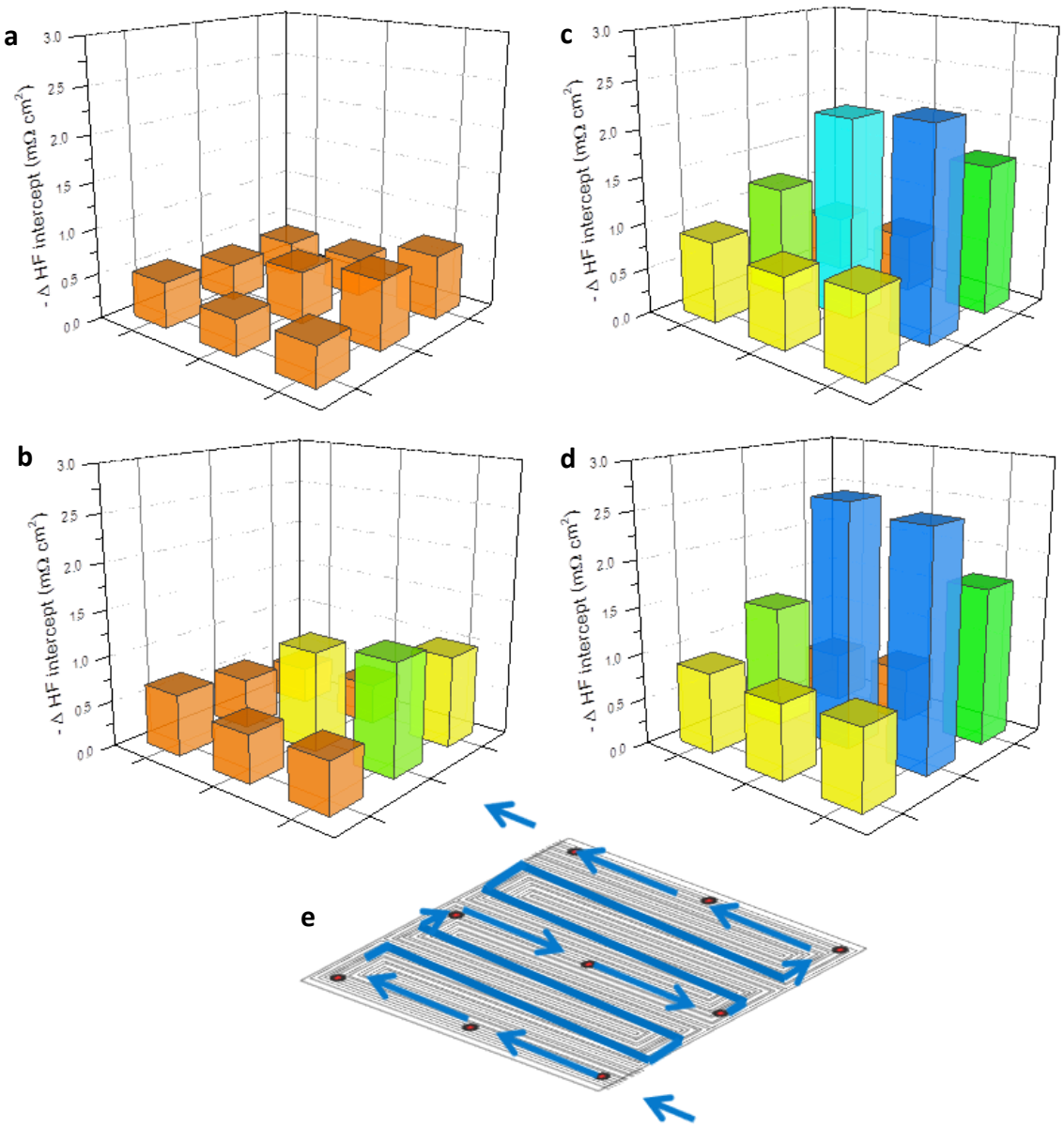

Figure 4.7 - Negative difference in high frequency intercept at each reference electrode location after 20 (a), 100 (b), 200 (c), and 600 (d) seconds, following step-change from OCV to 500 mA cm^{-2}. The direction of air flow relative to the flow-field and the reference electrode is also shown (e). EIS was performed galvanostatically at 1 kHz every 0.2 s with an amplitude of 30 mA cm^{-2}. Humidified hydrogen and air (90% RH) were supplied at two times stoichiometry, 80 °C and 204 kPag back pressure.

4.3 Summary

Localised electrochemical impedance measurements of a polymer electrolyte membrane fuel cell were successfully demonstrated as a diagnostic tool, using a reference electrode array to give cathode-specific measurements as a function of positon on the cathode and cathode polarisation.

The results demonstrate the vast variation in localised high-frequency and low-frequency impedance on the cathode due to changing humidity and gas composition conditions along the channel can result in LF resistance differences across a cathode flow field in excess of 25%.

In addition, the HFR was measured continuously for 10 minutes following a step change from OCV to 500 mA cm^{-2}. The results are in close agreement with previous membrane hydration dynamics studies, demonstrating three distinct regions of Nafion membrane hydration upon polarisation of the fuel cell, with steady state being reached around 250 s after the current is changed.

Chapter 5

Electro-thermal Impedance Spectroscopy as a diagnostic tool for PEMFCs

Having investigated a well-established transfer function, EIS, in a novel way, fuel cell properties other than purely electrical were investigated using a similar approach. Due to the high sensitivity of fuel cell performance and degradation to temperature and the increasing availability of high-resolution IR cameras, Electro-thermal Impedance Spectroscopy (ETIS) was developed as a novel diagnostic tool for PEMFCs. The technique was used to identify common fault mechanisms in PEMFCs such as pinhole formation.

5.1 Introduction

In this introduction, open cathode PEMFC development presented before discussion of ETIS applied to electrochemical devices is presented alongside a related diagnostic technique, lock-in thermography, before introducing pinhole formation, a thermally-relevant PEMFC degradation mechanism.

5.1.1 Air-breathing Open-Cathode PEMFCs

Air-breathing open-cathode PEMFCs have the advantage of requiring little balance of plant as they do not require active convection of air to the cathode. The cathode in these devices is exposed to the atmosphere and oxygen is supplied via natural convection of air [123, 124]. However, they are generally outperformed by their forced-convection counterparts due to the fact that the only mechanism for water removal is evaporation, presenting mass transport limitations at lower current densities.

Printed Circuit Board (PCB) fuel cells are based on using standard materials and methods from the PCB industry to lower the cost of manufacturing fuel cells [125, 126]. These designs are largely made up of a FR-4, a composite material composed of woven fiberglass. This sturdy material can be layered and machined, ideal for construction of BPPs. The current collectors are made of thin (typically 35 µm) layers of copper. Due to the acidic environment in a fuel cell, coupled with potential and temperature changes, the copper is passivated to prevent degradation.

Obeisun *et al.* applied diagnostic techniques to an open-cathode PCB fuel cell design [88, 89, 91]. This design was presented in Section 3.2.1 and applied to the study presented in this chapter.

5.1.2 Electro-thermal Impedance Spectroscopy

ETIS is a technique that applies transfer function analysis, in this instance, a small current (or voltage) perturbation is linked to modulation of heat generation, and consequently the measured temperature. The relative amplitude and phase shift between the periodic current stimulus and the temperature response are frequency dependent and can yield information on the electro-thermal properties of electrochemical devices [127-129].

For example, Schmidt *et al.* [127] applied the technique to a Li-ion pouch cell by measuring the surface temperature at a single point with a thermocouple. They demonstrated that the relative amplitude of the thermal response to the current perturbation is analogous to the 'thermal impedance' of the system; a higher thermal impedance through a material results in a lower temperature at the surface of the material. The phase shift between the perturbation and response is analogous to 'thermal capacitance'; the finite thermal diffusivity of a material means that there is a time lag between perturbation and response.

They were able to determine the thermal conductivity of the bulk pouch material based on low-frequency data. However, current perturbations above 1 mHz produced thermal

responses too noisy to produce a significant result; hence this was a relatively slow diagnostic technique.

Fleckenstein *et al.* [130] developed an ETIS model of a cylindrical lithium ion battery and were able to determine the thermal capacitance and thermal conductivity of the interior 'jelly roll' to within 5% and 12%, respectively.

The application of ETIS to batteries is notably limited due to the long time required for the heat to travel from the source of generation, through a thermal diffusive length, to the surface of the object. However, lock-in thermography, a related technique, has been more widely adopted for studies in electrochemical devices and combines IR thermal imaging with single frequency temperature perturbation/measurement.

5.1.3 Lock-in thermography

Lock-in thermography is an established technique that typically uses a thermal stimulus (e.g. a heat gun or IR lamp) imposed on a sample, with the resultant temperature modulation measured to give spatially resolved information about heat transfer in a system (identification of cracks in components, for example) [50, 131]. Reflection artefacts and variations in emissivity are avoided due to periodic, not absolute, values determining the measurement, thereby improving image fidelity.

While heat is often used as the stimulus, other forms of modulation stimulus can be used that result in heat generation (e.g. mechanical stress, ultra-sound, electrical current) [50].

Robinson *et al.* [132] applied lock-in thermography to a Li-ion pouch cell with a periodic current stimulus, highlighting the ability of the technique to identify sub-surface defects such as gas pockets formed during cell ageing.

The technique has also been applied to silicon materials for solar applications to identify areas containing recombination-active grain boundaries [133], in photovoltaic modules to determine shunt values [134, 135], and in semiconductors to identify cracks [136].

The power and effectiveness of lock-in thermography is governed by the ability to interpret the images. This necessitates appreciation of the factors that lead to phase and amplitude shifts from stimulus to response. The *a priori* knowledge of the physical structure and materials of the device and measured selection of the modulation frequency can yield significant results. Where the internal structure of devices can be determined using techniques such as X-ray computed tomography, the application of ETIS can provide insight into the selection of modulation frequency and interpretation of images [137].

5.1.4 Accelerated stress tests and pinhole formation

Diagnostic techniques such as ETIS and lock-in thermography are intended to measure the performance of electrochemical devices over time. A major hindrance to the uptake of PEMFCs is their durability and diagnostic techniques are critical to identifying degradation issues when they occur.

The US Department of Energy has set a goal of less than 5% power degradation within a fuel cell lifetime of 5000 operational hours for cars [7, 138] and 40,000 hours for stationary applications [139]. The membrane electrode assembly (MEA) is the component of a PEMFC most prone to failure during durability testing [140], and is hence the limiting factor in attaining this goal. Exposure to impurities, potential cycling, fuel starvation, start/stop cycling and changes in temperature and relative humidity can have a significant effect on membrane durability [7].

Accelerated Stress Tests (ASTs) have been developed to simulate the coupled mechanical and chemical degradation of the membrane as degradation under normal operating conditions would require more than 4.5 years of uninterrupted testing for stationary applications until failure [7, 139]. Failure is generally defined either as a threshold irrecoverable drop in performance or by a threshold hydrogen crossover, indicative of the formation of a pinhole: an opening in the MEA which allows hydrogen and oxygen to mix and react directly.

In ASTs, mechanical degradation is accelerated by cycling the relative humidity of the cell [140-142]. Chemical degradation is accelerated by running the cell at open circuit voltage (OCV) at elevated temperature with dry gases [142, 143]. These tests lead to failure on the timescale of hundreds of hours [138, 141-145].

Accelerated mechanical degradation occurs due to the swelling and shrinking of the MEA under varying humidification conditions. The electrodes and the membrane dry at varying

rates, causing creep and membrane thinning, leading to the formation of perforations, cracks, tears, and pinholes [139, 140].

Ex-situ testing [144] shows that before a pinhole forms, thinning of the membrane can lead to the development of hotspots 2-3 °C higher than the rest of the cell. Stanic and Hoberecht [140] suggest that the elastic modulus of the membrane decreases with time due to polymer molecule reorganization to minimalize local stresses. The membrane thins to about 5 µm until there is no longer a sufficient barrier to prevent the reactant gases from mixing.

Chemical degradation occurs due to the presence of hydrogen peroxide across the membrane as a result of hydroxyl and hydroperoxyl free-radical formation [142]. Hydrogen peroxide has been found in the exhaust gas and drain water from fuel cells and although an MEA can remain chemically stable in 30% H_2O_2, the reaction with Cu^{2+} and Fe^{2+} impurities accelerates chemical degradation [146].

There have been varying mechanisms proposed for the formation of these free-radicals and conflicting results showing the formation of the free-radicals at the anode and progressing to the cathode [147], forming at the cathode and moving to the anode [148-150], and showing no discernible difference between the electrodes [151]. The accumulation of contaminants causes blistering and ultimately leads to the formation of a pinhole.

Thermal degradation is often not considered in ASTs as the MEA components are thermally stable up to 180 °C due to the strength of the C-F bond and the shielding effect

of fluorine, present in Nafion [139, 152]. Up to 180 °C, typically only 4% of the weight of the Nafion is lost, attributed to moisture elimination. Above 345 °C, the sulfonic groups split off the carbon backbone and total destruction occurs between 420 °C and 590 °C, where the oxidative destruction of the pre-fluorinated matrix occurs [153]. The heat produced by the MEA (around 0.13 W m^{-2}) is some 70 times lower than that required for ignition and total failure of the cell [140].

Inaba *et al.* reported a degradation rate of 83 μV h^{-1} while the cell was held at OCV running humidified gases, where a mechanical degradation technique coupled with a chemical degradation technique [142] leads to an OCV degradation rate of 700 μV h^{-1} prior to pinhole formation and 3900 μV h^{-1} after.

When a pinhole first forms, it does not significantly affect the fuel cell performance [142, 154, 155]. Pinholes of 100 – 250 μm in diameter formed by ASTs have been observed between under SEM, however when Huang *et al.* [155] used a pin to create a 700 μm pinhole it did not have an immediate or significant effect on the fuel cell performance. Continued operation can lead to further structural deformation, the pinhole widening, and eventual performance drop.

Using EIS, it was shown that the HF resistance does not change significantly with a small pinhole [142, 145, 155] under operating conditions. A segmented cell has been used to observe pinhole effects on local current densities [156]. At OCV, current was produced around the pinhole. However, under load, while most of the cell produced a net positive current, electrolysis occurred at the pinhole.

More recently, Reshetenko *et al.* [157] performed localised EIS measurements on an MEA with a pinhole using a segmented cell. They determined that at low current densities, there is little difference in the EIS spectra before and after a pinhole is formed. At higher current densities, the differences in the low-frequency region become more pronounced in the segments after the pinhole.

5.1.5 Thermal effects of pinhole formation

The thermal effects of pinhole formation in a PEM fuel cell have been mathematically modelled [154] and it has been shown that temperatures around the pinhole are 4 °C - 5 °C higher than under normal operation. Vengatesan *et al.* [141] demonstrated a post-mortem analysis technique of an MEA using thermal imaging. The MEA was placed in a cell where a low hydrogen flow rate was passed over the anode. The cathode was exposed to the atmosphere and imaged with a thermal camera. The temperature around the pinhole was almost 50 °C higher than the rest of the cell due to the pressure gradient across the MEA and contacted reaction of hydrogen and oxygen.

5.1.6 Aims of the study

Here, for the first time, ETIS is applied to a PEMFC to determine the frequency, polarisation, and spatially-dependent behaviour of the system and to inform the interpretation of lock-in images (electro-thermo-ampligrams). The open-cathode configuration allows for direct visualisation of the gas diffusion layer (GDL) and comparison of channel and land features.

Once the technique had been developed, it is applied to identify pinhole formation. Pinhole formation has not been previously modelled or imaged on an open-cathode PEM fuel cell. The added effects of a large pressure difference across the membrane and convection of air will result in different effects than previously modelled in a closed system. The pressure difference between the hydrogen fuel and the ambient air will force hydrogen through the hole at a higher rate than in a closed system and thus allow more reaction between hydrogen and oxygen, creating more heat around the pinhole.

5.2 Computational Modelling

In order to verify the changes in ETIS phase shift between the channel and land, heat-transfer computational modelling of the channel and land was performed in COMSOL Multiphysics. As this was a heat transfer model, it would not allow for the electro-thermal analysis to be directly compared to the experimental data, however the channel and land comparisons for each set of data could be compared.

The transient heat input was assumed to be uniform across the base of the GDL, as shown in Figure 5.1. Reflective boundaries were assigned to the model at x = 0 and x = 2 mm, to represent the distance to the subsequent land either side of the channel.

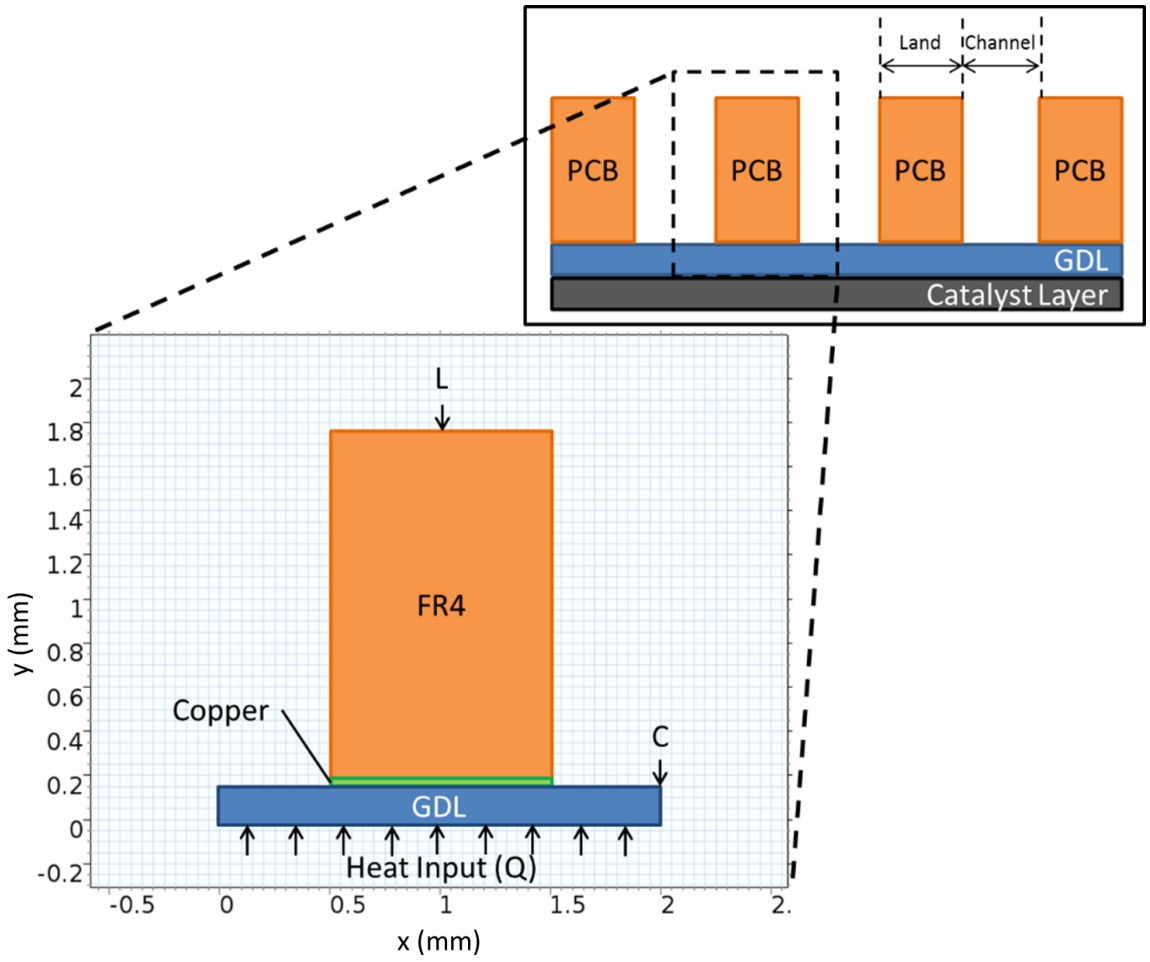

Figure 5.1 – In-plane drawing of PCB cathode fuel cell model. The land temperature measurement is taken at the centre of the top of the FR4, labelled "L", and the channel temperature is taken at the centre of the gap between lands, labelled "C."

Fourier's Law describes heat flux through a solid as a function of thermal conductivity and the temperature gradient [158]. As the system considered is time dependent due to the transient behaviour of the heat input and temperature output, we consider the heat equation for a solid, immobile system [159]:

$$\rho C_p \frac{dT}{dt} = \nabla \cdot (\mathrm{k}\nabla T) + Q$$

Equation 5.1 – Heat balance for a solid, immobile system

By defining the material density, specific heat, and thermal resistance as well as the transient heat input, the model is left to solve for the temperature.

The following parameters were used for the model:

FR4 [160]	ρ	1900 kg m^{-3}
	C_p	600 J kg^{-1} K^{-1}
	k	0.3 W m^{-1} K^{-1}
Copper [161]	ρ	8700 kg m^{-3}
	C_p	385 J kg^{-1} K^{-1}
	k	400 W m^{-1} K^{-1}
GDL [162]	ρ	440 kg m^{-3}
	C_p	1000 J kg^{-1} K^{-1}
	k	1.7 W m^{-1} K^{-1}
Heat Input	Q	0.3 + 0.03 sin(2πft) [W cm^{-2}]

Table 5.1 – Material parameters used for ETIS model

The heat input is roughly based on a fuel cell operating at 50% efficiency.

5.3 Results and discussion

In order to validate the performance of the PEMFC, EIS was performed on the open-cathode PCB fuel cell design (Figure 3.4) and shown in Figure 5.2.

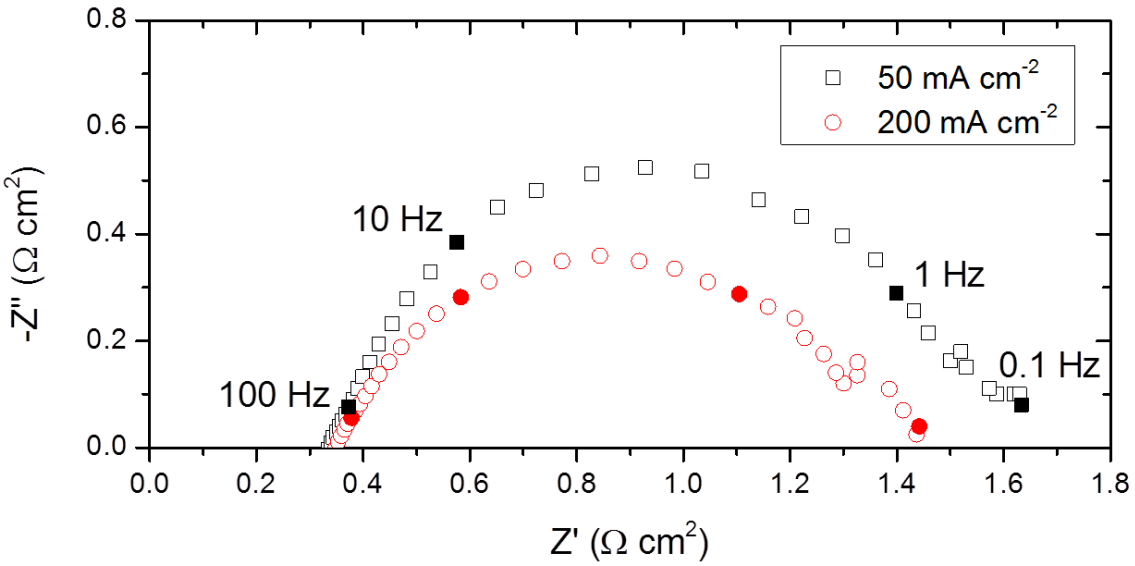

Figure 5.2 – Galvanostatic EIS of the open-cathode PEMFC from 1 kHz to 100 mHz at 50 mA cm^{-2} and 200 mA cm^{-2}. Dry hydrogen was supplied at ambient temperature and 100 mL min^{-1}. A sinusoidal perturbation of amplitude 3 mA cm^{-2} was applied to the PEMFC.

The EIS impedance arcs show similar performance as shown in previous studies by Obeisun *et al.* [88, 89, 91]. The low-frequency intercept, indicative of the charge transfer

resistance, at both 50 mA cm^{-2} and 200 mA cm^{-2} are within 5 % and the high-frequency intercept, indicative of the Ohmic resistances, are within 2% of the previous studies.

5.3.1 ETIS development

In order to determine an appropriate amplitude of the current perturbation, the relative temperature responses to 1, 2, 3, and 5 mA cm^{-2} peak amplitude current perturbations were investigated.

Figure 5.3 shows the thermal responses in the time domain under a 0.1 Hz current perturbation with a 30 mA cm^{-2} direct current (dc) offset. It can be seen that a 3 mA cm^{-2} current perturbation was enough to elicit a clear, periodic temperature response. Under these conditions, the perturbation is comparable to those typically used in EIS studies [163, 164] and hence does not significantly perturb the system.

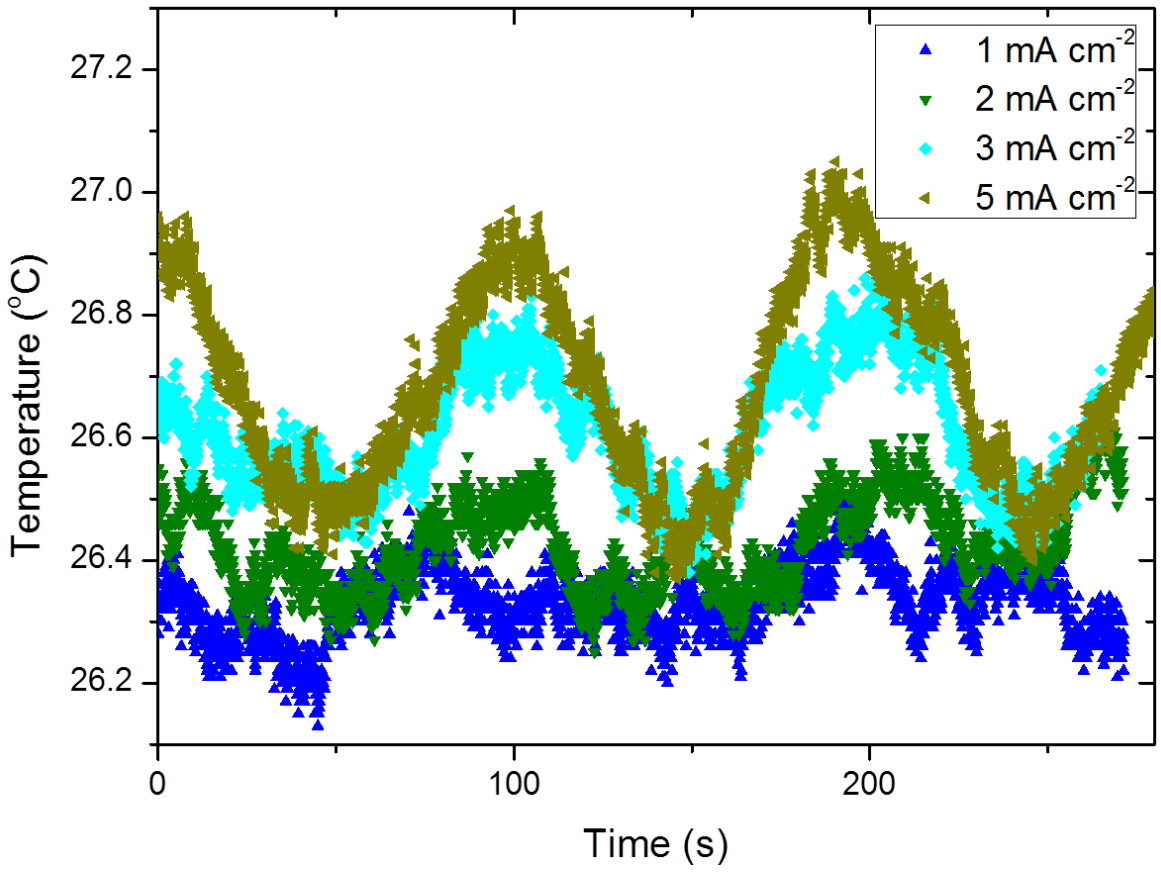

Figure 5.3 - Temporal temperature responses to current stimuli of 1, 2, 3 and 5 mA cm^{-2} peak amplitude. The perturbations had a constant frequency of 0.1 Hz with a 30 mA cm^{-2} dc offset. Temperatures were recorded in a region near the middle of the fuel cell cathode using a thermal imaging camera.

A 3 mA cm^{-2} peak amplitude current perturbation was applied to the system with a fixed 30 mA cm^{-2} and 250 mA cm^{-2} dc offset. A sinusoidal fit was applied to the current perturbation and temperature response in the form of Equation 5.2:

$$i, T\ (\mathrm{A}, ^{\circ}\mathrm{C}) = A_{i,T} \sin\left(2\pi\omega t + B_{i,T}\right) + C_{i,T}$$

Equation 5.2 – Standard fitting of ETIS stimulus and response

Where *A* is the peak amplitude of the waveform, ω is the frequency, *t* is time, *B* is the time offset, and *C* is the current (*i*) or temperature (*T*) offset. The raw data were post processed in MATLAB and fitted to the equation by minimising the root mean square error between the fitted equation and data. An example of the current and temperature data to which Equation 5.2 was applied is shown in Figure 5.4.

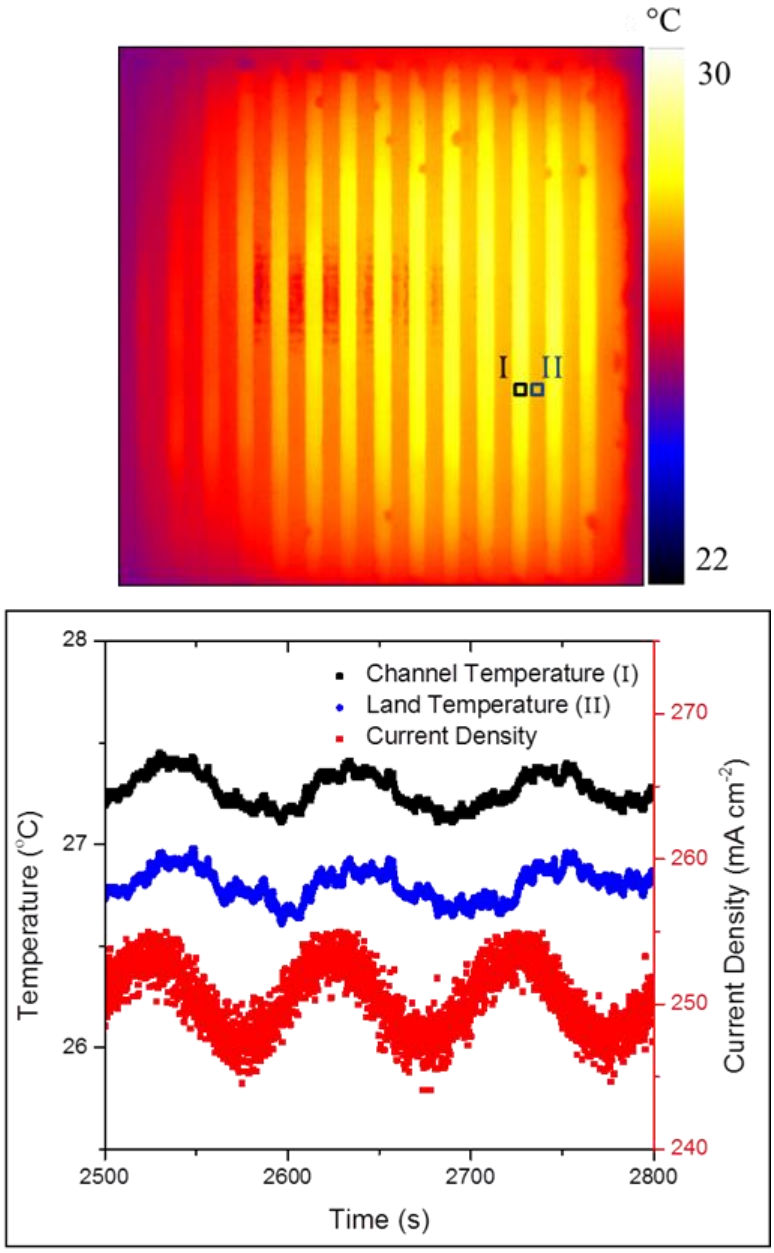

Figure 5.4 - Thermal image (top) depicting the area of the channel (I) and of the land (II) considered. Temporal data (bottom) of current stimulus (red) plotted with the temperature response of the channel (black) and land (blue) acquired from thermal imaging. A fit in the form of Equation 5.2 was applied to the current and temperature signals in order to determine the amplitude and time offset of each signal.

Subsequently, the amplitude ratio (*AR*) at each frequency can be evaluated as the relative peak amplitude of the thermal response (A_T) and current perturbation (A_i).

$$\mathrm{AR}(^{\circ}\mathrm{C\ A^{-1}cm^{2}}) = \frac{A_T}{A_i} = \frac{A_T}{0.003\ \mathrm{A\ cm^{-2}}}$$

Equation 5.3 – Amplitude ratio of ETIS based on sinusoidal fitting

The phase shift is the difference in the time off-set between the temperature (B_T) and the current (B_i).

$$\emptyset(\mathrm{degrees}) = (B_T - B_i)\frac{180}{\pi}$$

Equation 5.4 – Phase shift of ETIS based on sinusoidal fitting

The thermal response was measured at places where liquid water was not present, near the bottom and top of the cathode flow field, as seen in Figure 5.5. The thermal response while performing ETIS in these cold spots is dampened due to the added thermal resistance. Moreover, due to evaporation, the heating of the liquid water is not necessarily periodic and fails to satisfy a fundamental transfer function criterion.

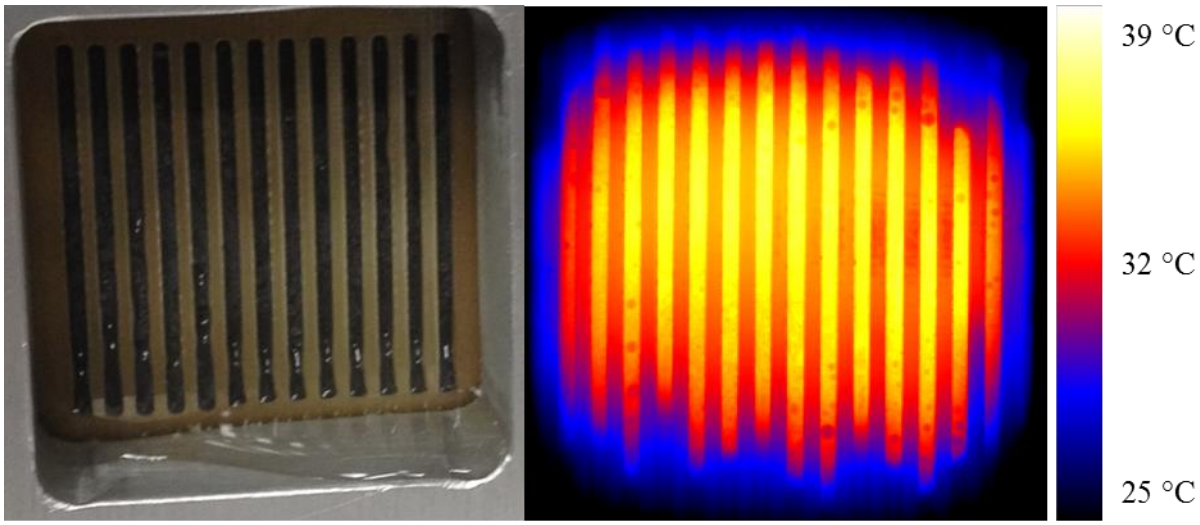

Figure 5.5 – White light image (left) and IR image (right) of the open cathode PEMFC. Flooding occurs near the bottom of the cathode flow-field, forming a puddle of liquid water on the aluminium backing plate and causes darker spots to appear in the thermal image.

5.3.2 Comparison of channel and land

The amplitude ratio and phase shift were plotted as a function of frequency for an area in the middle of a cathode open channel and an area in the adjacent land. The Bode plot for these measurements is shown in Figure 5.6.

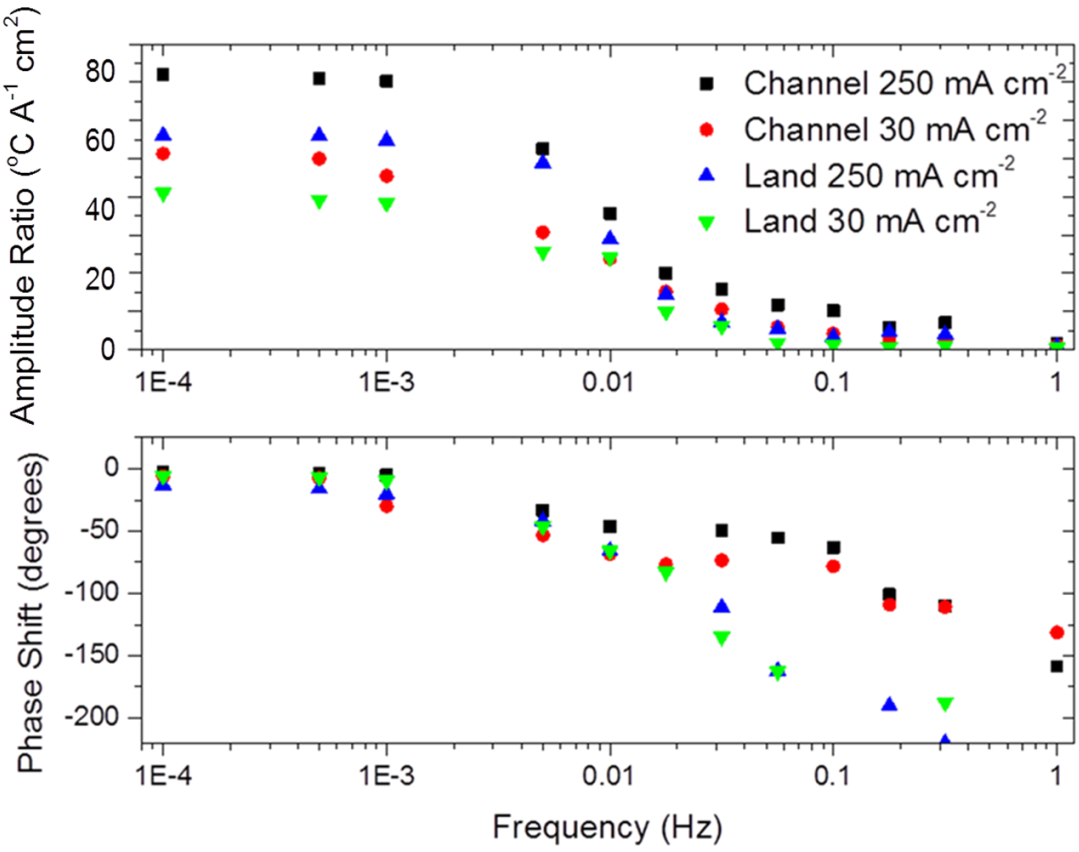

Figure 5.6 - ETIS Bode plots (amplitude ratio – top, and phase shift – bottom) for channel and land locations at 30 mA cm^{-2} and 250 mA cm^{-2}. The plot demonstrates the relationship between the temperature response and current stimulus as a function of

frequency and location. The system was perturbed with a fixed 3 mA cm^{-2} peak amplitude current stimulus.

From Figure 5.6, it can be observed that at low frequencies (below 1 mHz) the magnitude of the amplitude ratio is significantly greater in the channel location than in the land location, for both respective direct current offset values. This is due to the presence of the land which gives rise to an additional thermal impedance, thus damping the temperature response.

Additionally, at 250 mA cm^{-2}, there is a greater low-frequency amplitude ratio than for 30 mA cm^{-2}. Due to the fact that the amplitude of the current perturbation is fixed for both dc current densities, the higher amplitude ratio means that the differential heat generation term is more significant under the higher loading condition. The higher amplitude ratio may be related to decreased efficiency of heat dissipation at the higher current density.

With increasing frequency, the amplitude ratios decrease and converge as the modulation wavelength moves away from the characteristic thermal diffusion length of the fuel cell features.

Below 1 mHz, the magnitude of the phase shift in the channel and land locations is near zero at both dc current densities, indicating that the system has had sufficient time to thermally equilibrate. With increasing frequency, the magnitude of the phase shift increases more rapidly for the land, due to the added thermal diffusion length of the land compared to the channel, i.e. the temperature of the land moves out-of-phase with the

current stimulus at a faster rate than the channel. The difference in phase shift between the channel and land at 200 mHz is approximately 100 degrees. The phase shift profile across the spectrum between the two dc current densities does not vary significantly and thus the phase shift is not sensitive to polarisation.

5.3.3 Computational verification of phase shift

The difference in phase shift at 200 mHz is 100°, representative of a 1.3 s difference in the thermal response for the additional 1.6 mm of material between channel and land. In order to determine whether or not this lag was reasonable, computational modelling was conducted in COMSOL Multiphysics.

The model presented was written as a thermal, not electrochemical, study, hence investigation of the absolute values of the amplitude ratio and phase shift were not feasible.

However, the relative magnitudes of the channel and land response were relevant. The normalised amplitude ratio of the channel of the experimental and computational results, as well as the phase shift between the channel and land for both sets of data, are presented in Figure 5.7.

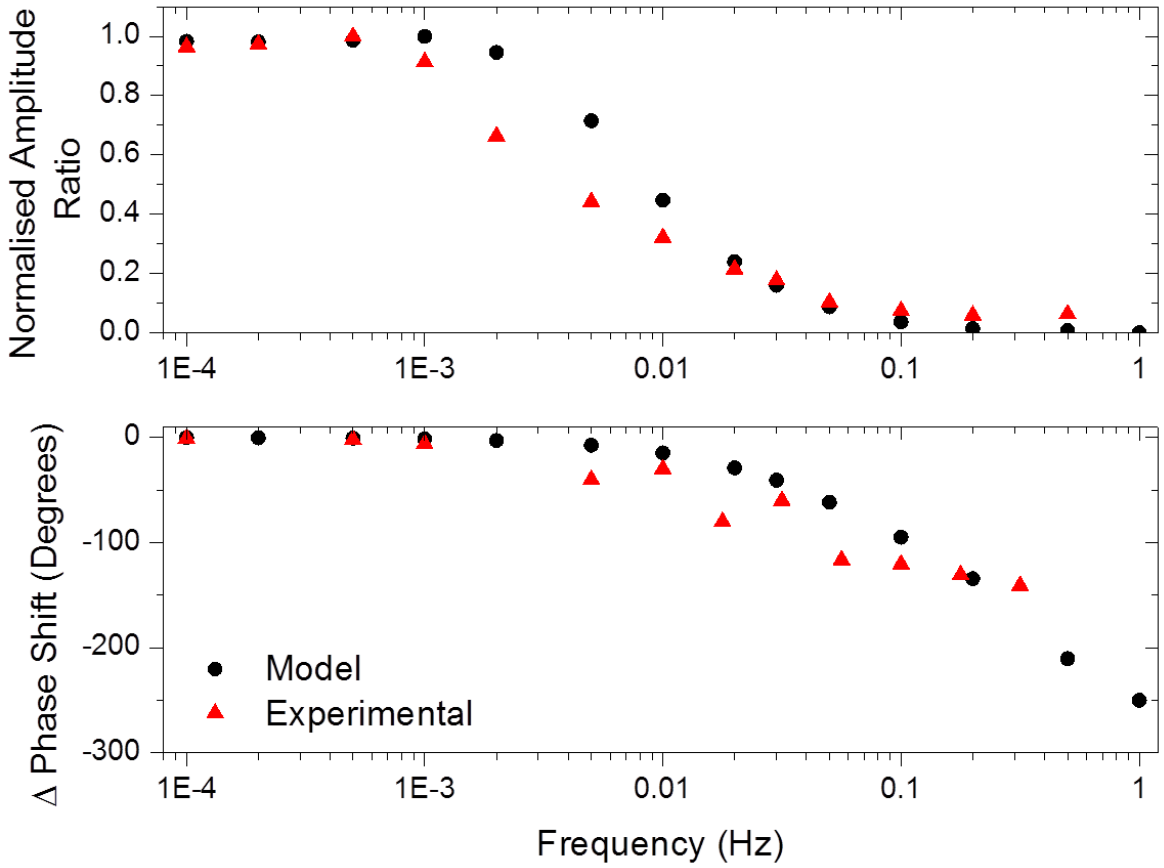

Figure 5.7 - ETIS Bode plots (amplitude ratio – top, and phase shift – bottom) comparing experimental and computational results. Amplitude ratios of the channel are normalised relative to their maximum value for both sets of results. The phase shift is represented as a difference in phase between the channel and land.

The computational and experimental results show good agreement, particularly at high (> 10 mHz) and low (< 1 mHz) frequencies. The slight differences in the intermediate frequencies may be a result of not including natural convection in the computational model.

It can be expected that if natural convection were included in the model, the heat would be lost more rapidly to the atmosphere and hence the amplitude ratio of the computational data would decrease more closely with the experimental data.

The phase shift shows good agreement within the frequency range investigated. The computational model provides further evidence that a difference in phase shift of up to -100° at 200 mHz between the channel and land is reasonable. In fact, the phase shift from the computational model continues to decrease to -300° at 1 Hz. Experimentally, the phase shift at this frequency cannot be verified due to the low magnitude of the temperature response, which is concealed in noise.

5.3.4 Spatial variation of amplitude ratio and phase shift

Following the comparison of ETIS behaviour between channel and land, the spatial variation of amplitude ratio and phase shift was investigated by observing the transient behaviour of five different regions of the cathode channels. These five regions, shown in Figure 5.8, were chosen distinctly as near the top and bottom of the cathode, without static water.

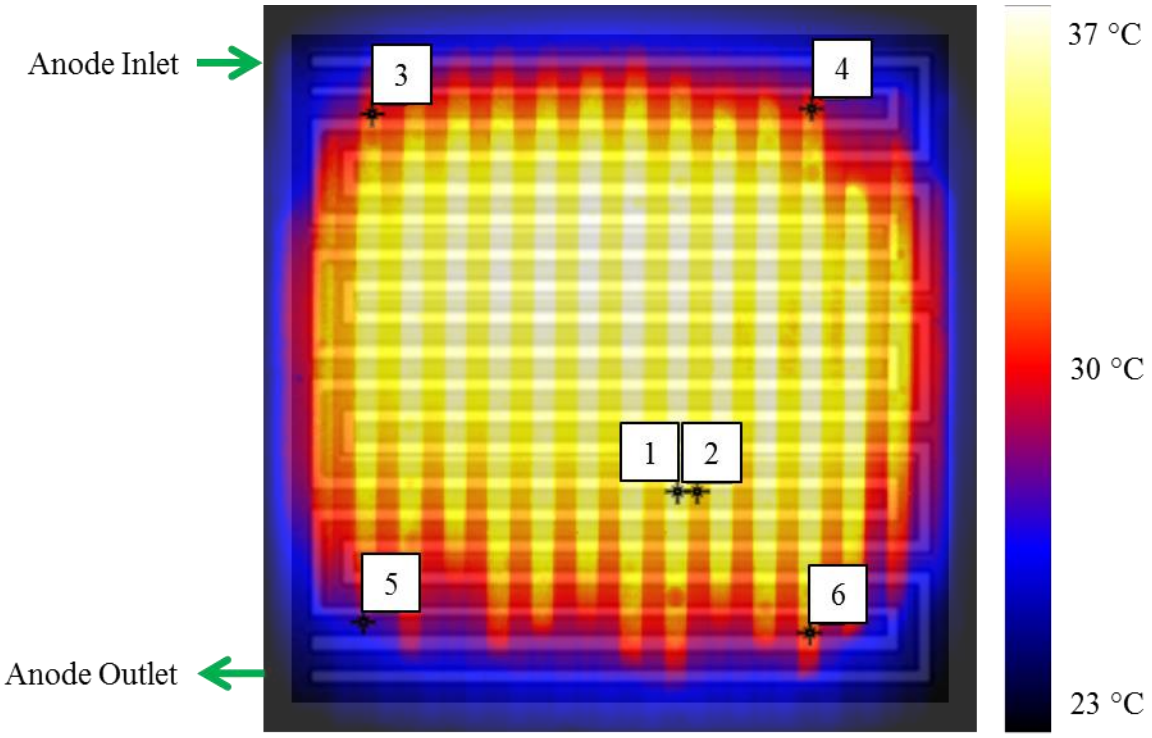

Figure 5.8 - Thermal image of the PEMFC cathode with anode double serpentine flow field overlaid. Areas 1 and 2 are representative of the channel and land area near the centre of the MEA. Areas 3, 4, 5, and 6 are all channel locations near the corners of the anode.

ETIS was applied to the five selected channel regions (the second point highlighted refers to the land investigated in Section 5.3.2) at 250 mA cm^{-2}. The amplitude ratio and phase shift are shown in Figure 5.9 and assumes there is no variation in local current densities.

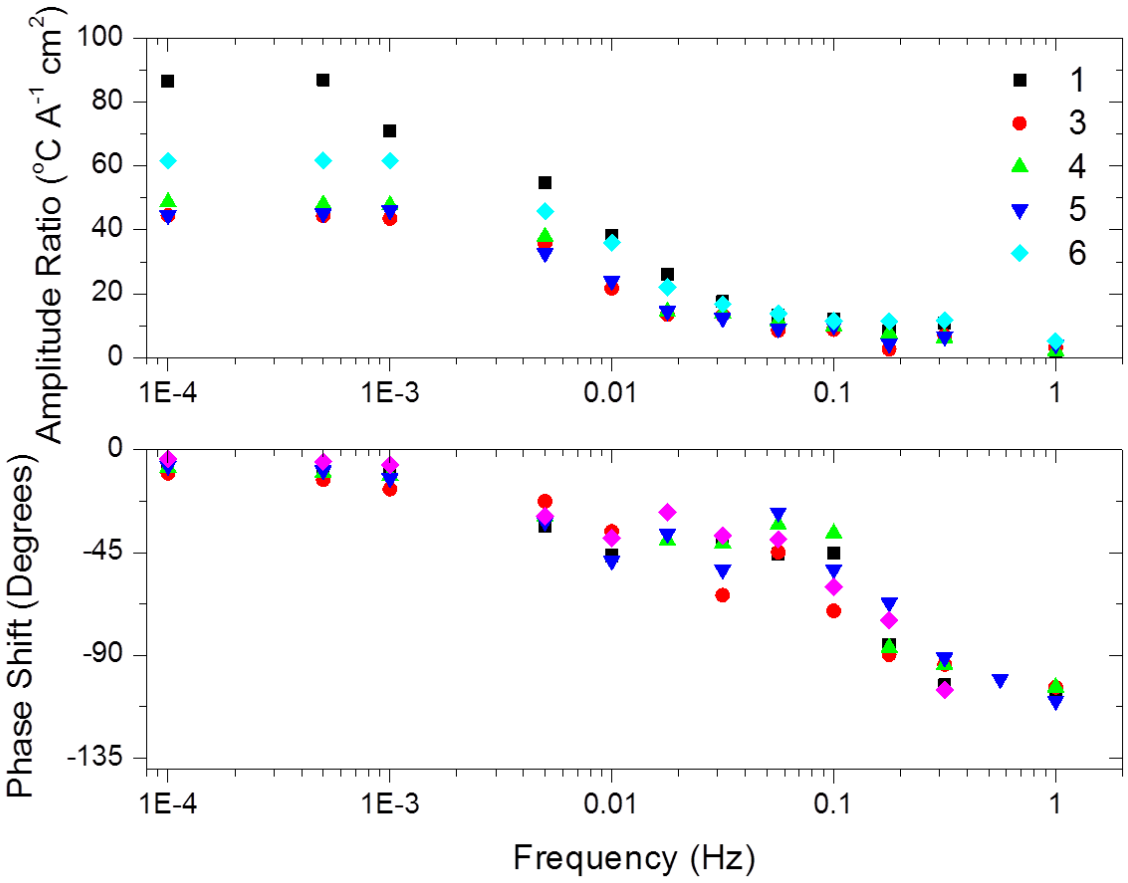

Figure 5.9 - ETIS Bode plots (amplitude ratio – top, and phase shift – bottom) for five channel locations at 250 mA cm^{-2}. The plot demonstrates the relationship between the temperature response and current stimulus as a function of frequency and location. The system was perturbed with a fixed 3 mA cm^{-2} peak amplitude current stimulus.

The amplitude ratios for the five regions are all quite similar, with the exception of area 1 which has a higher *AR* at lower frequencies. This is perhaps due to the fact that there is less static water around this region, and hence less of a heat sink, allowing for a larger

thermal response. The areas around the edges are all near water droplets and the aluminium end plates, as seen in Figure 5.8.

The phase shift for all five points, however, is very similar. This may be due to the fact the thermal diffusive length from the catalyst layer to the surface of all parts of the channel is similar, so little variation is expected.

It is impractical to investigate the entire surface of the fuel cell in this way; therefore, in order to investigate the spatial variation of the amplitude ratio at increased resolution, lock-in imaging was applied to the PEMFC. By selecting individual frequencies, ETIS could be performed quickly, at high spatial resolution.

At different dc current densities, the lock-in technique was applied to generate electro-thermo-ampligrams at two different frequencies, selected from the ETIS spectrum. Electro-thermo-ampligrams are topographical representations of the ETIS amplitude ratio at a fixed frequency.

Figure 5.10 compares the conventional thermograms (a, d) to the electro-thermo-ampligrams at 100 mHz (b, e) and 1 mHz (c, f) for dc current densities of 30 mA cm^{-2} (a-c) and 250 mA cm^{-2} (d-f).

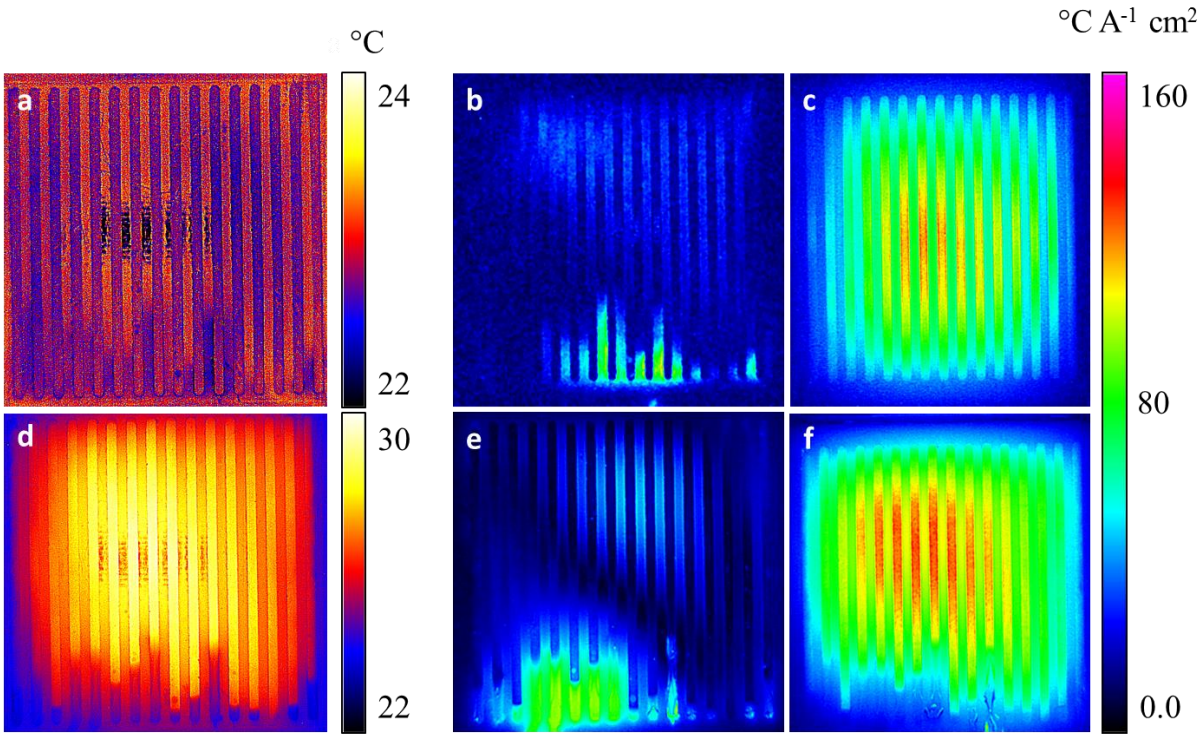

Figure 5.10 - Thermograms (a,d) and electro-thermo-ampligrams at 100 mHz (b, e) and 1 mHz (c, f) of a PEMFC open cathode at 30 mA cm^{-2} (a-c) and 250 mA cm^{-2} (d-f). The system was perturbed with a fixed 3 mA cm^{-2} peak amplitude current stimulus.

Artefacts caused by the Narcissus Effect, i.e. the reflection of the lens on the surface of the sample [49, 165], can be observed in the centre of the thermograms - Figure 5.10(a) and Figure 5.10(d). Additionally, the channels appear to be cooler than the lands in Figure 5.10(a), when in fact the channels are warmer than the lands due to the generation of heat in the electrode. This is a consequence of the difference in emissivity of the two materials and is a major challenge for IR thermography in general. The application of alternating current (ac) thermography automatically corrects for differences in emissivity

and the reflections do not appear in the electro-thermo-ampligrams (b, c, e, f). Removal of such artefacts is a major advantage of the ETIS technique.

At 100 mHz, the amplitude ratios - and consequent contrast in the images in Figure 5.10(b) and Figure 5.10(e) - are much lower than at 1 mHz, in agreement with the manually calculated values in Figure 5.6. The electro-thermo-ampligrams explicitly show where heat is generated, not just the temperature distribution. As such, the dc and ac techniques are highly complementary.

By definition, the electro-thermo-ampligram is sensitive to temperature changes caused by the current stimulus and insensitive to absolute temperature; so parameters that change as a consequence of the current cycle can be targeted. For example, since water generation is linked to current, there is the possibility to target its formation and removal.

As water generation will change the thermal conductivity of the GDL, there is even the possibility of identifying water generated *within* the GDL or *under* lands. When comparing the bottom of the flow-field in Figure 5.10(c) and Figure 5.10(f), the higher current case leads to lower amplitude ratios in both the channel and the land locations. Visual inspection shows that this is correlated with water formation, acting as a barrier to heat transfer. Conversely, since heat generation from pinhole formation is not related to the flow of current, a hot spot due to a pin hole in the membrane will be identifiable by a thermogram, but not by an electro-thermo-ampligram.

5.3.5 Identification of land “bowing” using ETIS

“Bowing” can be a problem in stack manufacturing as uneven compression of the tying bolts that hold the stack together can result in insufficient contact of the BPP lands with the GDL. Fuel cell performance is decreased due to high contact resistance and areas where there is no physical contact between GDL and current collector will fail to draw current, limiting the electrochemical activity in the affected region. Bowing can be induced on the single cell by applying uneven, or insufficient, torque to bolts of the open cathode fuel cell [89].

With the knowledge that 1 mHz was a suitable frequency to observe differences in thermal resitance for this system, lock-in thermography was applied to the PEMFC to produce an electro-thermo-ampligram to identify any deviation from its regular operation.

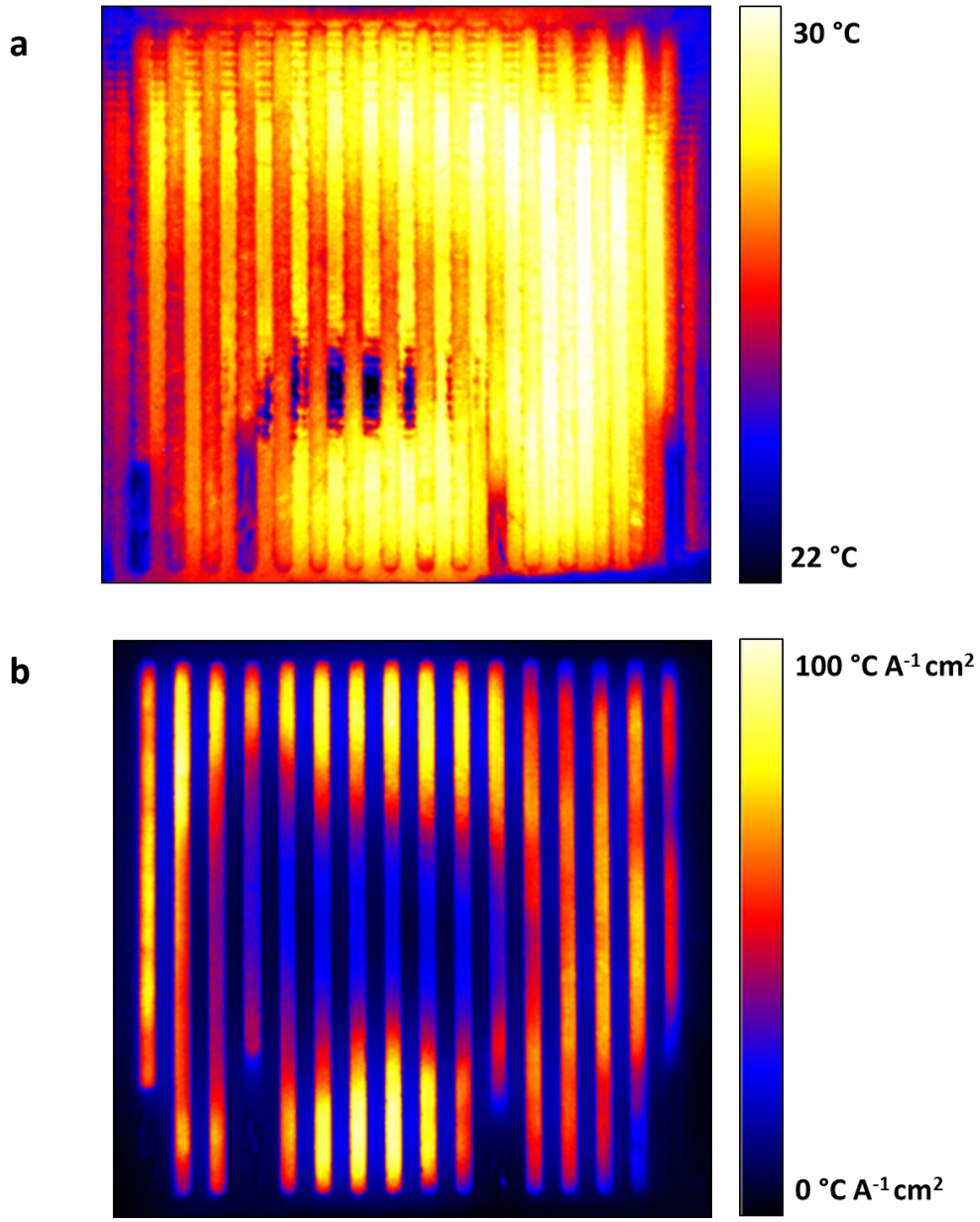

Figure 5.11 – Average thermogram (a) and electro-thermo-ampligram (b) at 1 mHz and 250 mA cm^{-2}. The system was perturbed with a fixed 3 mA cm^{-2} peak amplitude current stimulus. 2 N m of torque were applied to bolts at the top left and bottom right of the images, with 1 N m of torque applied to the bolts on the top and bottom right.

From Figure 5.11 (a), the thermal image does not definitively demonstrate a problem with the PEMFC's operation, although there is an apparent higher temperature on the right-hand side of the fuel cell of approximately 4 °C compared to the left-hand side.

However, the electro-thermo-ampligram, Figure 5.11 (b) clearly indicates there is a lack of electro-thermal activity at the centre of the flow-field. While the centre of the flow-field appears to be warm, the image reveals that the heating of this area is not due to an electro-thermal effect and is effectively not electrochemically active due to poor contact of the land on the GDL. The edges around the dark spot appear active, in an inverse to the normally operated cell seen in Figure 5.10 (f).

5.3.6 Identification of pinhole formation using ETIS

The effectiveness of ETIS in detecting pinholes in the membrane was evaluated using the MEA from the previous had been subjected to repeated start-up and shut down events and cycling of humid and dry anode gases. No evidence of pinhole formation was observable with EIS as shown in Figure 5.12. Due to the small amount of reactant crossover, the cell EIS spectrum varied very little from the unaltered MEA, as observed in previous studies [156, 157]. The low-frequency resistance for the pinhole EIS spectra at both polarisations were within 3% of the unaltered value, and the high-frequency values were within 1% of the original value. Similarly, the presence of a pinhole was not immediately obvious from the thermogram when the cell was polarised due to the

relatively small measured temperature difference between any pinhole and the hotter areas of the fuel cell.

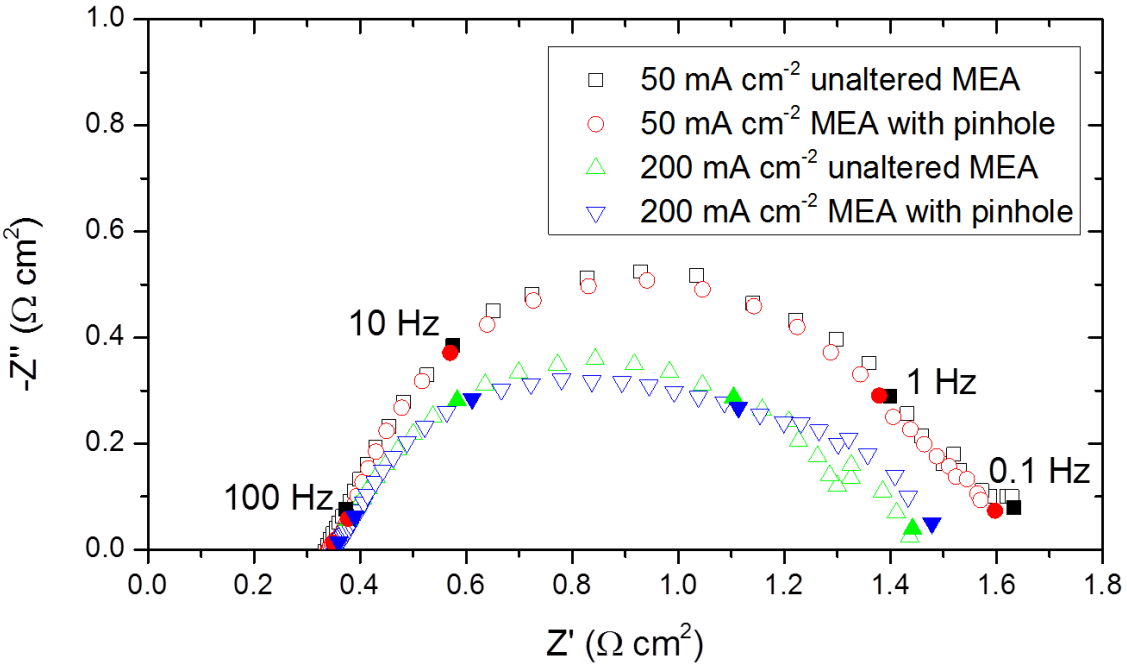

Figure 5.12 - Galvanostatic EIS of the open cathode PEMFC from 1 kHz to 100 mHz at 50 mA cm^{-2} and 200 mA cm^{-2}, with and without a pinhole in the MEA. Dry hydrogen was supplied at ambient temperature and 100 mL min^{-1}. A peak to peak perturbation of 3 mA cm^{-2} was applied to the PEMFC.

ETIS was then applied at 1 mHz; the electro-thermo-ampligram as well as relevant thermograms are shown in Figure 5.13.

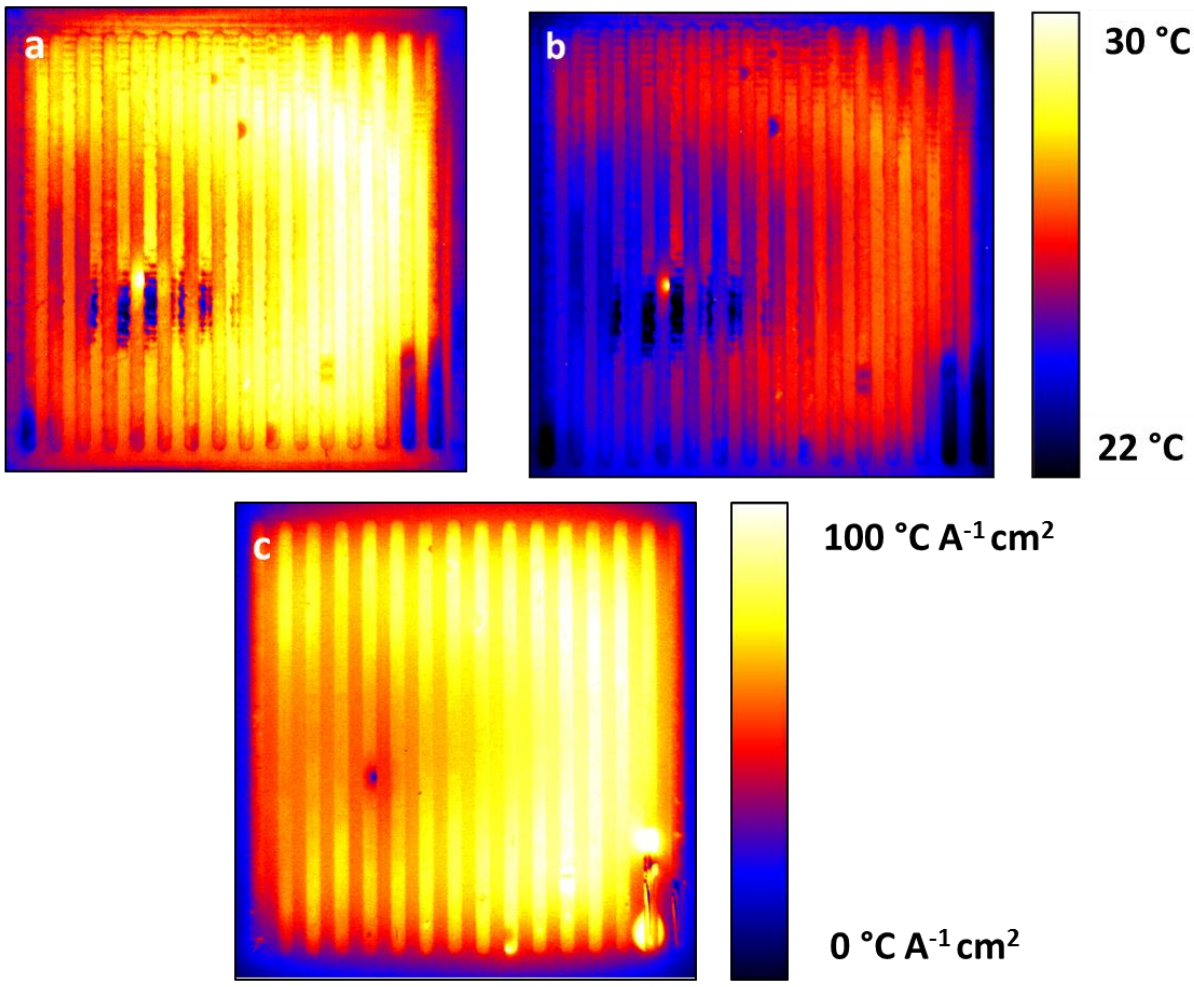

Figure 5.13 - Thermograms of the fuel cell with a pinhole at 250 mA cm^{-2} (a) and 0 mA cm^{-2} (b). The electro-thermo-ampligrams at 1 mHz and 250 mA cm^{-2} (c) was generated with a fixed 3 mA cm^{-2} peak amplitude current stimulus.

A pinhole was evident adjacent to the fifth land from the left-hand side of the fuel cell but was not easily identifiable from the thermogram when the cell was polarised at 250 mA cm^{-2}, Figure 5.13 (a). This is due to the fact that while there is a reaction between hydrogen and oxygen at the pinhole, heat is still generated elsewhere in the fuel cell

through the polarisation of the fuel cell. The pinhole becomes much clearer in the thermogram at OCV, Figure 5.13 (b), where the only form of heat generation is from the crossover of hydrogen to the cathode at the pinhole.

However, it is possible to clearly identify the pinhole while it is polarised using the electro-thermo-ampligram, Figure 5.13 (c). Because the heat generated from the pinhole is not an electro-thermal effect, it appears in black at 0 °C A^{-1} in the electro-thermo-ampligram. Moving away from the pinhole, the amplitude ratios increase, particularly at the top and right-hand side of the cell, where the bulk electro-thermal effect is occurring.

5.4 Summary

ETIS has been applied to a PEMFC for the first time to determine the frequency, polarisation, and spatial-dependence of the thermal response of the fuel cell when a periodic current perturbation is applied. A greater thermal diffusive length between the source of the heat and surface of the system yields a greater phase shift and lower amplitude ratio.

Based on the ETIS analysis, frequencies can be selected in order to achieve greatest image contrast or tune the technique to identify different features in the electro-thermo-ampligram. As such, DC and AC thermography are highly complementary and allow current-dependent features such as water generation to be decoupled from the absolute temperature distribution and non-current-dependant effects.

The electro-thermo-ampligrams were used to identify electro-thermal faults or contrasts such as bowing of current collectors and pinhole formation which were not immediately obvious by existing, widely used electrical diagnostic techniques.

Chapter 6

Electrochemical pressure impedance spectroscopy applied to a PEMFC

Portions of this chapter are reproduced in part with permission from "Electrochemical pressure impedance spectroscopy applied to the study of polymer electrolyte membrane fuel cells", E. Engebretsen, T. J. Mason, P. R. Shearing, G. Hinds, and D. J. L. Brett, *Electrochemistry Communications*, vol. 75, pp. 60 - 63, Copyright (2016) Elsevier B.V. [166]

Having investigated the thermal properties of an open-cathode fuel cell and failure mechanisms with thermo-electric effects, another major facet of fuel cell performance was explored: mass transport limitations. In particular, the frequency dependent electrical performance as a function of the cathode back pressure was investigated.

6.1 Introduction

It is well known that the performance of a PEMFC can be improved by applying a backpressure to the cathode [167-172]. The performance improvement becomes more pronounced at higher current density [168] but can also detrimentally increase gas crossover, cost, size, and weight of a PEMFC system. Furthermore, the increased partial pressure of reactant gas has an influence on the Nernst potential and the current distribution due to the higher oxygen concentration at the cathode [173], with a consequent decrease in membrane resistance due to the increase in membrane water content [174].

6.1.1 EPIS applied to batteries

The relationship between gas pressure and electrochemical performance, using electrochemical pressure impedance spectroscopy (EPIS), has been used to study the pressure dynamics in metal–air batteries under voltage and current cycling. Hartmann *et al.* [175] developed a system in which the pressure of an oxygen reservoir in a sodium-oxygen battery was varied and the electrochemical response was measured for selected frequencies.

Grübl *et al.* [176] verified the work with a mathematical model of the cell. Niroumand *et al.* [177] demonstrated the voltage response under cathode pressure perturbation at a single frequency, noting that the pressure and voltage were counter-intuitively out of

phase; as pressure increased, potential decreased. They identified this could have been because of dynamics of water at the catalyst layer.

In this chapter, the reactant gas pressure is perturbed and the electrical response monitored; the opposite of the cause-effect relationship is not investigated.

By studying the relationship between reactant gas pressure and electrochemical response as a function of modulation frequency, it may be possible to isolate the pressure effects of oxygen concentration on the cathode, Nernst potential, and membrane water content. In itself, this is a powerful diagnostic but it is also highly complementary to EIS, as processes that cannot be resolved due to similar time constants in the current/voltage regime may be determined by EPIS, e.g. mass transport effects associated with a hydration imbalance caused by water build-up or changes in reactant distribution.

6.2 Results and discussion

6.2.1 Fixed Cathode Pressure Measurements

The effect of cathode backpressure on the polarisation performance of the closed-cathode, 5 cm^2 Scribner fuel cell is shown in Figure 6.1. As previously reported [173], increased backpressure results in increased performance; the effect at OCV is relatively small but the performance enhancement becomes more pronounced with increasing current density [168, 169, 172]. While the reactant gas pressure affects the Nernst potential at all current densities, the effect of a higher pressure has a much more significant effect on the PEMFC performance [169, 173]. Between 0 kPa_g and 62.1 kPa_g there is an improvement of ~150 mV at 1600 mA cm^{-2}, as opposed to just 10 mV at OCV. As the effect is most significant at higher current densities, it is likely due to factors relating to water management and reactant access.

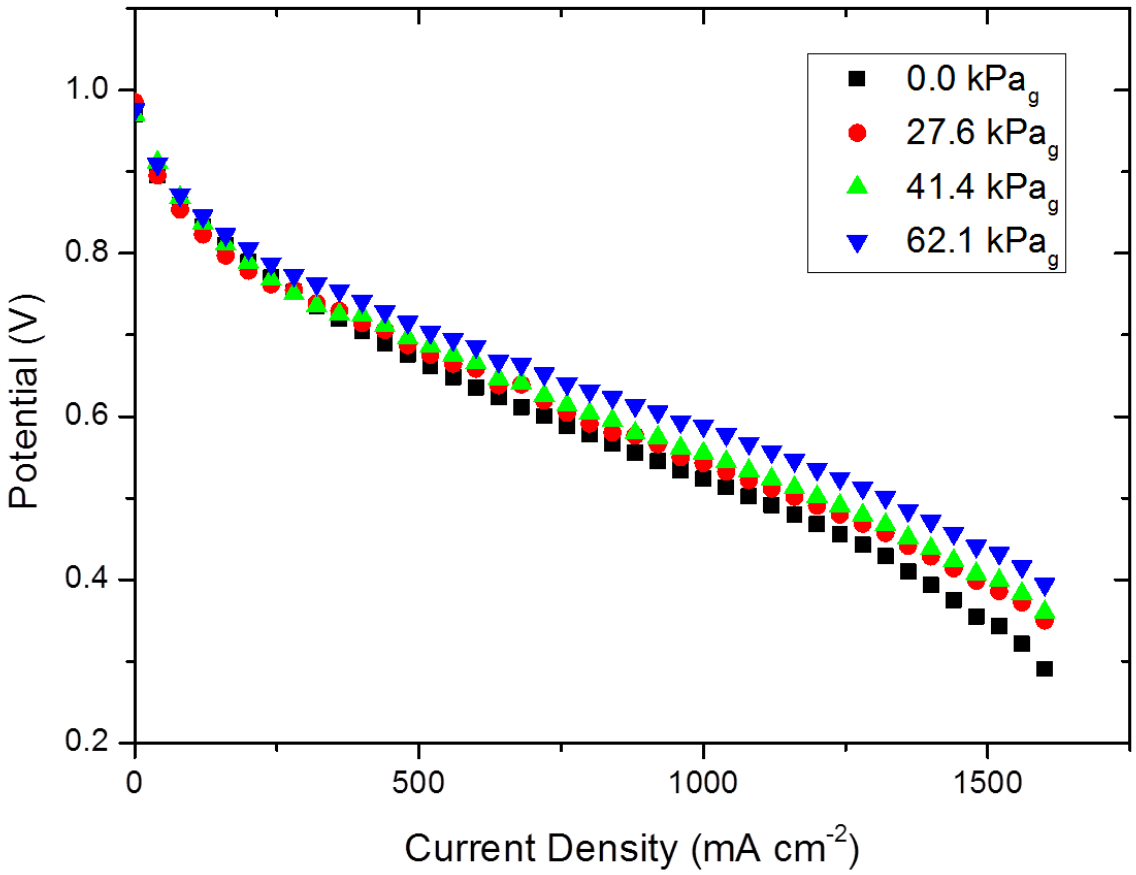

Figure 6.1 – Polarisation curves at varying cathode backpressures with humidified hydrogen (70 % RH) supplied at 100 mL min^{-1}, 60 °C to the anode and humidified air supplied at 250 mL min^{-1}, 60 °C to the cathode. The cell was operated at 70 °C in galvanostatic mode.

Figure 6.1 also suggests that increasing pressure linearly does not necessarily mean the voltage also increases linearly. At higher current densities, it can be seen that the improvement in cell potential from having no back pressure to 27.6 kPa$_g$ is greater than when increasing the back pressure from 27.6 to 41.4 kPa$_g$. In order to have a better

understanding of the rate of change of voltage with pressure, a "pressurisation curve" was measured, where the current density was fixed and the cathode back pressure was increased. These results are shown in Figure 6.2.

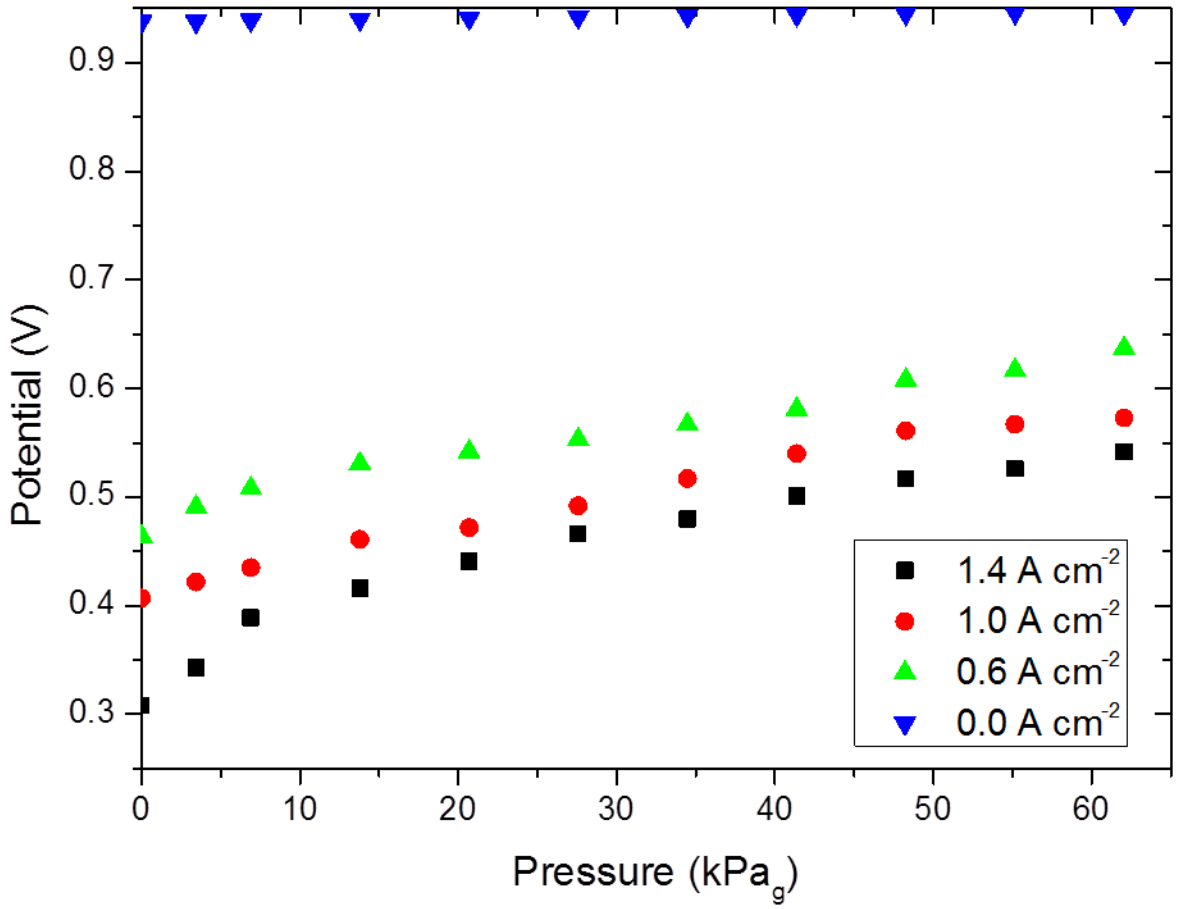

Figure 6.2 – Pressurisation curves at 0, 0.6, 1.0, and 1.4 A cm^{-2}. The pressure is increased on the cathode side only. Humidified hydrogen (70 % RH) was supplied at 100 mL min^{-1}, 60 °C to the anode and humidified air supplied at 250 mL min^{-1}, 60 °C to the cathode. The cell was operated at 70 °C galvanostatically.

From the pressurisation curve, it can be observed that at OCV (0 A cm^{-2}), there is a relatively small increase in voltage, 7 mV from 0 kPa_g to 62.1 kPa_g. This is in the expected range of a Nernstian response; 6.2 mV (from Equation 2.5). For current densities above this, there is a much more pronounced performance improvement. When increasing the cathode back pressure from 0 to 7 kPa_g, the improvement in potential is more rapid than the improvement between 13 and 62 kPa_g. At 1.4 A cm^{-2}, the first gradient is ~12 mV kPa_g^{-1} and the second is ~3 mV kPa_g^{-1}. This is beneficial for the proposed EPIS system as it can only operate at atmospheric pressure due to the limitation introduced by the speaker's operating pressure.

6.2.2 EPIS development at fixed flow rates

By analogy to EIS, the minimal modulation that can deliver a measurable response should be used in order to ensure a linear relationship between cause and effect and perturb the fuel cell as little as possible. The speaker system provided a peak amplitude pressure perturbation of 60 Pa across the measured frequency range. While this is two orders of magnitude lower than the pressures investigated in Figure 6.1 and Figure 6.2, it was large enough to elicit a transient voltage response. The maximum observed fuel cell voltage response to the pressure perturbation was 5 mV, which is comparable to the amplitude of a perturbation required to perform EIS on a system of a similar size [21, 87, 129].

The upper-frequency limit of the cathode backpressure perturbation was determined by the magnitude of the fuel cell voltage response. Above 100 Hz, the pressure perturbation

was found to yield a voltage response too small to reliably apply a sinusoidal fit. The lower frequency limit was determined by the amplitude of the pressure perturbation; below 10 mHz the pressure perturbation began to drop below 60 Pa.

A sinusoidal fit over a minimum of 8 cycles was applied to the backpressure perturbation and voltage response signal at each frequency using Equation 6.1:

$$P, V\ (\mathrm{Pa, V}) = A_{P,V} \sin\left(2\pi\omega t + B_{P,V}\right) + C_{P,V}$$

Equation 6.1 – Sinusoidal fitting for EPIS pressure and current signals

Where *A* is the peak amplitude of the wave, ω is the frequency, *t* is the time, *B* is the time offset, and *C* is the fixed backpressure (*P*) or voltage (*V*) offset. Fittings were performed in MATLAB for each data set by reducing the root mean square error between the line of best fit and the data set.

An example of the pressure and voltage signals that were fitted after collection through the DAQ board are shown in Figure 6.3. It is clear that even at the frequency shown, 10 Hz, the pressure perturbation from the speaker shows strong linearity and is able to generate a voltage response.

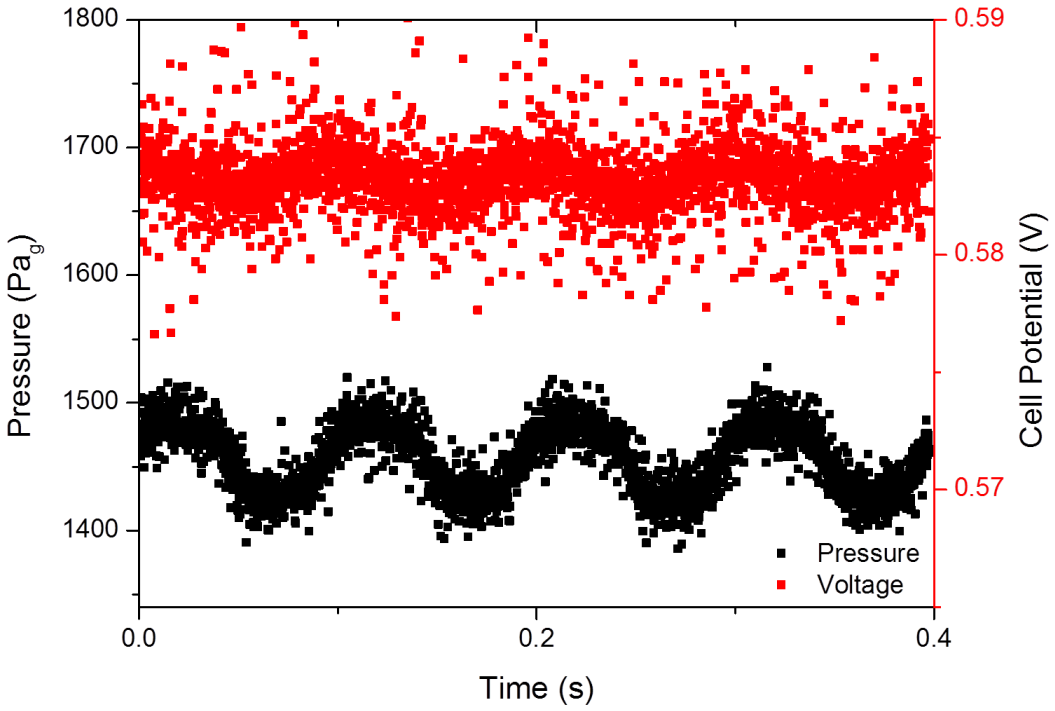

Figure 6.3 - Time-resolved data of EPIS pressure and voltage signal at 10 Hz at 800 mA cm^{-2}. EPIS was performed galvanostatically with a peak amplitude of 60 Pa. The pressure was recorded with a Honeywell PC01D pressure transducer and the pressure and voltage signal were both recorded in an NI- DAQ device.

The amplitude ratio (*AR*) at each frequency is taken as the relative peak amplitude of the voltage response and backpressure perturbation.

$$\mathrm{AR(V\ Pa^{-1}\ )} = \frac{A_V}{A_P}$$

Equation 6.2 – Amplitude ratio of EPIS

The phase shift is the difference in the time offsets between the voltage and the backpressure.

$$\emptyset(\mathrm{degrees}) = (B_V - B_P)\frac{180}{\pi}$$

Equation 6.3 – Phase shift of EPIS

By plotting the amplitude ratio and phase shift as a function of frequency, the EPIS Bode plots for the fuel cell could be generated for varying current densities (Figure 6.4).

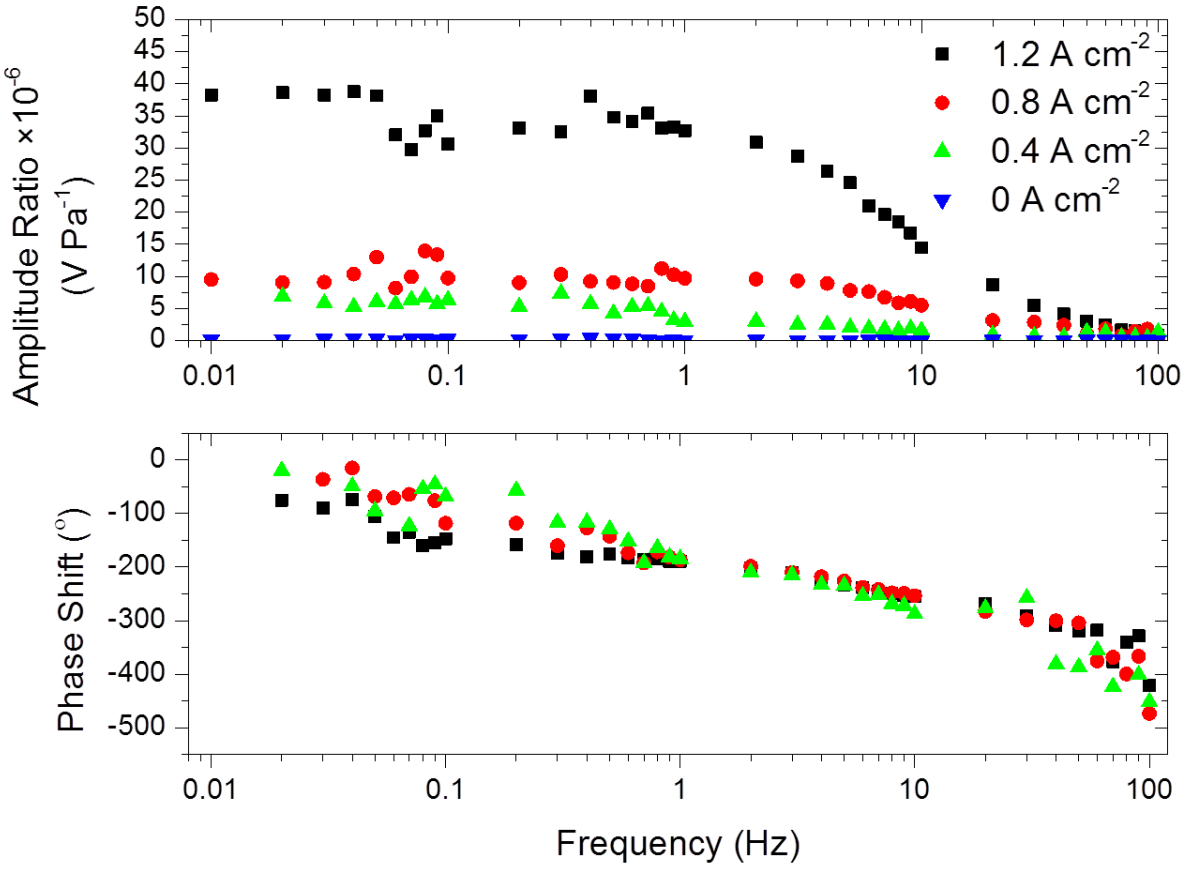

Figure 6.4 – EPIS Bode plots (amplitude ratio – top, and phase shift – bottom) at varying current densities. The plot demonstrates the relationship between the voltage response and pressure stimulus as a function of frequency. The system was perturbed with a 60 Pa peak amplitude pressure stimulus. Both anode and cathode gases were humidified to 70% RH at 100 mL min^{-1} and 250 mL min^{-1}, respectively. The cell was operated galvanostatically with no added backpressure.

At OCV (0 A cm^{-2}) the amplitude ratio is insensitive to modulation frequency and has an average value of 1.5×10^{-7} V Pa^{-1} across the range, consistent with a Nernstian response at 70 °C. The amplitude ratio at each of the other load levels reaches a steady state

maximum value below 100 mHz, which increases with current density. Normalisation of the data in Figure 6.4 shows that at each current density above 0 A cm^{-2}, the characteristic corner frequency, the frequency at which the electrical response begins to reduce relative to the pressure perturbation, does not change. This is indicative of a single phenomenon being observed as the associated time constant in a system does not change with polarisation.

For each polarisation, the response tends to near 0 V Pa^{-1} above 70 Hz. It follows that the effect of pressure modulation is most significant at lower frequencies, associated with processes having a characteristic frequency below ~ 1 s.

It is evident that pressure perturbation has an increasing effect on cell voltage with increasing current density. This is due to pressure having an increased effect on cell performance at higher polarisations and lower stoichiometries, where there are also water management issues, as seen in Figure 6.1. By this interpretation, the amplitude ratio is a measure of the impedance of the reactant gas reaching the active sites on the catalyst surface.

Moreover, the amplitude ratio increases more rapidly below 10 Hz at each current density, with increasing polarisation due to the cell operating nearer the limiting current density; the stoichiometric ratio decreases from greater than 7 at 0.4 A cm^{-2} to 2.5 at 1.2 A cm^{-2}.

Interpretation of phase shift in EPIS varies significantly from that of EIS. This is due to the EPIS phase shift being a strong function of the cell geometry and the location of the pressure oscillation source relative to the cell.

The phase shift does not vary significantly with polarisation and increases with increasing frequency. This can be attributed to the gas volume required for the pressure 'front' to affect the fuel cell voltage. As the frequency increases, the wavelength of each pressure perturbation decreases; thus more than one pressure perturbation may be required before a voltage response is observed in the PEMFC and the phase shift can exceed -360°; given that the distance between the point of pressure measurement and the point at which the pressure 'front' first affects the fuel cell is fixed, the phase shift will tend to negative infinity.

Phase shift data at OCV are not included due to the relatively small amplitudes of the signal providing unreliable phase shift data.

It is important to note that while the net flowrate controlled by the Scribner is constant, the pressure front can cause localised changes in gas velocity, lending the opportunity to model the effect of gas velocity on the electrical response.

6.2.3 EPIS under varying humidity conditions

In order to demonstrate the potential of EPIS to provide new information about PEMFC operation, the effect of different reactant gas humidification conditions was examined. The effects of stoichiometry were normalised by fixing the flow rates and polarisation for each humidity condition. Figure 6.5(a) compares the polarisation curve performance when supplying gases with 70% relative humidity to both electrodes with that using a dry cathode/70% RH anode and a 70% RH cathode/dry anode.

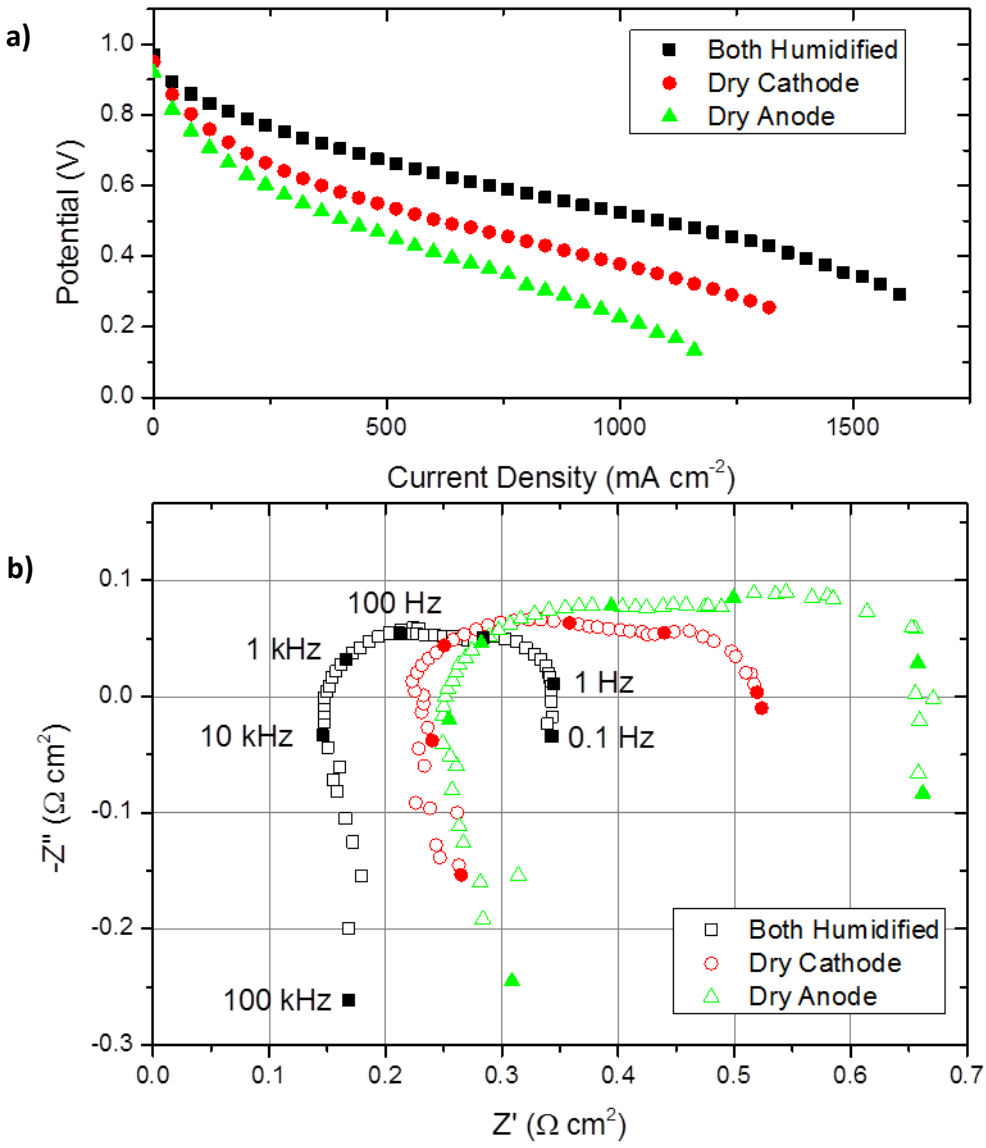

Figure 6.5 – Effects of supplying 70% RH and dried inlet gases on the polarisation curves (a) and EIS Nyquist plots (b). In the case where the anode was dry, the cathode was humidified and vice-versa. Hydrogen gas was supplied at 100 mL min^{-1} to the anode and air supplied at 250 mL min^{-1} to the cathode with no added backpressure. The cell was operated at 70 °C. EIS was performed between 100 kHz and 100 mHz at 800 mA cm^{-2} with a peak amplitude of 20 mA cm^{-2}.

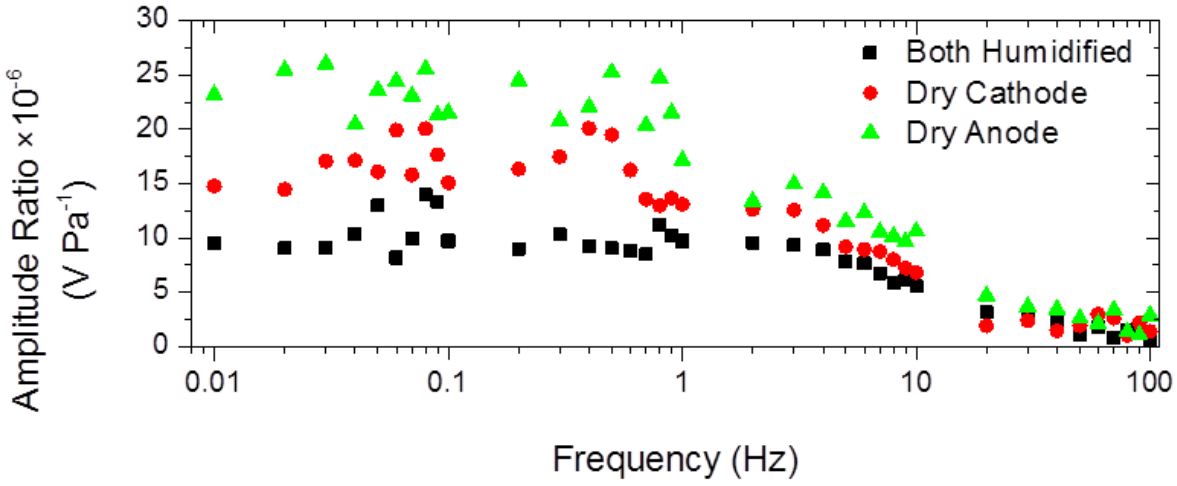

Figure 6.6 - Effects of supplying 70% RH and dried inlet gases on the EPIS *AR*. In the case where the anode was dry, the cathode was humidified and vice-versa. EPIS was performed between 100 Hz and 10 mHz with a peak amplitude of 60 Pa and the cell operated galvanostatically at 800 mA cm^{-2}. Hydrogen gas was supplied at 100 mL min^{-1} to the anode and air supplied at 250 mL min^{-1} to the cathode with no added backpressure.

In accordance with previous studies, there is a significant drop in performance when inlet streams are not humidified [172, 174]. Moreover, fuel cell performance is particularly sensitive to anode humidity as water is generated at the cathode but not at the anode [174].

From the EIS Nyquist plot in Figure 6.5(b), the high-frequency impedance at 800 mA cm^{-2} increases from 150 mΩ cm^2 when both steams are humidified to 220 mΩ cm^2 and 250 mΩ cm^2 when the cathode and anode respectively are supplied with dry gases. Moreover, the low-frequency impedance also increases when dry gases are supplied. This has been previously reported by Kim *et al.* [120] who attributed a higher ionic resistance to the increasing low-frequency impedance.

When considering the EPIS response, it should be noted that the same current density and reactant flow rates were used in each case to eliminate the variables of stoichiometry and oxygen partial pressure in the cathode feed. Figure 6.6 shows that, below 1 Hz, the EPIS amplitude ratio when both inlet streams are humidified is near 10×10^{-6} V Pa^{-1}. This value increases to 15×10^{-6} V Pa^{-1} when the cathode is dry and 25×10^{-6} V Pa^{-1} when the anode is dry. Thus, the larger amplitude ratios observed when the anode or cathode were supplied with dry gas can be attributed to the fact that the humidification and thus water balance of the system is more sensitive compared to having both streams humidified. Furthermore, when comparing EIS to EPIS, it can be observed that below 1 Hz, there is little change in the magnitude of the EPIS response, which corresponds to the low-frequency intercept with the real axis in the EIS. Discounting the difference in the high frequency intercepts, it is observed that the frequency range over which the EIS responses diverge corresponds to ca. 100 Hz to 1 Hz, the same range over which the EPIS responses change and diverge. The two techniques are therefore complementary and can confirm whether the difference in performance is a consequence of water management effects.

6.2.4 EPIS amplitude ratio as a function of stoichiometry

It is clear that stoichiometry has a significant effect on electrical performance due to the amount of reactant available. While stoichiometry was altered in Section 6.2.2, the relationship between the EPIS AR and stoichiometry of inlet gases was not clearly defined and investigated.

The amplitude ratio was investigated at a single frequency, 1 Hz, as this one of the fastest in the low-frequency *AR* plateau shown in Figure 6.4 and Figure 6.5. The relationship between stoichiometry and EPIS amplitude ratio at five current densities is shown in Figure 6.7.

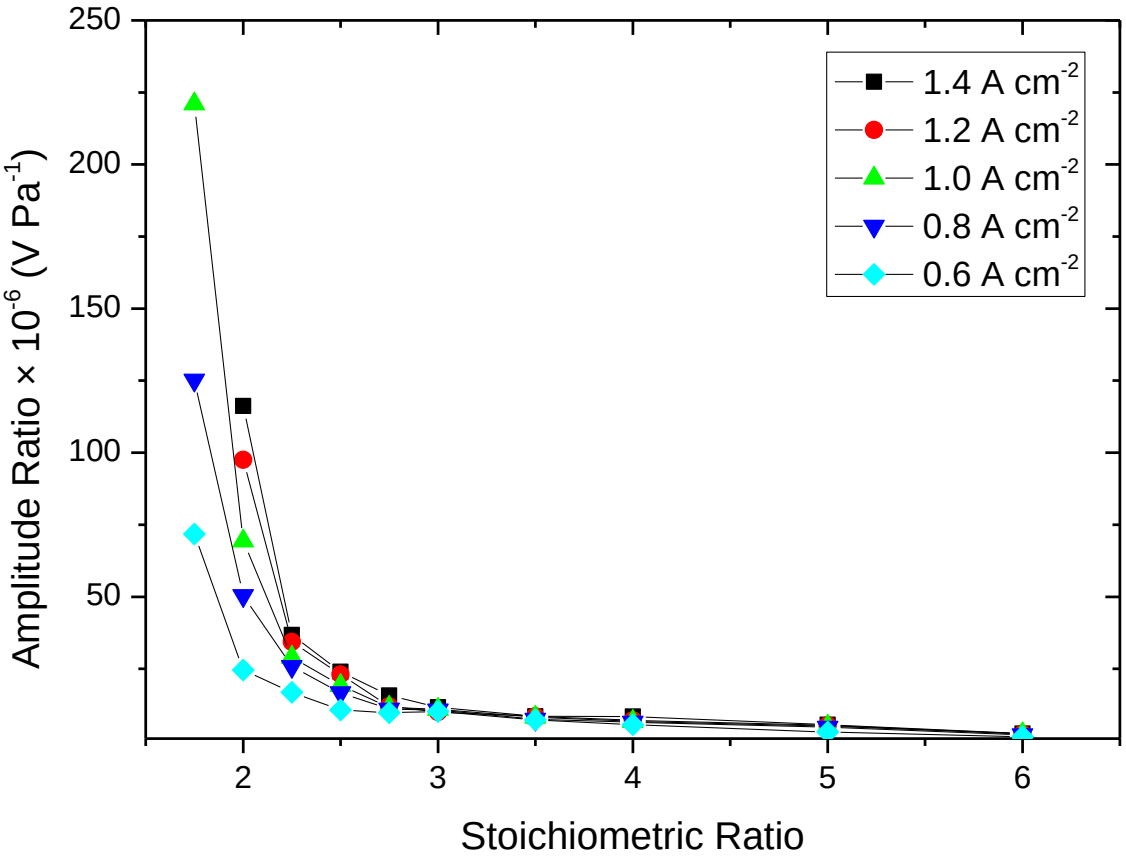

Figure 6.7 – EPIS amplitude ratio at 1 Hz as a function of reactant stoichiometry and current density. The system was perturbed with a 60 Pa peak amplitude pressure stimulus.

It can be observed that there is a convergence in the amplitude ratio with increasing stoichiometry. This is expected as the pressure perturbation has a smaller effect on improvement of oxygen distribution than the actual amount of oxygen available. The convergence occurs near a stoichiometry of 3, which is also the stoichiometric value suggested by the US Department of Energy for standardisation of single cell testing to reduce the effect of reactant utilisation [178].

For current densities above 1.0 A cm^{-2}, it was not possible to achieve a stable, linear voltage response to a pressure perturbation below a stoichiometric ratio of 2.

It can be seen that for any given stoichiometry, there is an increased EPIS AR with increasing current density, indicative that the voltage is more sensitive to pressure perturbations at higher current densities. Because there is more oxidant available at a higher current density at a fixed stoichiometry, this suggests that the increased *AR* is associated with water management, thus isolating these mass-transport limiting effects.

6.3 Conclusions

EPIS has been developed and successfully applied to an operating PEMFC for the first time to determine the frequency dependent relationship between cell voltage and a periodic cathode backpressure perturbation. The amplitude ratio between the voltage response and pressure perturbation increased with increasing polarisation due to the more

significant effects of altering the partial pressure of oxygen and water management issues at higher current densities.

In order to eliminate the effects of reactant partial pressure, the system was investigated under varying inlet gas humidity conditions. The amplitude ratio increases when dry rather than humid gases are supplied to the fuel cell, implying that water imbalances can be indirectly measured using EPIS, providing complementary information to EIS. The difference in phase increases similarly with increasing frequency regardless of polarisation and gas inlet humidity, suggesting this is a function of the geometry of the cell.

The effect of stoichiometry on the EPIS AR was investigated at a single frequency and demonstrated a convergence of AR above a stoichiometric ratio of 3 and *AR* increasing with increasing current density, suggesting the effects of oxidant availability and water management were measured separately.

Chapter 7

Summary, Conclusions and Future Work

While great success was achieved in the development and application of the three transfer function techniques, there remain challenges to monitoring fuel cell performance and improving their viability as a widely commercialised energy conversion device. Alterations to PEMFC systems were made in order to develop the diagnostic techniques, which perhaps would not be accommodated by a commercial system. While standard metrological tools and standards have been recently introduced by the International Electrotechnical Commission [179], these are sure to change with time as progress is made in PEMFC monitoring sensors and systems.

7.1 Summary and Conclusions

The three transfer function diagnostic techniques developed and discussed have offered unique insight into fuel cell performance, providing complementary information to the current understanding of PEMFCs and offering alternative methods of diagnosing fuel cell failure modes.

The localised impedance using reference electrodes has validated the assumption of the cathodic behaviour dominating the overall impedance. More importantly, the study demonstrated the difference in localised cell performance due to the changing conditions down the flow-field of a PEMFC. The transient HF resistance study on start-up also demonstrated a unique method of observing spatially resolved membrane hydration transients, previously only recorded with a complex array of sensitive displacement sensors.

ETIS was applied to an open-cathode PEMFC to investigate the relevant frequency ranges required to yield information about fuel cell performance. Due to the relatively slow diffusion of heat, the technique offered limited information on fuel cell performance other than mass transport limitations associated with water production, which created added thermal impedances to the materials already present in the system. With the application of lock-in thermography, relevant frequencies could be selected to identify pinhole formation and bowing of lands; separating electro-thermal effects from non-electro-thermal effects, not easily accessible by EIS.

EPIS was applied to a PEMFC and shown to be a useful technique in the evaluation of water management and reaction kinetics. The technique could be accurately applied to measure a Nernstian response at OCV and at constant stoichiometry, was able to isolate the effects of the partial pressure of oxidant from water management; demonstrated by the study in Section 6.2.3.

Although vastly different in their system perturbations and measurements, both ETIS and EPIS revealed complementary PEMFC performance data provided by the more conventional EIS. From Figure 7.1, there is clearly an overlap in the frequencies at which ETIS and EPIS spectra overlap with EIS and various physical phenomena that affect fuel cell performance.

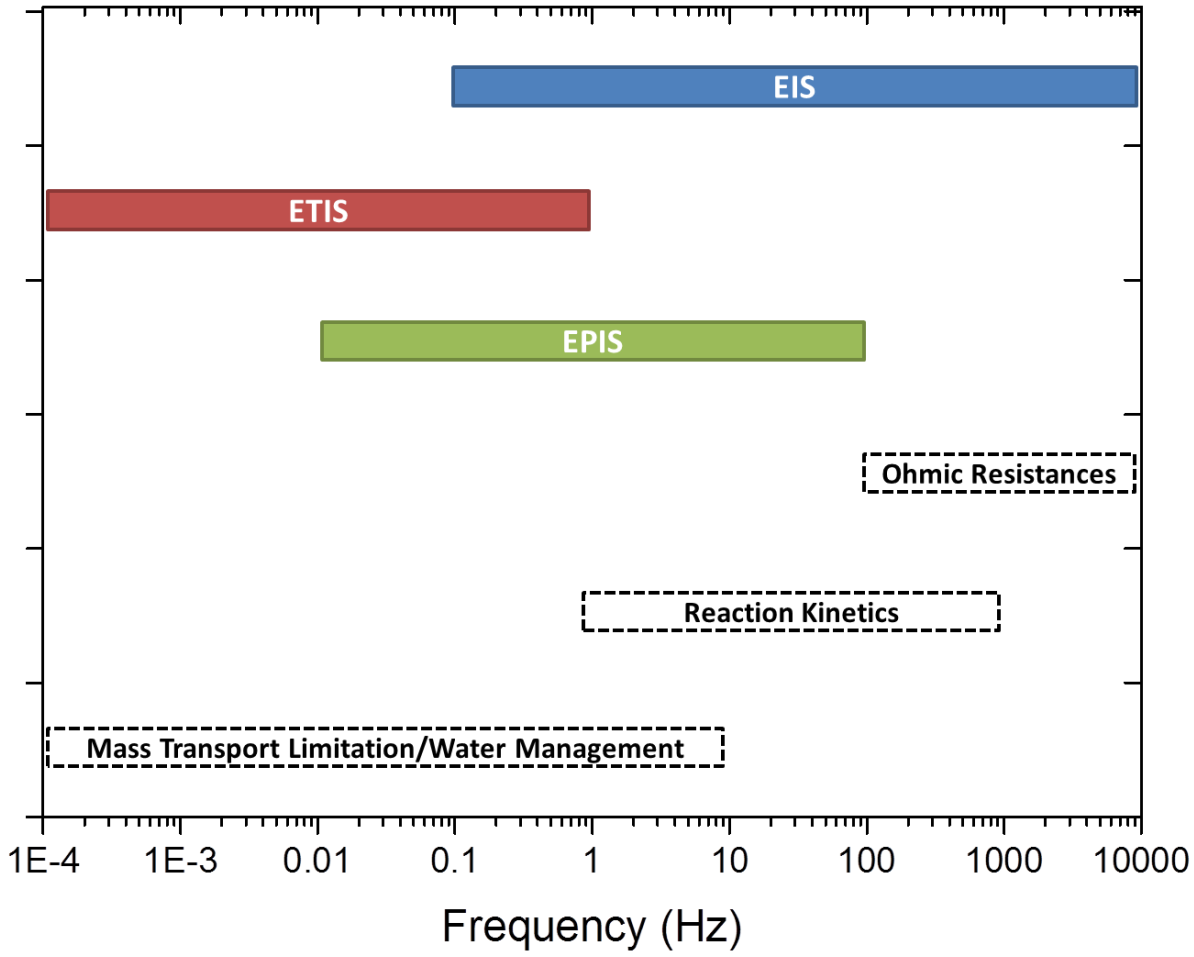

Figure 7.1 – Relevant frequency range of applying EIS, ETIS, and EPIS for a PEMFC presented with relevant fuel cell performance factors accessible by EIS.

From ETIS, the common link was the measurement of water management in varying ways; rather than improving electrical conductivity in the membrane or increasing concentration polarisation, ETIS is applied to measure liquid water formation as an additional thermal impedance, appearing as a lower amplitude ratio in the channels.

From EPIS, reaction kinetics could be perturbed and measured accurately in the form of the Nernstian response at OCV. Moreover, the contribution to water management issues was measured more directly with EPIS as the oxidant partial pressure was perturbed and controlled. There is scope for EPIS to be applied at higher frequencies if the voltage response can be measured locally, rather than at the system level. Due to the high frequency of the pressure perturbation and long serpentine geometry, it is possible that the global oxidant partial pressure at high frequencies is not changing, thus dampening the global voltage response.

7.2 Future Work

While progress has been made in developing and applying these specific techniques, it is important to reflect on the limitations of each study and suggest further areas of interest to improve the efficacy of each diagnostic tool and develop more of the transfer functions shown in Table 2.2.

7.2.1 Localised EIS using a novel reference electrode array

The greatest limitation in making cathode-specific measurements in the study presented in Chapter 4 is the need to drill small holes in the GDL to achieve direct contact between the salt bridge and catalyst layer. This method was shown to affect the overall fuel cell performance at current densities above 1 A cm^{-2}, but there is the likelihood that the system alteration had a greater localised affect near the reference electrode measurement point.

A potential method to overcome this is to use radiation grafting in the specific areas where reference electrode measurements are taken in order create a low resistance ionic pathway through the GDL and MPL to the catalyst layer without compromising the structure of the diffusive layer. This technique was recently been demonstrated by PSI who used the technique to graft membranes for electrolysis applications [180].

Moreover, the ability to incorporate localised voltage measurements through the flow-field plates allows for the implementation of further instrumentation such as relative

humidity sensors and temperature sensors to isolate the effects of water formation and heat production relative to localised cell performance.

The inclusion of thermocouples also yields the possibility of performing ETIS on a closed-cathode system. Localised PEIS may be performed by applying a pressure perturbation at the outlet of the cell and measuring voltage responses at each reference electrode point.

7.2.2 ETIS applied to PEMFCs

ETIS was developed and applied to a passive open-cathode PEMFC to simplify the thermal complexity of the fuel cell system. As previously mentioned, there is the possibility of utilising temperature mapping while applying ETIS to a larger, closed cathode system. Although the spatial resolution would decrease relative to the study presented in Chapter 5, it would be more relevant to high power applications. The application of localised ETIS on a closed system may reveal changes in thermal impedance down the cathode due to the formation of liquid water.

In order to be more applicable to industrial applications, the technique would need to be tuned for PEMFCs with convective fans blowing air over the cathode. This would inevitably introduce a faster time constant than heat conduction, associated with forced convection and dampen thermal responses. Despite this, the use of ETIS may still be relevant due to the high-temperature resolution of IR thermography equipment available. The geometry, orientation, and materials used in the cell should also be considered as

components such as thick end-plates can sufficiently dampen thermal responses due to the large diffusive length and insulation of heat.

7.2.3 EPIS applied to PEMFCs

EPIS was applied to a PEMFC with a serpentine flow-field, increasing the complexity of the pressure signature of the system due to the pressure drop associated with this geometry. As the pressure front moves through the system, the pressure perturbation is dampened as one would expect with any pressure front travelling through a media. Hence, the pressure perturbation at the cathode outlet may not be the same magnitude as that in the centre of the cathode.

Moving to a simpler, straight flow-field geometry would likely yield a greater electrical response as the pressure perturbation would have an effect on more of the active area. This could be useful in evaluating the water management of different GDL materials in a sample volume. However, it will not aid in the application of water management in industrial stacks; where water management issues can be affected by the pressure drop caused by serpentine geometries. It is more representative to apply the technique to a more complex system, knowing the pressure perturbation and voltage response using localised measurements incorporated into the cell design.

Localised measurements will unlock higher EPIS frequencies, allowing for the evaluation of improvements in Ohmic resistance. This may be onset by the changes in membrane

resistance caused by perturbations of the partial pressure of oxygen, resulting in the formation of water and subsequent hydration of electrolyte.

Although EPIS yielded information from the changes in *AR* to the water management of a PEMFC system, the *PS* revealed little information. This was due to the fact that the geometry of the cell and flow rates did not change throughout the study presented in Chapter 6; the characteristic length for the pressure perturbation to affect fuel cell performance did not change.

There is the possibility to examine how the flow is distributed in a fuel cell by examining the localised EPIS phase shift using a segmented current collector or reference electrode array, analogous to localised EIS studies such as that presented in Chapter 4. The measurement of localised pressure due to a fixed perturbation downstream prior or measurement of voltage allows for calibration of the characteristic pressure signal of the PEMFC under different flow conditions.

Furthermore, diffusion of gas to the catalyst surface can be examined by comparing the phase shift of a system using air to one with heliox, a mixture of helium and oxygen, in which diffusion will be an order of magnitude faster [169]. By a similar reasoning, the diffusion of oxidant to the catalyst layer through different gas diffusion and micro-porous layer materials can be examined, quantifying this effect.

References

[1] M. Mench, Fuel Cell Engines, Wiley, New Jersey, 2008.

[2] R.P. O'Hayre, Fuel Cell Fundamentals, Wiley, New Jersey, 2006.

[3] A. Wilson, J. Marcinkoski, D. Papageorgopoulos, Fuel Cell System Cost - 2016, in: D.o. Energy (Ed.), 2016.

[4] J.M. Moore, P.L. Adcock, J.B. Lakeman, G.O. Mepsted, The effects of battlefield contaminants on PEMFC performance, Journal of Power Sources, 85 (2000) 254-260.

[5] O. Baturina, Y. Garsany, B. Gould, K. Swider-Lyons, Contaminant-Induced Degradation, in: PEM Fuel Cell Failure Mode Analysis, CRC Press, 2011, pp. 199-241.

[6] D.J.L. Brett, A.R. Kucernak, P. Aguiar, S.C. Atkins, N.P. Brandon, R. Clague, L.F. Cohen, G. Hinds, C. Kalyvas, G.J. Offer, B. Ladewig, R. Maher, A. Marquis, P. Shearing, N. Vasileiadis, V. Vesovic, What happens inside a fuel cell? Developing an experimental functional map of fuel cell performance., Chem. Phys. Phys. Chem, 11 (2010) 2714 - 2731.

[7] R. Borup, J. Meyers, B. Pivovar, Y.S. Kim, R. Mukudan, N. Garland, D. Myers, M. Wilson, F. Garzon, D. Wood, P. Zelenay, K. More, K. Stroh, T. Zawodzinski, J. Boncella, J.E. McGrath, M. Inaba, K. Miyatake, M. Hori, K. Ota, Z. Ohumi, S. Miyata, A. Nishikata, Z. Siroma, Y. Uchimoto, K. Yasuda, K.-i. Kimijima, N. Iwashita, Scientific Aspects of Polymer Electrolyte Fuel Cell Durability and Degradation, Chem. Rev., 107 (2007) 3904 - 3951.

[8] M. Orazem, B. Tribollet, Electrochemical Impedance Spectroscopy, Wiley, Hoboken, New Jersey, 2008.

[9] G. Hoogers, Fuel Cell Technology Handbook, CRC Press LLC, 2002.

[10] E4Tech, The Fuel Cell Industry Review 2016, in, 2016.

[11] Bloomberg Markets, in, 2017.

[12] O.T. Holton, J.W. Stevenson, The Role of Platinum in Proton Exchange Membrane Fuel Cells, Platinum Metals Review, 57 (2013) 259-271.

[13] J. Zhang, PEM Fuel Cell Electrocatalysts and Catalyst Layers, Springer, 2008.

[14] R.A. Antunes, M.C.L. Oliveira, G. Ett, V. Ett, Corrosion of metal bipolar plates for PEM fuel cells: A review, International Journal of Hydrogen Energy, 35 (2010) 3632-3647.

[15] F. Barbir, PEM Fuel Cells, Elsevier Academic Press, 2005.

[16] X. Wang, R. Kumar, D.J. Myers, Effect of Voltage on Platinum Dissolution: Relevance to Polymer Electrolyte Fuel Cells, Electrochemical and Solid-State Letters, 9 (2006) A225-A227.

[17] M.K. Debe, Electrocatalyst approaches and challenges for automotive fuel cells, Nature, 486 (2012) 43-51.

[18] A.J. Bard, L. Faulkner, Electrochemical Methods Fundamentals and Applications, 2nd ed., Wiley, 2001.

[19] J. Wu, X.Z. Yuan, H. Wang, M. Blanco, J.J. Martin, J. Zhang, Diagnostic tools in PEM fuel cell research: Part I Electrochemical techniques, International Journal of Hydrogen Energy, 33 (2008) 1735-1746.

[20] W.J. Wruck, R.M. Machado, T.W. Chapman, Current Interruption—Instrumentation and Applications, Journal of the Electrochemical Society, 134 (1987) 539-546.

[21] X. Yuan, H. Wang, J. Colin Sun, J. Zhang, AC impedance technique in PEM fuel cell diagnosis—A review, International Journal of Hydrogen Energy, 32 (2007) 4365-4380.

[22] C.E. Reece, An Introduction to Electrochemical Impedance Spectroscopy (EIS), in: 3rd International Workshop on Thin films and New Ideas for pushing the limits of RF Superconductivity, Jefferson Lab, Viriginia, 2008.

[23] X.-Z. Yuan, C. Song, H. Wang, J. Zhang, Electrochemical impedance spectroscopy in PEM fuel cells : fundamentals and applications, Springer, London, 2010.

[24] F. Marken, A. Neudeck, A.M. Bond, Cyclic Voltammetry, in: Electroanalytical Methods, Springer, Berlin, 2010, pp. 57 - 106.

[25] H.A. Gasteiger, W. Gu, R. Makharia, W.F. Mathias, B. Sompali, Fuel Cell Technology and Applications, in: W. Vielstitch, A. Lamm, H.A. Gasteiger (Eds.) Handbook of Fuel Cells: Fundamentals, Technology, Applications, vol. 3, Wiley, New York, 2003, pp. 593.

[26] K.C. Neyerlin, W. Gu, J. Jorne, A. Clark, H.A. Gasteiger, Cathode Catalyst Utilization for the ORR in a PEMFC: Analytical Model and Experimental Validation, Journal of the Electrochemical Society, 154 (2007) B279-B287.

[27] K.C. Neyerlin, W. Gu, J. Jorne, H.A. Gasteiger, Determination of Catalyst Unique Parameters for the Oxygen Reduction Reaction in a PEMFC, Journal of the Electrochemical Society, 153 (2006) A1955-A1963.

[28] A. Pozio, M. De Francesco, A. Cemmi, F. Cardellini, L. Giorgi, Comparison of high surface Pt/C catalysts by cyclic voltammetry, Journal of Power Sources, 105 (2002) 13-19.

[29] K. Kinoshita, P. Stonehart, Preparation and Characterization of Highly Dispersed Electrocatalytic Materials, in: J.O.M. Bockris, B.E. Conway (Eds.) Modern Aspects of Electrochemistry: No. 12, Springer US, Boston, MA, 1977, pp. 183-266.

[30] E. Brightman, G. Hinds, R. O'Malley, In situ measurement of active catalyst surface area in fuel cell stacks, Journal of Power Sources, 242 (2013) 244-254.

[31] K.-S. Lee, B.-S. Lee, S.J. Yoo, S.-K. Kim, S.J. Hwang, H.-J. Kim, E. Cho, D. Henkensmeier, J.W. Yun, S.W. Nam, T.-H. Lim, J.H. Jang, Development of a galvanostatic analysis technique as an in-situ diagnostic tool for PEMFC single cells and stacks, International Journal of Hydrogen Energy, 37 (2012) 5891-5900.

[32] D. Kramer, J. Zhang, R. Shimoi, E. Lehmann, A. Wokaun, K. Shinohara, G.G. Scherer, In situ diagnostic of two-phase flow phenomena in polymer electrolyte fuel cells by neutron imaging: Part A. Experimental, data treatment, and quantification Electrochimica Acta, 50 (2005) 2603-2614.

[33] N. Pekula, K. Heller, P.A. Chuang, A. Turhan, M.M. Mench, J.S. Brenizer, K. Ünlü, Study of water distribution and transport in a polymer electrolyte fuel cell using neutron imaging, Nuclear Instruments and Methods in Physics Research Section A: Accelerators, Spectrometers, Detectors and Associated Equipment, 542 (2005) 134-141.

[34] P. Boillat, D. Kramer, B.C. Seyfang, G. Frei, E. Lehmann, G.G. Scherer, A. Wokaun, Y. Ichikawa, Y. Tasaki, K. Shinohara, In situ observation of the water distribution across a PEFC using high resolution neutron radiography, Electrochemistry Communications, 10 (2008) 546-550.

[35] P. Stahl, J. Biesdorf, P. Boillat, J. Kraft, K.A. Friedrich, Water Distribution Analysis in the Outer Perimeter Region of Technical PEFC Based on Neutron Radiography, Journal of the Electrochemical Society, 162 (2015) F677-F685.

[36] P. Oberholzer, P. Boillat, R. Siegrist, R. Perego, A. Kästner, E. Lehmann, G.G. Scherer, A. Wokaun, Cold-Start of a PEFC Visualized with High Resolution Dynamic In-Plane Neutron Imaging, Journal of the Electrochemical Society, 159 (2011) B235-B245.

[37] Q. Meyer, S. Ashton, R. Jervis, D.P. Finegan, P. Boillat, M. Cochet, O. Curnick, T. Reisch, P. Adcock, P.R. Shearing, D.J.L. Brett, The Hydro-electro-thermal Performance of Air-cooled, Open-cathode Polymer Electrolyte Fuel Cells: Combined Localised Current Density, Temperature and Water Mapping, Electrochimica Acta, 180 (2015) 307-315.

[38] Y.-S. Chen, H. Peng, D.S. Hussey, D.L. Jacobson, D.T. Tran, T. Abdel-Baset, M. Biernacki, Water distribution measurement for a PEMFC through neutron radiography, Journal of Power Sources, 170 (2007) 376-386.

[39] Q. Meyer, S. Ashton, P. Boillat, M. Cochet, E. Engebretsen, D.P. Finegan, X. Lu, J.J. Bailey, N. Mansor, R. Abdulaziz, O.O. Taiwo, R. Jervis, S. Torija, P. Benson, S. Foster, P. Adcock, P.R. Shearing, D.J.L. Brett, Effect of gas diffusion layer properties on water distribution across air-cooled, open-cathode polymer electrolyte fuel cells: A combined ex-situ X-ray tomography and in-operando neutron imaging study, Electrochimica Acta, 211 (2016) 478-487.

[40] Q. Meyer, S. Ashton, S. Torija, C. Gurney, P. Boillat, M. Cochet, E. Engebretsen, D.P. Finegan, P. Adcock, P.R. Shearing, D.J.L. Brett, Nitrogen Blanketing and Hydrogen Starvation in Dead-Ended-Anode Polymer Electrolyte Fuel Cells Revealed by Hydro-Electro-Thermal Analysis, Electrochimica Acta, 203 (2016) 198-205.

[41] K. Tüber, D. Pócza, C. Hebling, Visualization of water buildup in the cathode of a transparent PEM fuel cell, Journal of Power Sources, 124 (2003) 403-414.

[42] D. Spernjak, A.K. Prasad, S.G. Advani, Experimental investigation of liquid water formation and transport in a transparent single-serpentine PEM fuel cell, Journal of Power Sources, 170 (2007) 334-344.

[43] D. Spernjak, S.G. Advani, A.K. Prasad, Simultaneous Neutron and Optical Imaging in PEM Fuel Cells, Journal of the Electrochemical Society, 156 (2009) B109-B117.

[44] S.-K. Lee, K. Ito, T. Ohshima, S. Noda, K. Sasaki, In Situ Measurement of Temperature Distribution across a Proton Exchange Membrane Fuel Cell, Electrochemical and Solid-State Letters, 12 (2009) B126-B130.

[45] H. Lin, T.-F. Cao, L. Chen, Y.-L. He, W.-Q. Tao, In situ measurement of temperature distribution within a single polymer electrolyte membrane fuel cell, International Journal of Hydrogen Energy, 37 (2012) 11871-11886.

[46] H. Pei, Z. Liu, H. Zhang, Y. Yu, Z. Tu, Z. Wan, W. Liu, In situ measurement of temperature distribution in proton exchange membrane fuel cell I a hydrogen–air stack, Journal of Power Sources, 227 (2013) 72-79.

[47] Z. Wan, J. Shen, H. Zhang, Z. Tu, W. Liu, In situ temperature measurement in a 5kW-class Proton Exchange Membrane Fuel Cell stack with pure oxygen as the oxidant, International Journal of Heat and Mass Transfer, 75 (2014) 231-234.

[48] Q. Meyer, K. Ronaszegi, J.B. Robinson, M. Noorkami, O. Curnick, S. Ashton, A. Danelyan, T. Reisch, P. Adcock, R. Kraume, P.R. Shearing, D.J.L. Brett, Combined current and temperature mapping in an air-cooled, open-cathode polymer electrolyte fuel cell under steady-state and dynamic conditions, Journal of Power Sources, 297 (2015) 315-322.

[49] M. Vollmer, L.-P. Möllmann, Infrared Thermal Imaging: Fundamentals, Research and Applications, Wiley-VCH, 2010.

[50] O. Breitenstein, W. Warta, M. Langenkamp, Lock-in Thermography: Basics and Use for Evaluating Electronic Devices and Materials, 2 ed. ed., Springer, 2003.

[51] Y.A. Cengel, Heat Transfer: A Practical Approach, McGraw-Hill Higher Education, 2002.

[52] A. Hakenjos, H. Muenter, U. Wittstadt, C. Hebling, A PEM fuel cell for combined measurement of current and temperature distribution, and flow field flooding, J. Power Sources, 131 (2004) 213 - 216.

[53] M. Wang, H. Guo, C. Ma, Temperature distribution on the MEA surface of a PEMFC with serpentine channel flow bed, J. Power Sources, 17 (2006) 181-187.

[54] Q. Meyer, S. Shton, O. Curnick, T. Reisch, P. Adcock, K. Ronaszegi, J.B. Robinson, D.J.L. Brett, Dead-ended anode polymer electrolyte fuel cell stack operation investigatation using electrochemical impedance spectroscopy, J. Power Sources, 254 (2014) 1-9.

[55] M. Matian, A.J. Marquis, N.P. Brandon, Application of thermal imaging to calidate a heat transfer model for polymer electrolyte fuel cells, Int. J. Hydrogen Energy, 35 (2010) 12308 -12316.

[56] L.S. Martins, J.E.F.C. Gardolinski, J.V.C. Vargas, J.C. Ordonez, S.C. Amico, M.M.C. Forte, The experimental validation of a simplified PEMFC simulation model for design and optimization purposes, Applied Thermal Eng., 29 (2009) 3036-3048.

[57] G.N. Srinivasulu, T. Subrahmanyam, V.D. Rao, Parametric sensitivity analysis of PEM fuel cell electrochemical Model, International Journal of Hydrogen Energy, 36 (2011) 14838-14844.

[58] M. Noorkami, J.B. Robinson, Q. Meyer, O.A. Obeisun, E.S. Fraga, T. Reisch, P.R. Shearing, D.J.L. Brett, Effect of temperature uncertainty on polymer electrolyte fuel cell performance, Int. J. Hydrogen Energy, 39 (2014) 1439-1448.

[59] K.J. Åström, R.M. Murray, Analysis and Design of Feedback Systems, Princeton University Press, 2008.

[60] S. Webb, T. Croft, L. Mustoe, J. Ward, Engineering Mathematics Open Learning Project, in, vol. 2014, Loughborough University, 1999.

[61] J.P. Diard, B.L. Gorrec, C. Montella, Handbook of Electrochemical Impedance Spectroscopy, in: Bio-Logic (Ed.), Claix, France, 2013.

[62] D.E. Seborg, D.A. Mellichamp, T.F. Edgar, F.J. Doyle, Process Dynamics and Control, John Wiley & Sons, 2010.

[63] A. Lasia, Electrochemical Impedance Spectroscopy and its Applications, in: Modern Aspects of Electrochemistry, Springer, 2002.

[64] G. Stephanapoulos, Chemical Process Control: An Introduction to Theory and Practice, Prentice-Hall, 1984.

[65] N. Wagner, Characterization of membrane electrode assemblies in polymer electrolyte fuel cells using a.c. impedance spectroscopy, Journal of Applied Electrochemistry, 32 (2002) 859-863.

[66] M. Boillot, C. Bonnet, S. Didierjean, F. Lapicque, Investigation of the response of separate electrodes in a polymer electrolyte membrane fuel cell without reference electrode, Journal of Applied Electrochemistry, 37 (2007) 103-110.

[67] V.A. Paganin, C.L.F. Oliveira, E.A. Ticianelli, T.E. Springer, E.R. Gonzalez, Modelisticinterpretation of the impedance response of a polymer electrolyte fuel cell1, Electrochimica Acta, 43 (1998) 3761-3766.

[68] E. Antolini, L. Giorgi, A. Pozio, E. Passalacqua, Influence of Nafion loading in the catalyst layer of gas-diffusion electrodes for PEFC, Journal of Power Sources, 77 (1999) 136-142.

[69] T.J.P. Freire, E.R. Gonzalez, Effect of membrane characteristics and humidification conditions on the impedance response of polymer electrolyte fuel cells, Journal of Electroanalytical Chemistry, 503 (2001) 57-68.

[70] L.R. Jordan, A.K. Shukla, T. Behrsing, N.R. Avery, B.C. Muddle, M. Forsyth, Diffusion layer parameters influencing optimal fuel cell performance, Journal of Power Sources, 86 (2000) 250-254.

[71] E. Passalacqua, G. Squadrito, F. Lufrano, A. Patti, L. Giorgi, Effects of the Diffusion Layer Characteristics on the Performance of Polymer Electrolyte Fuel Cell Electrodes, Journal of Applied Electrochemistry, 31 (2001) 449-454.

[72] D.M. Bernardi, M.W. Verbrugge, A Mathematical Model of the Solid-Polymer-Electrolyte Fuel Cell, Journal of the Electrochemical Society, 139 (1992) 2477-2491.

[73] T.J. Mason, J. Millichamp, T.P. Neville, A. El-kharouf, B.G. Pollet, D.J.L. Brett, Effect of clamping pressure on ohmic resistance and compression of gas diffusion layers for polymer electrolyte fuel cells, Journal of Power Sources, 219 (2012) 52-59.

[74] T.J. Mason, J. Millichamp, T.P. Neville, P.R. Shearing, S. Simons, D.J.L. Brett, A study of the effect of water management and electrode flooding on the dimensional change of polymer electrolyte fuel cells, Journal of Power Sources, 242 (2013) 70-77.

[75] N. Wagner, E. Gülzow, Change of electrochemical impedance spectra (EIS) with time during CO-poisoning of the Pt-anode in a membrane fuel cell, Journal of Power Sources, 127 (2004) 341-347.

[76] J.-F. Chailan, M. Khadhraoui, P. Knauth, Mechanical and Dynamic Mechanical Analysis of Proton-Conducting Polymers, in: Solid State Proton Conductors, John Wiley & Sons, Ltd, 2012, pp. 185-240.

[77] Z. Liu, J.S. Wainright, W. Huang, R.F. Savinell, Positioning the reference electrode in proton exchange membrane fuel cells: calculations of primary and secondary current distribution, Electrochimica Acta, 49 (2004) 923-935.

[78] A.A. Kulikovsky, P. Berg, Positioning of a Reference Electrode in a PEM Fuel Cell, Journal of the Electrochemical Society, 162 (2015) F843-F848.

[79] W. He, T. Van Nguyen, Edge Effects on Reference Electrode Measurements in PEM Fuel Cells, Journal of the Electrochemical Society, 151 (2004) A185-A195.

[80] F.N. Büchi, G.G. Scherer Investigation of the Transversal Water Profile in Nafion Membranes in Polymer Electrolyte Fuel Cells, Journal of the Electrochemical Society, 148 (2001) A183-A188.

[81] G. Li, P.G. Pickup, Measurement of single electrode potentials and impedances in hydrogen and direct methanol PEM fuel cells, Electrochimica Acta, 49 (2004) 4119-4126.

[82] P. Piela, T.E. Springer, J. Davey, P. Zelenay, Direct Measurement of iR-Free Individual-Electrode Overpotentials in Polymer Electrolyte Fuel Cells, The Journal of Physical Chemistry C, 111 (2007) 6512-6523.

[83] E. Brightman, G. Hinds, In situ mapping of potential transients during start-up and shut-down of a polymer electrolyte membrane fuel cell, Journal of Power Sources, 267 (2014) 160-170.

[84] G. Hinds, E. Brightman, In situ mapping of electrode potential in a PEM fuel cell, Electrochemistry Communications, 17 (2012) 26-29.

[85] M. Balabajew, B. Roling, Minimizing Artifacts in Three-electrode Double Layer Capacitance Measurements Caused by Stray Capacitances, Electrochimica Acta.

[86] F. Mansfeld, S. Lin, Y.C. Chen, H. Shih, Minimization of High-Frequency Phase Shifts in Impedance Measurements, Journal of the Electrochemical Society, 135 (1988) 906-907.

[87] Q. Meyer, S. Barass, O. Curnick, T. Reisch, D.J.L. Brett, A multichannel frequency response analyser for impedance spectroscopy on power sources, J. Electrochem. Sci. Eng., 3 (2013) 107-114.

[88] O.A. Obeisun, Q. Meyer, J. Robinson, C.W. Gibbs, A.R. Kucernak, P.R. Shearing, D.J.L. Brett, Development of open-cathode polymer electrolyte fuel cells using printed circuit board flow-field plates: Flow geometry characterisation, International Journal of Hydrogen Energy, 39 (2014) 18326-18336.

[89] O.A. Obeisun, Q.P.-G. Meyer, J. Robinson, C. Gibbs, A.R.J. Kucernak, P.R. Shearing, D.J.L. Brett, Advanced Diagnostics Applied to a Self-Breathing Fuel Cell, ECS Transactions, 61 (2014) 249-258.

[90] F.A. Daniels, C. Attingre, A.R. Kucernak, D.J.L. Brett, Current collector design for closed-plenum polymer electrolyte membrane fuel cells, Journal of Power Sources, 249 (2014) 247-262.

[91] O.A. Obeisun, Q. Meyer, E. Engebretsen, D.P. Finegan, J.B. Robinson, G. Hinds, P.R. Shearing, D.J.L. Brett, Study of water accumulation dynamics in the channels of an open-cathode fuel cell through electro-thermal characterisation and droplet visualisation, International Journal of Hydrogen Energy, 40 (2015) 16786-16796.

[92] O.A. Obeisun, D.P. Finegan, E. Engebretsen, J.B. Robinson, O.O. Taiwo, G. Hinds, P.R. Shearing, D.J.L. Brett, Ex-situ characterisation of water droplet dynamics on the surface of

a fuel cell gas diffusion layer through wettability analysis and thermal characterisation, International Journal of Hydrogen Energy, 42 (2017) 4404-4414.

[93] J. Blauert, N. Xiang, Acoustics for Engineers, Springer-Verlag, Berlin, 2008.

[94] A. Storck, F. Coeuret, Mass and momentum transfer at a wall in the presence of turbulence promoters, Electrochimica Acta, 22 (1977) 1155-1160.

[95] C.J. Brown, D. Pletcher, F.C. Walsh, J.K. Hammond, D. Robinson, Local mass transport effects in the FM01 laboratory electrolyser, Journal of Applied Electrochemistry, 22 (1992) 613-619.

[96] L.R. Czarnetzki, L.J.J. Janssen, Electrode current distribution in a hypochlorite cell, Journal of Applied Electrochemistry, 19 (1989) 630-636.

[97] W.W. Focke, On the mechanism of transfer enhancement by eddy promoters, Electrochimica Acta, 28 (1983) 1137-1146.

[98] C. Wieser, A. Helmbold, E. Gülzow, A new technique for two-dimensional current distribution measurements in electrochemical cells, Journal of Applied Electrochemistry, 30 (2000) 803-807.

[99] S.J.C. Cleghorn, C.R. Derouin, M.S. Wilson, S. Gottesfeld, A printed circuit board approach to measuring current distribution in a fuel cell, Journal of Applied Electrochemistry, 28 (1998) 663-672.

[100] M. Noponen, T. Mennola, M. Mikkola, T. Hottinen, P. Lund, Measurement of current distribution in a free-breathing PEMFC, Journal of Power Sources, 106 (2002) 304-312.

[101] S.-G. Kim, M.-J. Kim, Y.-J. Sohn, Segmented cell approach for studying uniformity of current distribution in polymer electrolyte fuel cell operation, International Journal of Hydrogen Energy.

[102] J. St-Pierre, J. Ge, Y. Zhai, T.V. Reshetenko, M. Angelo, PEMFC Cathode Contamination Mechanisms for Several VOCs - Acetonitrile, Acetylene, Bromomethane, Iso-Propanol, Methyl Methacrylate, Naphthalene and Propene, ECS Transactions, 58 (2013) 519-528.

[103] T.V. Reshetenko, J. St-Pierre, Study of the acetonitrile poisoning of platinum cathodes on proton exchange membrane fuel cell spatial performance using a segmented cell system, Journal of Power Sources, 293 (2015) 929-940.

[104] T.V. Reshetenko, J. St-Pierre, Study of acetylene poisoning of Pt cathode on proton exchange membrane fuel cell spatial performance using a segmented cell system, Journal of Power Sources, 287 (2015) 401-415.

[105] T.V. Reshetenko, K. Bethune, M.A. Rubio, R. Rocheleau, Study of low concentration CO poisoning of Pt anode in a proton exchange membrane fuel cell using spatial electrochemical impedance spectroscopy, Journal of Power Sources, 269 (2014) 344-362.

[106] T.V. Reshetenko, K. Bethune, R. Rocheleau, Spatial proton exchange membrane fuel cell performance under carbon monoxide poisoning at a low concentration using a segmented cell system, Journal of Power Sources, 218 (2012) 412-423.

[107] T.V. Reshetenko, G. Bender, K. Bethune, R. Rocheleau, A segmented cell approach for studying the effects of serpentine flow field parameters on PEMFC current distribution, Electrochimica Acta, 88 (2013) 571-579.

[108] T.V. Reshetenko, G. Bender, K. Bethune, R. Rocheleau, Systematic study of back pressure and anode stoichiometry effects on spatial PEMFC performance distribution, Electrochimica Acta, 56 (2011) 8700-8710.

[109] D.J.L. Brett, S. Atkins, N.P. Brandon, V. Vesovic, N. Vasileiadis, A.R. Kucernak, Measurement of the current distribution along a single flow channel of a solid polymer fuel cell, Electrochemistry Communications, 3 (2001) 628-632.

[110] D.J.L. Brett, S. Atkins, N.P. Brandon, V. Vesovic, N. Vasileiadis, A. Kucernak, Localized Impedance Measurements along a Single Channel of a Solid Polymer Fuel Cell, Electrochemical and Solid-State Letters, 6 (2003) A63-A66.

[111] I.A. Schneider, H. Kuhn, A. Wokaun, G.G. Scherer, Fast Locally Resolved Electrochemical Impedance Spectroscopy in Polymer Electrolyte Fuel Cells, Journal of the Electrochemical Society, 152 (2005) A2092-A2103.

[112] A. Hakenjos, C. Hebling, Spatially resolved measurement of PEM fuel cells, Journal of Power Sources, 145 (2005) 307-311.

[113] G. Bender, M.S. Wilson, T.A. Zawodzinski, Further refinements in the segmented cell approach to diagnosing performance in polymer electrolyte fuel cells, Journal of Power Sources, 123 (2003) 163-171.

[114] S. Cruz-Manzo, R. Chen, P. Rama, Study of current distribution and oxygen diffusion in the fuel cell cathode catalyst layer through electrochemical impedance spectroscopy, International Journal of Hydrogen Energy, 38 (2013) 1702-1713.

[115] S. Cruz-Manzo, R. Chen, A generic electrical circuit for performance analysis of the fuel cell cathode catalyst layer through electrochemical impedance spectroscopy, Journal of Electroanalytical Chemistry, 694 (2013) 45-55.

[116] S. Cruz-Manzo, R. Chen, Electrochemical impedance study on estimating the mass transport resistance in the polymer electrolyte fuel cell cathode catalyst layer, Journal of Electroanalytical Chemistry, 702 (2013) 45-48.

[117] A.A. Kulikovsky, M. Eikerling, Analytical solutions for impedance of the cathode catalyst layer in PEM fuel cell: Layer parameters from impedance spectrum without fitting, Journal of Electroanalytical Chemistry, 691 (2013) 13-17.

[118] A. Kulikovsky, O. Shamardina, A Model for PEM Fuel Cell Impedance: Oxygen Flow in the Channel Triggers Spatial and Frequency Oscillations of the Local Impedance, Journal of the Electrochemical Society, 162 (2015) F1068-F1077.

[119] D.J.L. Brett, S. Atkins, N.P. Brandon, N. Vasileiadis, V. Vesovic, A.R. Kucernak, Membrane resistance and current distribution measurements under various operating conditions in a polymer electrolyte fuel cell, Journal of Power Sources, 172 (2007) 2-13.

[120] H.-T. Kim, K.-Y. Song, T.V. Reshetenko, S.-I. Han, T.-Y. Kim, S.-Y. Cho, M.-K. Min, G.-S. Chai, S.-C. Shin, Electrochemical analysis of polymer electrolyte membrane fuel cell operated with dry-air feed, Journal of Power Sources, 193 (2009) 515-522.

[121] Y.-H. Lai, G.W. Fly, S. Clapham, In-situ membrane hydration measurement of proton exchange membrane fuel cells, Journal of Power Sources, 274 (2015) 324-337.

[122] E. Engebretsen, J.B. Robinson, O. Obeisun, T. Mason, D. Finegan, G. Hinds, P.R. Shearing, D.J.L. Brett, Electro-thermal impedance spectroscopy applied to an open-cathode polymer electrolyte fuel cell, Journal of Power Sources, 302 (2016) 210-214.

[123] S.U. Jeong, E.A. Cho, H.J. Kim, T.H. Lim, I.H. Oh, S.H. Kim, Effects of cathode open area and relative humidity on the performance of air-breathing polymer electrolyte membrane fuel cells, J. Power Sources, 158 (2006) 348-353.

[124] N. Bussayajarn, H. Ming, K.K. Hoong, W.Y.M. Stephen, C.S. Hwa, Planar air breathing PEMFC with self-humidifying MEA and open cathode geometry design for portable applications, Int. J. Hydrogen Energy, 34 (2009) 7761-7767.

[125] A. Schmitz, M. Tranitz, S. Wagner, R. Hahn, C. Hebling, Planar self-breathing fuel cells, J. Power Sources, 118 (2003) 162-171.

[126] C. Ziegler, A. Schmitz, M. Tranitz, E. Fontes, J.O. Schumacher, Modeling Planar and Self-Breathing Fuel Cells for Use in Electronic Devices, J. Electrochemical Soc., 151 (2004).

[127] J.P. Schmidt, D. Manka, D. Klotz, E. Ivers-Tiffée, Investigation of the thermal properties of a Li-ion pouch-cell by electrothermal impedance spectroscopy, Journal of Power Sources, 196 (2011) 8140-8146.

[128] E. Barsoukov, J.H. Jang, H. Lee, Thermal impedance spectroscopy for Li-ion batteries using heat-pulse response analysis, Journal of Power Sources, 109 (2002) 313-320.

[129] E. Barsoukov, J.R. Macdonald, Impedance Spectroscopy: Theory, Experiment, and Applications, 2nd ed., Wiley, 2005.

[130] M. Fleckenstein, S. Fischer, O. Bohlen, B. Bäker, Thermal Impedance Spectroscopy - A method for the thermal characterization of high power battery cells, Journal of Power Sources, 223 (2013) 259-267.

[131] S. Huth, O. Breitenstein, A. Huber, D. Dantz, U. Lambert, F. Altmann, Lock-In IR-Thermography – A Novel Tool for Material and Device Characterization, Solid State Phenomena, 82-84 (2001) 741-746.

[132] J.B. Robinson, E. Engebretsen, D. Finegan, J.A. Darr, G. Hinds, P.R. Shearing, D.J.L. Brett, Detection of internal defects in lithium ion batteries using lock-in thermography, ECS Electrochemistry Letters, 4 (2015) A106-A109.

[133] S. Rißland, O. Breitenstein, High resolution saturation current density imaging at grain boundaries by lock-in thermography, Solar Energy Materials and Solar Cells, 104 (2012) 121-124.

[134] S. Besold, U. Hoyer, J. Bachmann, T. Swonke, P. Schilinsky, R. Steim, C.J. Brabec, Quantitative imaging of shunts in organic photovoltaic modules using lock-in thermography, Solar Energy Materials and Solar Cells, 124 (2014) 133-137.

[135] J.P. Rakotoniaina, O. Breitenstein, M. Langenkamp, Localization of weak heat sources in electronic devices using highly sensitive lock-in thermography, Materials Science and Engineering: B, 91–92 (2002) 481-485.

[136] Y.-K. An, J. Yang, S. Hwang, H. Sohn, Line laser lock-in thermography for instantaneous imaging of cracks in semiconductor chips, Optics and Lasers in Engineering, 73 (2015) 128-136.

[137] J.B. Robinson, L.D. Brown, R. Jervis, O.O. Taiwo, T.M.M. Heenan, J. Millichamp, T.J. Mason, T.P. Neville, R. Clague, D.S. Eastwood, C. Reinhard, P.D. Lee, D.J.L. Brett, P.R. Shearing, Investigating the effect of thermal gradients on stress in solid oxide fuel cell anodes using combined synchrotron radiation and thermal imaging, Journal of Power Sources, 288 (2015) 473-481.

[138] S. Zhang, X. Yuan, H. Wang, W. Mérida, H. Zhu, J. Shen, S. Wu, J. Zhang, A review of accelerated stress tests of MEA durability in PEM fuel cells, Int. J. Hydrogen Energy, 34 (2009) 388 - 404.

[139] J. Wu, X.Z. Yuan, J.J. Martin, H. Wang, J. Zhang, J. Shen, S. Wu, W. Merida, A review of PEM fuel cell durability: Degradation mechanisms and mitigation strategies, J. Power Sources, 185 (2008) 104-119.

[140] V. Stanic, M. Hoberecht, Mechanism of Pinhole Formation in Membrane Electrode Assemblies for PEM Fuel Cells, in: M. Murthy, K. Ota, J.W.V. Zee, S.R. Narayanan, E.S.

Takeuchi (Eds.) Proton Conducting Membrane Fuel Cells IV, The Electrochemical Society, Inc.`, Pennington, NJ, 2006, pp. 391 - 401.

[141] S. Vengatesan, M.W. Fowler, X.-Z. Yuan, H. Wang, Diagnosis of MEA degradation under accelerated relative humidity cycling, J. Power Sources, 196 (2011) 5045 - 5052.

[142] C. Lim, L. Ghassemzadeh, F.V. Hove, M. Lauritzen, J. Kolodziej, G.G. Wang, S. Holdcroft, E. Kjeang, Membrane degradation during combined chemical and mechanical accelerated stress testing of PEM fuel cells, J. Power Sources, (2014).

[143] M. Inaba, T. Kinumoto, M. Kiriake, R. Umebayashi, A. Tasaka, Z. Ogumi, Gas crossover and membrane degradation in polymer electrolyte fuel cells, Electrochimica Acta, 51 (2006) 5746 - 5753.

[144] K. Panha, M. Fowler, X.-Z. Yuan, H. Wang, Accelerated durability testing via reactants relative humidity cycling on PEM fuel cells, Applied Energy, 93 (2012) 90 - 97.

[145] T.-C. Jao, G.-B. Jung, S.-T. Ke, P.-H. Chi, S.-H. Chan, Diagnosis of PTFE-Nafion MEA degradation modes by an accelerated degradation technique, Int. J. Energy Res., 35 (2010) 1274 - 1283.

[146] A.B. LaConti, A.R. Fragala, J.R. Boyack, in: D.E. McIntyre, S. Srinivasan, F.G. Will (Eds.) Proceeding of the Symposium on Electrode Materials and Process for Energy Conservation and Storage, The Electrochemical Society, Inc., Princeton, NJ, 1977, pp. 354.

[147] C. Huang, K.S. Tan, J. Lin, K.L. Tan, Chem. Phys. Lett., 371 (2003) 80-85.

[148] A. Pozio, R.F. Silva, M.D. Francesco, L. Giorgi, Nafion degradation in PEFCs from end plate iron contamination, Electrochimica Acta, 48 (2003) 1543-1549.

[149] S. Stucki, G.G. Scherer, S. Schlagowski, E. Fischer, PEM water electrolysers: Evidence for membrane failure in 100kW demonstration plants, J. Appl. Electrochem., 28 (1998) 1041-1049.

[150] J. Yu, B. Yi, D. Zing, F. Liu, Z. Shao, Y. Fu, H. Zhang, Degradation mechanism of polystyrene sulfonic acid membrane and application of its composite membranes in fuel cells Phys. Chem. Chem. Phys., 5 (2002) 611-615.

[151] B. Mattsson, H. Ericson, L.M. Torella, F. Sundholm, Degradation of a fuel cell membrane, as revealed by

micro-Raman spectroscopy, Electrochimica Acta, 45 (2000) 1405-1408.

[152] C.A. Wilkie, J.R. Thomsen, M.L. Mittleman, Interaction of Poly (Methyl Methacrylate) and Nafions, J. of App. Polymer Sci., 42 (1991) 901 - 909.

[153] J. Surowiec, R. Bogoczek, Studies on the thermal stability of the prefluorinated cation-exchange membrane Nafion-417, J. Therm. Anal., 33 (1988) 1097 - 1102.

[154] W. Lü, Z. Liu, C. Wang, Z. Mao, M. Zhang, The effects of pinholes on proton exchange membrane fuel cell performance, Int. J. Energy Res., 35 (2010) 24 - 30.

[155] B.T. Huang, Y. Chatillon, C. Bonnet, F. Lapicque, S. Leclerc, M. Hinaje, S. Raël, Experimental investigation of pinhole effect on MEA/cell aging in PEMFC, Int. J. Hydrogen Energy, 38 (2013) 543 - 550.

[156] R. Lin, E. Gülzow, M. Schulze, K.A. Friedrich, Investigation of Membrane Pinhole Effects in Polymer Electrolyte Fuel Cells by Locally Resolved Current Density, Journal of the Electrochemical Society, 158 (2011) B11-B17.

[157] T.V. Reshetenko, G. Bender, K. Bethune, R. Rocheleau, Application of a segmented cell setup to detect pinhole and catalyst loading defects in proton exchange membrane fuel cells, Electrochimica Acta, 76 (2012) 16-25.

[158] Y.A. Cengel, Heat & Mass Transfer: A Practical Approach, McGraw-Hill Education (India) Pvt Limited, 2007.

[159] J. M. Coulson, J.F. Richardson, Heat Transfer, in: Coulson and Richardson's Chemical Enginnering, vol. 1, Butterworth-Heinemann, Oxford, 2004.

[160] F. Sarvar, N.J. Poole, P.A. Witting, PCB glass-fibre laminates: Thermal conductivity measurements and their effect on simulation, Journal of Electronic Materials, 19 (1990) 1345-1350.

[161] Thermal Properties of Metals, Conductivity, Thermal Expansion, Specific Heat, in: Engineers Edge, vol. 2017, Engineers Edge, LLC, Georgia, USA, 2017.

[162] Fuel Cell Store, in, vol. 2017, Texas, USA, 2017.

[163] P. Gode, F. Jaouen, G. Lindbergh, A. Lundblad, G. Sundholm, Influence of the composition on the structure and electrochemical characteristics of the PEFC cathode, Electrochimica Acta, 48 (2003) 4175-4187.

[164] F. Jaouen, G. Lindbergh, K. Wiezell Transient Techniques for Investigating Mass-Transport Limitations in Gas Diffusion Electrodes: II. Experimental Characterization of the PEFC Cathode, Journal of the Electrochemical Society, 150 (2003) A1711-A1717.

[165] T.L. Williams, Thermal Imaging Cameras: Characteristics and Performance, CRC Press, Boca Raton, 2009.

[166] E. Engebretsen, T.J. Mason, P.R. Shearing, G. Hinds, D.J.L. Brett, Electrochemical pressure impedance spectroscopy applied to the study of polymer electrolyte fuel cells, Electrochemistry Communications, 75 (2017) 60-63.

[167] C. Boyer, S. Gamburzev, A.J. Appleby, Evaluation of methods to increase the oxygen partial pressure in PEM fuel cells, Journal of Applied Electrochemistry, 29 (1999) 1095-1102.

[168] J. Zhang, C. Song, J. Zhang, R. Baker, L. Zhang, Understanding the effects of backpressure on PEM fuel cell reactions and performance, Journal of Electroanalytical Chemistry, 688 (2013) 130-136.

[169] Y.W. Rho, O.A. Velev, S. Srinivasan, Y.T. Kho, Mass Transport Phenomena in Proton Exchange Membrane Fuel Cells Using O_2/He, O_2/Ar, and O_2/N_2 Mixtures: I. Experimental Analysis, Journal of the Electrochemical Society, 141 (1994) 2084-2089.

[170] T.E. Springer, T.A. Zawodzinski, S. Gottesfeld, Polymer Electrolyte Fuel Cell Model, Journal of the Electrochemical Society, 138 (1991) 2334-2342.

[171] S. M, M. Zoppi, P. Nithiarasu, P. Karthikeyan, M. Muthukumar, S. Vignesh Shanmugam, P. Pravin Kumar, S. Murali, A.P. Senthil Kumar, International Conference on Design and Manufacturing (IConDM2013)Optimization of Operating and Design Parameters on Proton Exchange Membrane Fuel Cell by using Taguchi method, Procedia Engineering, 64 (2013) 409-418.

[172] L. Wang, A. Husar, T. Zhou, H. Liu, A parametric study of PEM fuel cell performances, International Journal of Hydrogen Energy, 28 (2003) 1263-1272.

[173] M.A.R.S. Al-Baghdadi, H.A.K.S. Al-Janabi, Effect of operating parameters on the hygro–thermal stresses in proton exchange membranes of fuel cells, International Journal of Hydrogen Energy, 32 (2007) 4510-4522.

[174] B. Zhou, W. Huang, Y. Zong, A. Sobiesiak, Water and pressure effects on a single PEM fuel cell, Journal of Power Sources, 155 (2006) 190-202.

[175] P. Hartmann, D. Grübl, H. Sommer, J. Janek, W.G. Bessler, P. Adelhelm, Pressure Dynamics in Metal–Oxygen (Metal–Air) Batteries: A Case Study on Sodium Superoxide Cells, The Journal of Physical Chemistry C, 118 (2014) 1461-1471.

[176] D. Grübl, J. Janek, W.G. Bessler, Electrochemical Pressure Impedance Spectroscopy (EPIS) as Diagnostic Method for Electrochemical Cells with Gaseous Reactants: A Model-Based Analysis, Journal of the Electrochemical Society, 163 (2016) A599-A610.

[177] A.M. Niroumand, W. Mérida, M. Eikerling, M. Saif, Pressure–voltage oscillations as a diagnostic tool for PEFC cathodes, Electrochemistry Communications, 12 (2010) 122-124.

[178] M.P. Rodgers, B. Li, P. Choi, D. Slattery, L. Bonville, H.R. Kunz, J.M. Fenton, Procedure for Performing PEM Single Cell Testing, in: High Temperature Membrane Working Group Meeting, Florida Solar Energy Center, Arlington, Virginia, 2009.

[179] Fuel cell technologies - Part 7-1: Test methods - Single cell performance tests for polymer electrolyte fuel cells (PEFC), in: I.E. Commission (Ed.) IEC TS 62282-7-1, Geneva, Switzerland, 2017.

[180] A. Albert, A.O. Barnett, M.S. Thomassen, T.J. Schmidt, L. Gubler, Radiation-Grafted Polymer Electrolyte Membranes for Water Electrolysis Cells: Evaluation of Key Membrane Properties, ACS Applied Materials & Interfaces, 7 (2015) 22203-22212.